Gravitational Lensing in Galaxy Cluster Abell 1689

Aleksi Halkola

Gravitational Lensing in Galaxy Cluster Abell 1689

Aleksi Halkola

Ph.D. Thesis
at the faculty of physics
of Ludwig-Maximilians-Universität München

Submitted by
Aleksi Halkola

Munich, 9. November 2006

First Examiner: Prof. Dr. Ralf Bender
Second Examiner: Prof. Dr. Hans Böhringer
Date of oral examination: 16. April 2007

Zusammenfassung

In dieser Doktorarbeit wird der Galaxienhaufen A1689 untersucht. Der Haufen ist relativ nahe (die Rotverschiebung ist 0.18) und es existieren hervorragende Bilddaten im Hubble-Space-Teleskop-Archiv, die eine unübertroffene Vielzahl an Gravitationslinseneffekten aufweisen. Wir benutzen diese so genannten Arcs und ca. 100 Mehrfachbilder von Galaxien, um verschiedene Aspekte seiner Massenverteilung zu untersuchen.

Am Anfang wird eine kurze Einführung in die Kosmologie und Allgemeine Relativitätstheorie sowie eine Motivation für diese Doktorarbeit gegeben. Es folgt eine Beschreibung des Programms, das für die Analyse des starken Linseneffekts entwickelt wurde.

Der Schwerpunkt dieser Arbeit beruht auf der Identifizierung gelinster Mehrfachbilder von Hintergrund-Galaxien. Ihre Positionen dienen dazu, sowohl die globale Massenverteilung des Haufens als auch die Masse, die mit den ihnen innewohnenden Galaxien assoziert ist, einzuschränken. Durch die sogenannte Fundamental Plane wurde die Geschwindigkeitsdispersion dieser Haufengalaxien abgeschätzt. Die glatte Komponente der dunklen Materie (DM) im Galaxienhaufen wird mit zwei alternativen Parametrisierungen beschrieben, einem nicht-singulären isothermen Ellipsoid (NSIE) und einem elliptischen Navarro-Frenk-White-Profil (ENFW). Mit dem Linsenmodell erhalten wir dann sowohl das gesamte Massenprofil als auch die separaten Beiträge von der Galaxienkomponente und der glatt verteilten dunklen Materie. Die beiden konkurrierenden DM-Profile liefern dieselbe Fitqualität und sind daher nicht unterscheidbar. Die Ergebnisse mit Massenprofilen, die aus Röntgendaten und dem schwachen Linseneffekt abgeleitet wurden, liegen um einen Faktor 2 niedriger. Diese Diskrepanz wurde in der Literatur bereits diskutiert, und es besteht ein genereller Konsens, dass systematische Fehler in der Anwendung der beiden anderen Methoden die Ursache sind. Verglichen mit Massenprofilen von A1689, die aus früheren Analysen des starken Linseneffekts stammen, liefert diese Arbeit ähnliche Ergebnisse, wobei unsere Arbeit die Mehrfachbilder und Arcs signifikant besser reproduziert. Die Ursache dafür ist die sorgfältige Berücksichtigung der Galaxienkomponente in unserem Modell. Diese Galaxienkomponente wird im Detail studiert und die Ausdehnung der dunklen Materiehalos bestimmt. Verglichen mit Feldgalaxien sind die Halos der Haufengalaxien jedoch deutlich kleiner. Mit dieser Arbeit ist zum ersten Mal die Größenmessung der Galaxienhalos mit dem starken Galaxienlensing gelungen. Die Ergebnisse stimmen qualitativ mit denen aus dem schwachen Linseneffekt überein. Diese wurden in anderen Galaxienhaufen gewonnnen, können aber größere systematische Fehler aufweisen.

Am Ende dieser Arbeit befaßen wir uns schließlich mit dem nach wie vor schlechten χ^2 des besten Linsenmodells. Es wird gezeigt, dass dies erklärt werden kann, wenn die 'glatte' Komponente selbst aus Subhalos zusammengesetzt ist.

Synopsis

In this thesis we have set out to study the galaxy cluster Abell 1689 using strong gravitational lensing. Due to its relative closeness at redshift 0.18 and available archived deep *Hubble Space Telescope* imaging it presents an ideal opportunity to several diverse studies based on strong gravitational lensing.

We start with a brief introduction to cosmology and general relativity as well as motivation for the thesis. This is followed by a short description of the program developed during the thesis to analyse strong lensing systems. We begin the main body of work by identifying the cluster galaxies and by estimating their velocity dispersions using the fundamental plane. The work on cluster galaxies is proceeded by identifying multiple image systems in A1689. The multiple images provide strong constraints for the global mass distribution of the cluster. After the identification of multiple images we detail the different models constructed to obtain robust estimates for the total mass in the cluster. The smooth dark matter is assumed to follow two parametric halo profiles, a non-singular isothermal ellipsoid (NSIE) and an elliptical Navarro, Frenk and White (ENFW) profile. With the models we are able to derive the total mass profile as well as to separate the mass contributions from cluster galaxies and the smooth halo of the cluster. The models based on both the NSIE and ENFW smooth dark matter profiles provide very similar fit qualities and we are unable to rule one of them out. Compared to weak lensing and X-ray estimates of the cluster mass, strong lensing methods obtain total masses consistently higher by factor of ~2. This discrepancy is well discussed in the literature, and there is general consensus that systematic effects in both weak lensing and X-ray methods lead to underestimates of the mass. In addition to the models used to derive the total mass profile of the cluster we also construct separate models to provide a direct comparison to earlier strong lensing work done on the cluster. We find good agreement between the mass profiles obtained, although the multiple images are reproduced significantly better in our modelling. This can be attributed to the careful inclusion of the cluster galaxies in our modelling. We also study in more detail the galaxy component and derive extensions of the dark matter haloes of the cluster galaxies. Compared to field galaxies the haloes of cluster galaxies are strongly truncated. This is the first time the sizes of haloes have been determined using strong lensing alone. The results are in good agreement with previous work done using weak lensing. Last, we investigate the fairly poor χ^2 obtained in strong lensing models of A1689 and find that the observed χ^2 can be explained by assuming that the smooth dark matter halo of the cluster is itself composed of subhaloes.

Contents

List of Figures

List of Tables

Foreword

The thriving forces behind the development of mankind, and us humans as individuals, have always been curiosity and need for survival. Once the latter has been satisfied the first takes over and our mind wanders in the mysteries of the world around us. Some of the most perplexing puzzles for the mind lie in the unreachable distances of the sky above us; the Sun, the Moon and a phletora of other phenomena from shooting stars to planets, from stars to galaxies. The same curiosity that has made people for thousands of years to turn their gaze on the star lit sky has driven also me to astronomy and to try to understand a little more of the Universe in which we live.
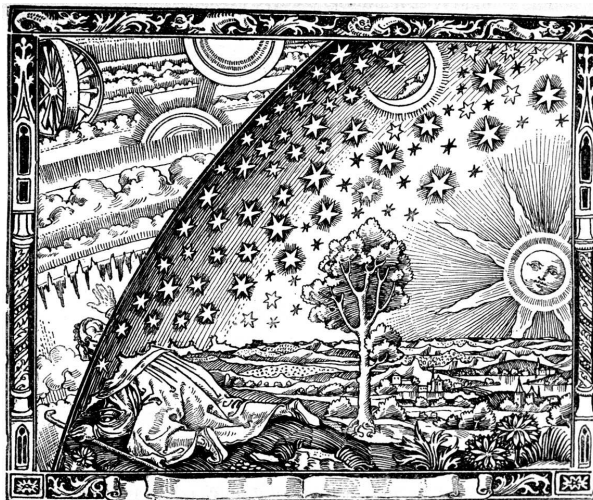
Un missionnaire du moyen âge raconte qu'il avait trouvé le point
où le ciel et la Terre se touchent...

Figure 1: A woodcut by an anonymous artist that was first published in the French astronomer Camille Flammarion's book "L'atmosphère: météorologie populaire". It depicts a scene where a pilgrim from the middle ages finds the place where the sky meets the Earth and is able to see the mechanics of the celestial spheres.

Chapter 1

Introduction

This thesis will deal with the astronomical phenomena on the very largest scales of the Universe: clusters of galaxies, the most massive gravitationally bound systems, on the one hand and galaxies at the edge of the observable Universe on the other. In this introduction we aim to provide the necessary background for the work to follow. We start with the Universe as a whole after the point when the currently understood laws of physics are believed to be valid, its evolution from the cosmic soup to the stars and galaxies we see today. We constrain ourselves mainly to the currently accepted world model, the Standard Cosmology, that starts with a Big Bang, but mention also briefly other alternative ideas. We then proceed to describe in some detail the objects of this thesis, galaxy clusters, and the method used to study them, gravitational lensing.

1.1   The Universe

The visible Universe outside our Solar system is composed of gas clouds, stars, galaxies and groups and clusters of galaxies, the largest known bound systems. The distribution of galaxies in the Universe is not smooth but consists of large voids where only a few galaxies are seen, and filaments with relatively high concentration of galaxies. Clusters of galaxies are seen where these filaments cross.

Through spectroscopy we can study the abundances of different elements. The Universe is mainly composed of hydrogen (~80%) and helium (~20%) with the remaining composed mainly of deuterium and lithium.

In 1965 a uniform microwave radiation was observed by Penzias & Wilson 1965. The temperature of the radiation corresponded to that of a black body at 3.5±1 K and seemed to come equally from all directions on the sky. This led to the interpretation of it being an antenna noise in their measurements. The existence of the cosmic microwave background radiation was predicted some years earlier by G. Gamow in 1948 and by R. Alpher and R. Herman in 1950. Although for Penzias & Wilson (1965)

the radiation was noise in the signal the interpretation of the radiation came in the same volume of the Astrophysical Journal by Dicke et al. (1965) who were devising an experiment to find the very radiation discovered by Penzias & Wilson. It is now widely accepted that the cosmic microwave background is a relic from the hot birth of the Universe. The temperature of the radiation has now cooled to around 3K due to the expansion of the Universe. The background radiation has since been measured with various instruments at different wavelengths, sky coverage and spatial resolution (COBE, Bennett et al. 1996; MAXIMA, Hanany et al. 2000; BOOMERanG, Crill et al. 2003; WMAP, Spergel et al. 2003 amongst others)

1.1.1   Standard Cosmology

Any cosmological model of the Universe should be able to meet the observational constrains, and ideally also have verifiable predictions for further observations. The most developed and mature model is the Standard Cosmology which successfully accounts for the observations but unfortunately has very little predictive power.

In order to start building a cosmological model some simplifying assumptions need to be made. For the Standard Cosmology these are:

- Gravitational force dominates the interactions of large-scale structure and is described by Einstein's theory of gravity

- On sufficiently large scales the distribution of matter in the universe is isotropic and homogeneous.

The two points together ensure that we can find a relatively simple solution to the Einstein field equations. Before Einstein, space and time were considered separate entities but after the publication of his theories of relativity space and time have been thought of as a space-time continuum. The field equations are a set of 10 equations arising from a single tensor equation that describes how time, space and energy are interrelated. In an isotropic and homogeneous universe the solution is called the Robertson-Walker metric,

$$ds^2 = c^2 dt^2 - a(t)^2 \left(\frac{dr^2}{1 - kr^2} + r^2(d\theta^2 + \sin^2(\theta)d\phi^2) \right), \tag{1.1}$$

where s is the proper distance, c is the speed of light, t is time, $a(t)$ is the expansion parameter at time t, and (r, θ, ϕ) are the usual spherical coordinates. In an isotropic and homogeneous universe there is no dependence on the direction and so $d\theta^2 = d\phi^2 = 0$. The parameter k describes the curvature of the universe. $k = 0$ corresponds to a geometrically flat universe, whereas $k < 0$ and $k > 0$ correspond to an open and closed universe respectively. A flat universe marks the boundary between an eternally expanding open universe and one that eventually starts collapsing under the attractive force of gravity.

With the adoption of the Robertson-Walker metric the 10 field equations are reduced to just 2, the Friedmann equations,

$$\frac{\ddot{a}}{a} = -\frac{4\pi G}{3}\left(\rho + 3\frac{P}{c^2}\right) + \frac{1}{3}\Lambda c^2 \text{ and} \tag{1.2}$$

$$H^2 = \left(\frac{\dot{a}}{a}\right)^2 = \frac{8\pi G\rho}{3} + \frac{1}{3}\Lambda c^2 - \frac{kc^2}{a^2}, \tag{1.3}$$

where in addition to the parameters in the metric we have the gravitational constant G, density ρ, pressure P, cosmological constant Λ and the Hubble parameter H. The Hubble parameter H (defined in equation 1.3) is related to the expansion rate of the universe, and was measured for the first time by Hubble (Hubble, 1929). The current value is usually denoted by H_0. The value has been under hot debate until recently and many other measurables depending on H are hence often given for a nominal value of H_0=100 h km/s/Mpc[1], and a dependence on h. The best determination of H_0 to-date comes from the measurements of the cosmic microwave background with the WMAP satellite and is H_0=71$^{+4}_{-3}$ km/s/Mpc (Spergel et al., 2003). The Hubble constant has been measured using several other techniques which yield similar results. Freedman et al. (2001) gives a nice summary on recent developments.

In addition to the Hubble parameter other convenient definitions include the density parameters

$$\Omega_m = \frac{\rho_m}{\rho_c} = \frac{8\pi G}{3H^2}\rho_m, \quad \Omega_r = \frac{\rho_r}{\rho_c} = \frac{8\pi G}{3H^2}\rho_r, \quad \Omega_k = -\frac{kc^2}{a^2 H^2}, \quad \text{and} \quad \Omega_\Lambda = \frac{\Lambda c^2}{3H^2} \tag{1.4}$$

for the scaled matter (Ω_m), radiation (Ω_r), curvature (Ω_k) and cosmological constant (Ω_Λ) energy densities of the universe respectively. ρ_c denotes the critical density for a flat universe with $k = \Lambda = 0$ and is equal to $3H^2/8\pi G$. For relativistic particles, e.g. photons, the density ρ and pressure P are related by the equation of state $P = w\rho$ with $w = 1/3$ and so $\rho_r = 3P$. The cosmological constant Λ has $w = -1$ and so it has negative pressure associated with it that drives the accelerating expansion of the universe as seen in observations of distant supernovae (e.g. Riess et al., 1998). Although $w = -1$ corresponds to a cosmological constant, also alternative theories for this dark energy, as it is also know, exist. In quintessence models, for example, the equation of state can vary in time and can obviously depart from unity.

---

[1]Parsec is an often used distance measure in astronomy. An object is at a distance of one parsec if its position on the sky relative to distant objects changes by ±one second of arc as the Earth rotates from one side of the Sun to the other. The nearest stars are some parsecs away, galaxies have typical radii of a few tens of kiloparsecs (kpc) and the sizes of clusters of galaxies are measured in megaparsecs (Mpc). Light travels one parsec in roughly 3.3 years.

The observations (recently Spergel et al., 2003) show that the geometry of the Universe is very close to flat and so $k = 0$. This means then that also $\Omega_k = 0$ and is hence often ignored. On the other hand the matter density is composed of two parts, the baryonic Ω_b and dark matter[1] Ω_{DM} components so that $\Omega_m = \Omega_b + \Omega_{\text{DM}}$.

We take this opportunity to introduce another important quantity in astronomy. This is the redshift z which can be used both as a time and distance indicator. In an expanding universe photons loose energy, and the wavelength of the photon is increased. This means that when we observe a galaxy at cosmological distances, the spectrum appears to have shifted to longer wavelengths by a factor $1 + z$.

The redshift of an object can be written in terms of the scale factor $a = a(t)$ at the time when the photon was emitted and the scale factor at the present time, $a_0 = a(t_0)$. What is actually observed are the the rest-frame wavelength of the emitted radiation λ_e, and the observed wavelength λ_o. The wavelength and scale factors are related, so that $\lambda_o/\lambda_e = a_0/a(t)$. The redshift z can then be written in terms of the expansion of the universe, and the observable wavelengths, as

$$z = \frac{a_0 - a}{a} = \frac{\lambda_o - \lambda_e}{\lambda_e}. \tag{1.5}$$

Redshifts are very important as distance measures on cosmological scales. For nearby objects the relative motion of the Earth and the object can also lead to a change in the observed wavelength, and hence redshifts cannot do not provide accurate distances within the local Universe.

The five parameters mentioned earlier (H, Ω_{DM}, Ω_b, Ω_r and Ω_Λ) are the parameters of a homogeneous and isotropic universe. In a perfectly homogeneous and isotropic universe no structures such as planets, stars and galaxies, can form and so we must introduce some inhomogeneities. As long as the scale of these inhomogeneities is much smaller than the universe we can still assume the background universe to behave like a Robertson-Walker model. Such a model is referred to as either an almost Robertson-Walker model or just Robertson-Walker model for simplicity.

The initial fluctuations $\delta(t, \boldsymbol{x})$ are small and written in terms of the mean density of the universe $\bar{\rho}$ so that $\delta(t, \boldsymbol{x}) \equiv \frac{\rho - \bar{\rho}}{\bar{\rho}}$. The density fluctuations in the early Universe are very nearly Gaussian (Spergel et al., 2003) and so are fully described by the amplitude A and the index n of the power spectrum of the Fourier transform δ_k of $\delta(t, \boldsymbol{x})$.

The Standard Cosmology has then seven parameters that describe the energy density, geometry and the expansion of the universe on large scales and the small scale variations of the otherwise homogeneous universe. These parameters are not in any way predicted by the model itself and need to come from observations. In Table 1.1.1

---

[1]Some dark matter candidates are mentioned in the appendixA

Table 1.1: Power Law ΛCDM Model Parameters - WMAP only. The Table is slightly modified from Spergel et al. (2003). Ω_{tot} is derived with additional measurements of H_0 from both supernova and HST Key Project (Freedman et al., 2001). Ω_Λ is obtained assuming $\Omega_{\text{tot}}=\Omega_m+\Omega_\Lambda$

Parameter Name	Parameter	Value
Baryon Density	Ω_b	0.046 ± 0.002
Matter Density	Ω_m	0.27 ± 0.06
Hubble Constant	h	0.72 ± 0.05
Amplitude	A	0.90 ± 0.10
Spectral Index	n_s	0.99 ± 0.04
Total Density	Ω_{tot}	1.02 ± 0.02
Cosm. Constant	Ω_Λ	0.75 ± 0.08

we give the measured values for the parameters as obtained from the measurements of the cosmic microwave background radiation by Spergel et al. (2003).

With a standard cosmology in place we will now proceed to the evolution of the Universe and outline briefly the main phases in the evolution our Universe from the beginning in a Big Bang to the present day.

1.1.2 Cosmological eras

The evolution of the Universe can be divided into several distinct epochs according to the temperature or the dominant Ω of the time. In the early phases of the evolution the time is most conveniently measured in seconds after the beginning, and time continues to be used until we enter the edge of the observable Universe. After this point we start using redshift as an indication for time since it can be measured directly.

1.1.2.1 The Beginning

The very beginning of the Universe will remain a tightly guarded secret until our knowledge of the physics at the highest energies improves either through theoretical work, or more importantly, by direct observations and experiments at energies higher than 100 Gev. The laws of physics have currently been tested only to energies below this limit and as is often in science new improved observations require us to revise the way we think about a subject.

There are several theories that hypothesise on the properties of the very early Universe at the Planck time of $\sim 10^{-43}$ seconds. In order for progress to be made the seemingly incompatible theories of quantum mechanics and Einstein's general relativ-

ity need to be combined to one all encompassing theory that could be used to predict the conditions of the Big Bang, the singularity in general relativity that marks the creation of the Universe. At the Planck epoch the now different forces, electromagnetism, weak nuclear force, strong nuclear force and gravity, would be unified to one fundamental force.

At roughly 10^{-33} seconds gravity begins to separate from the other forces. The physics is described by the Grand Unified Theories of the Standard Model where electromagnetism and the strong and weak nuclear forces are unified.

1.1.2.2   Inflation

As the strong nuclear force separates from the electroweak force the energy provided by symmetry breaking starts the following phase, the inflation. During inflation the Universe undergoes exponential expansion. Inflation explains some of the outstanding problems in the Standard Model, for example, the very smooth cosmic microwave background observed today and the flatness of the geometry. The structures seen in the Universe today are believed to originate from the quantum fluctuations in the Universe before inflation and the exponential expansion during the inflation naturally flattens the Universe as is observed today. It should be noted that for the Universe to be flat today requires it to be flat to within 1 part in 10^{15} directly after the Big Bang!

1.1.2.3   Matter

At roughly 10^{-6}s to 10^{-2}s the Universe enters the hadron epoch when quark-gluon plasma making up the Universe cools and produces hadrons. These are baryons and mesons composed of quarks which are held together by the strong nuclear.

1.1.2.4   Nucleosynthesis

One second after the Big Bang the Universe is cool enough for protons and neutrons to form atomic nuclei. The atoms created are mostly hydrogen ($\sim$75% ^{1}H, $\sim$0.01% D) and helium ($\sim$25% ^{4}He, $\sim$0.01% ^{3}He) and smaller amounts of beryllium and lithium. The relative amounts of the elements produced in the nucleosynthesis depends critically on the baryon density of the Universe and require that $\Omega_b \approx 0.04$. The dependences of the different elements on the baryon density can be seen in Figure 1.1 taken from Burles et al. (1999). The helium abundance is sensitive to the number of neutrino flavours, and the element abundances are satisfied with 3 flavours.

The evolution of the Universe has been dominated by radiation density and this continues to be so for the next 70 000 years. This is a relatively quiet period during which the Universe cools further. The matter density evolves like the inverse of the scale of the Universe cubed, a^{-3}, where as the radiation density falls of faster, a^{-4},
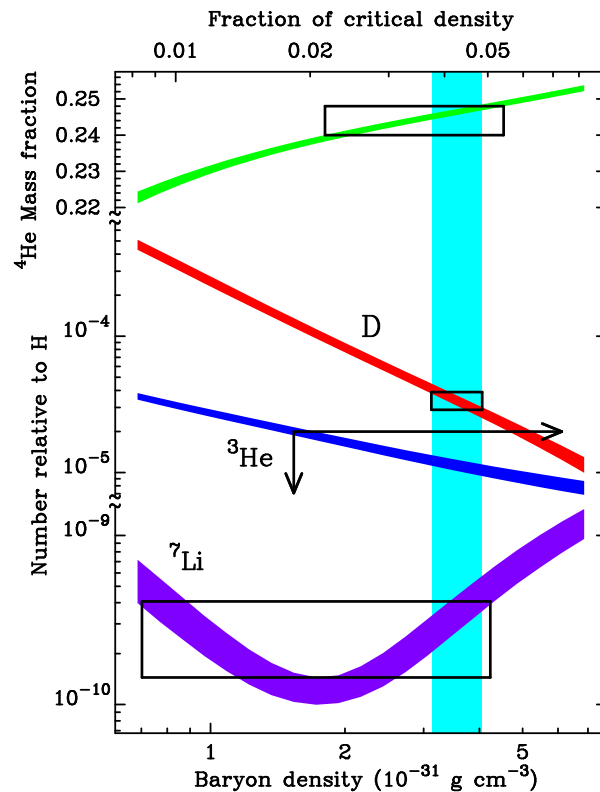
Figure 1.1: A figure showing how the abundances of the light elements produced the Big Bang nucleosynthesis vary with the baryon density. The figure has been taken from Burles et al. (1999)

due to the reduced energy of the photons during expansion. This increases the relative influence of matter on the evolution of the Universe as the temperatures continue to fall. After this period the relative densities in the radiation field and in matter are in rough equilibrium and as the Universe continues to expand the importance of matter for the evolution of the Universe continues to increase. We have entered the matter dominated era. The primordial density perturbations can start to grow.

1.1.2.5 Combination

After another 300 000 years, when the Universe is still at its infancy at an age of mere 380 000 years, the Universe is finally sufficiently cool for hydrogen and helium atoms to form when the nuclei can hold on to the electrons. The matter becomes transparent to the photons, which form a free flowing background radiation. It is this radiation that we see today at microwave energies. Before combination, interactions between matter and

radiation is frequent and direct observations of times before the combination are not possible as all features are erased by the photons. Not much is known observationally between the creation of the CMBR on the surface of last scatter at redshift~1100 and the time when the first stars and galaxies were formed.

1.1.2.6 Reionisation

When the first stars (Population III[1] stars) formed they produced large amounts of radiation that efficiently reionised the atomic gas of the Universe. Apart from taking part in the reionisation of the Universe they also enrich the primordial gas from which the next generation of stars forms. Quasars[2] are also thought to have formed at a similar time and taken part in the reionisation process. High redshift quasars with z~6 show absorption features of neutral hydrogen in their spectra indicating that at least a few percent of the gas was neutral by that time. The WMAP mission measured a reionisation redshift of $z_r = 17 \pm 4$, earlier than expected from the quasar spectra. The three year WMAP results have since lowered the reionisation redshift to $10.9^{+2.7}_{-2.3}$ (Spergel et al., 2006).

1.1.3 Structure formation

The first structures in the Universe were quasars and the hypothetical Population III stars that reionised the Universe. These are formed in local high density regions embedded in large scale over densities. In the cold dark matter paradigm of the Standard Model, the structures in the Universe are formed hierarchically by smaller structures merging, creating larger structures that merge further to create even larger structures. On large scales the evolution is dominated by gravitational forces than can be easily solved using powerful computers and N-body simulations. These largely reproduce the observed structures seen in the Universe today. Problems present themselves at small scales where gas dynamics and the details of star formation become important. What is clear though is that the inhomogeneities seen in the CMBR are too small to grow to the structures observed today. In the current paradigm most of the matter in

---

[1]Population III stars are the first stars that form and are made up entirely of the primordial gas from the Big Bang and hence share its element abundances. They are possibly very massive with masses ranging from 10-100 solar masses and are very short lived. These have never been observed.

Population II stars form from the metal (anything other than hydrogen and helium) enriched gas expelled by the Population III stars during their lifetime.

Population I stars are the most metal rich stars formed from the recycled gas from the previous two populations.

[2]Quasars are very energetic systems that are powered by supermassive black holes that accrete material from an accretion disk surrounding them. The highly directed emission from quasars is emitted perpendicular to the accretion disk. Due to the very concentrated radiation, quasars can be observed in the early Universe at $z > 6$.
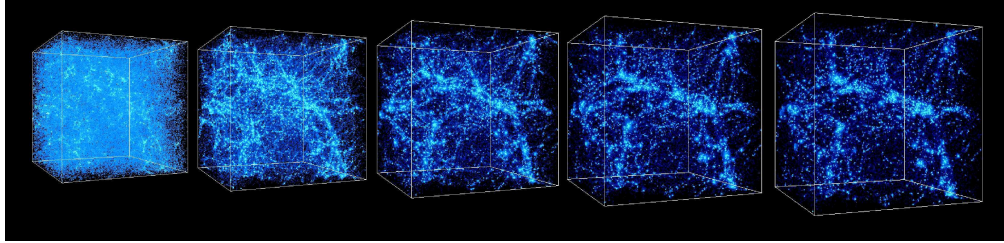
Figure 1.2: The evolution of structure in a ΛCDM universe N-body simulation[1]. The boxes show the (dark) matter density at different redshifts from z=10 (left) to the present day (z=0, right). The small scale structures form first and later merge to create larger objects.

the Universe is of a new type called dark matter. This new type of matter interacts only gravitationally. Since this new type of matter doesn't feel the radiation field, it is able to form structures already before the matter and radiation decouple. The normal baryonic matter then falls into the potential wells of the dark matter after the decoupling from radiation.

In addition to clearing the problem of structure formation, dark matter solves also other 'missing mass' problems. The observed flat rotation curves of galaxies and the high velocity dispersions of clusters of galaxies indicate that the total masses in galaxies and clusters far exceed the mass that can be contained in the luminous components of these structures.

A typical scenario of structure formation is shown in Figure 1.2. It shows how the density evolves from redshift $z = 10$ to the present day ($z = 0$) in numerical simulations. The density is fairly smoothly distributed to begin with but voids and filaments are formed as the denser regions contract and merge.

The Universe is still in this phase, and galaxies and clusters continue to form and evolve. We end this introduction to cosmological eras with some details on the properties of galaxies and clusters of galaxies.

1.1.3.1 Galaxies

After stars, galaxies are the next fundamental building blocks for structures in the Universe. Galaxies typically have 10^7 to 10^{12} stars, and their masses range from 10^7 to 10^{13} M$_\odot$. Their luminous components extend out to several tens of kiloparsecs and their dark haloes out to several hundreds of kiloparsecs.

---

[1]The simulations were performed at the National Center for Supercomputer Applications by Andrey Kravtsov (The University of Chicago) and Anatoly Klypin (New Mexico State University).
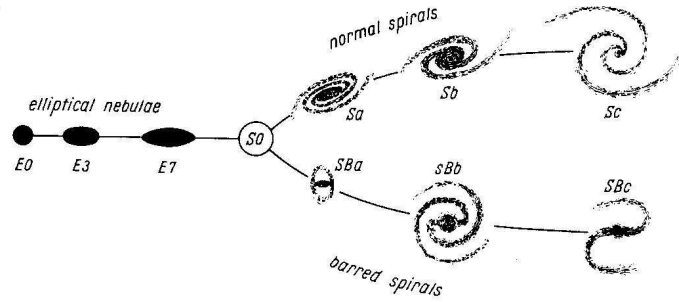
Figure 1.3: The Hubble tuning fork for galaxy classification. Elliptical galaxies (E0-E9) are on the right, spiral galaxies (Sa, Sb, Sc, SBa, SBb, SBc) on the right. Although originally proposed as an evolutionary sequence from left to right the direction has since been reverse.

It is still unclear when the first galaxies were formed but some galaxies have recently been identified with probable redshifts ~7 (Bouwens et al., 2004; Richard et al., 2006; Labbé et al., 2006). These galaxies have most likely formed at redshifts $\gtrsim 8$ when the Universe was only 500-600 million years old and still ionised.

Hubble (1936) constructed the so called Hubble tuning fork diagram. It is a classification scheme for galaxies according to their morphology. Hubble originally thought of it as an evolutionary track from the left to the right, from the elliptical galaxies to the spiral galaxies. The elliptical galaxies are classified based on their visual oblateness from E0 to E9. The classification of spiral galaxies is based on the increasing openness of the spiral arms. The spiral galaxies can be either normal (Sa, Sb, Sc) or barred (SBa, SBb, SBc) and this separation creates the tuning fork shape of the diagram. The direction of evolution has since been reversed, and elliptical galaxies are nowadays believed to form in mergers of spirals galaxies. In addition to the elliptical and spiral galaxies, Hubble also included an S0 galaxy as a transitional galaxy type between the two galaxy types, and an irregular galaxy type for galaxies that don't have clear morphological structure. A revision of the Hubble sequence for elliptical galaxies was proposed in Kormendy & Bender (1996). The original classification of elliptical galaxies is strongly affected by projection effects. The proposed new classification uses isophotal shapes that are in contrast related to fundamental properties of the galaxies such as the distribution of stellar orbits in the galaxy.

The different galaxy types have the following characteristic properties:

- The irregular galaxies are generally composed largely of gas and have a high star formation rate. They don't have recognisable spiral structure and also lack a

prominent nuclear bulge.

- Spiral galaxies have a disk with spiral arms with considerable angular momentum. The bulges of spiral galaxies are made of old and red Population II stars. The spiral arms have relatively high star formation rates and are composed largely of young Population I stars, generally bluish in colour. Due to the evolution scheme by Hubble these are also called late type galaxies.

- Elliptical galaxies have only a small amount of angular momentum compared to spirals and are dominated by random motions of the stars in the galaxy. They are also poor in interstellar gas and have mostly old Population II stars with little current star formation. Elliptical galaxies are often called early type galaxies.

The first galaxies to have formed were irregular and spiral galaxies with active star formation. Through galaxy mergers these have then formed the elliptical galaxies. All galaxy types continue to evolve through external inputs via mergers as well as internally through the evolution of the stellar populations in the galaxies.

1.1.3.2   Galaxy Clusters

Clusters of galaxies are the largest gravitationally bound systems in the Universe. They can be composed of several hundred galaxies and have masses up to $\sim 10^{15}$ $M_\odot$ and extents up to $\sim$2-3 Mpc. The typical velocity dispersions of the galaxies in a cluster are $\sim$1000 km/s. Although some of the mass in clusters is in the galaxies and intracluster gas, most of it is in a dark matter halo surrounding the whole cluster. The intracluster gas is hot, $\sim 10^8$ K, and emits X-ray photons. Cluster masses and radial mass profiles can be estimated from the X-ray emission, the velocity dispersion of the cluster galaxies or using weak or strong lensing.

Clusters have a composition similar to that of the Universe as a whole, and so by measuring both the baryonic mass and the total mass in a cluster it is possible to constrain the baryonic fraction of the Universe.

The mass profiles of clusters are an important test for the nature of dark matter, and its precise determination for a large number of clusters is an on going process. Numerical simulations with cold dark matter predict a so called universal dark matter profile. Navarro et al. (1996) showed that a simple fitting function can be used to describe the profiles of dark matter haloes at opposing ends of the mass scale, all the way from individual galaxies to the largest clusters. The so called Navarro, Frenk and White profile (NFW for short) has the following form

$$\rho(r) = \frac{\rho_0}{r/r_s \, (1 + r/r_s)^2}, \qquad (1.6)$$

where r_s is the scale radius of the cluster at which the density profile changes from $\rho(r) \propto r^{-1}$ to $\rho(r) \propto r^{-3}$. The profile is often parametrised in terms of its virial radius, r_{vir}, and concentration, $c = r_{vir}/r_s$. The virial radius determines the mass scale of the cluster.

The inner slope of cluster profiles is debated with some claiming that the logarithmic slope of -1 obtained in Navarro et al. 1996 can be a result of the mass resolution and force softening in the simulations. The proposed slope is steeper, closer to -1.5 (e.g. Fukushige & Makino, 1997; Moore et al., 1998). The profile with an inner slope of -1.5 is called the Moore profile. What is clear from the simulations is that the profiles are cuspy with the density continuing to increase towards the centre of the cluster.

The NFW profile has been generalised to account for the dispute. The generalised NFW profile has an additional free parameter, β, the inner slope of the profile.

$$\rho(r) = \frac{\rho_0}{(r/r_s)^{\beta}\,(1+r/r_s)^{3-\beta}}. \tag{1.7}$$

The standard NFW profile has $\beta = 1$, whereas a Moore profile has $\beta = 1.5$. Regardless of the inner slope, all generalised profiles have the same behaviour at large radii with $\rho(r) \propto r^{-3}$.

Another profile often used with success in fitting cluster profiles is the isothermal sphere. A galaxy or a cluster with an isothermal profile has a flat rotation curve. This is observed in many galaxies and the simplicity of the profile is very appealing. A profile with a flat rotation curve has an infinite mass as the mass increases linearly with the radius. It also has a singularity at r=0 where the density reaches infinity. For clusters a softened isothermal sphere is often used instead. The profile in this case has a flat core with a finite density in the centre. The density can be written as

$$\rho(r) = \frac{\sigma^2}{2\pi G} \frac{1}{r^2 + r_c^2}, \tag{1.8}$$

where σ is the velocity dispersion of the galaxies in the cluster and r_c is the core radius. Setting $r_c = 0$ recovers the singular profile. At large radii the density falls off like r^{-2}. A flat core in a cluster may indicate that dark matter is self-interacting or that the details of gas dynamics are important for the formation of the core. At large radii the density of an NFW profile falls off quicker than isothermal.

1.2 Gravitational lensing

In the curved space-time of general relativity the null geodesics, the paths followed by light rays, are no longer straight but curved due to the mass/energy content of the universe. The whole universe can have a curvature but also local concentrations of mass distort the space-time. This leads to the bending of light rays near massive objects.

Although speculated already earlier based on Newton's law of gravity – acceleration caused by massive objects is independent of mass and hence could, at least in principle, also apply to light – it wasn't until the general theory of relativity that the correct deflection angle for a point mass was obtained. The path of a light ray passing an object of mass M at a distance ξ will be bent by an angle $\hat{\alpha}(\xi)$,

$$\hat{\alpha}(\xi) = \frac{4\mathrm{G}M}{c^2\xi}. \tag{1.9}$$

This is a factor of 2 higher than expected from Newtonian mechanics. The bending of light was the first prediction of general relativity that was also observed. During the 1919 solar eclipse Arthur Eddington measured positions of stars near the edge of the Sun. By comparing the positions to those measured when the Sun was not present the bending angle could be determined. The analysis of the data taken during the eclipse has since been criticised and the results from Eddington's experiment are not as clear-cut as presented at the time.

1.2.1 Theory behind it all

We show in figure 1.4 the basic geometry of a gravitational lens. The lens could be the Sun, a MACHO (massive astronomical compact halo object) in our galaxy, another galaxy or even a cluster of galaxies. In the figure D_d is the angular diameter distance[1] to the deflector. We observe a source S at a distance D_s from us. The distance between the lens and the source is D_{ds}. Without the lens the source S that is offset from the optical axis by a distance η would be observed at an angular position $\beta = \eta/D_s$. Due to the deflection of the light ray from the source passing as it passes through the lens at an optical axis distance ξ the source is observed at I, with an angular position θ. The change in the position of the source is α, and the actual deflection of the light ray at the lens is $\hat{\alpha}$. The famous lens equation in its vector form (from now on all vector quantities are shown with bold font) summarises what is evident already from the figure, namely that

$$\boldsymbol{\beta}(\boldsymbol{\theta}) = \boldsymbol{\theta} - \boldsymbol{\alpha}(\boldsymbol{\theta}). \tag{1.10}$$

The lens equation is written in terms of the angular positions of the source and the lens since this is what is observed. In order to derive the projected physical positions $\boldsymbol{\eta}$

---

[1]Angular diameter distance (D) is a distance measure in astronomy that relates the physical size (x) of an object to its observed angular size (θ) on the sky by $\theta = x/D$.
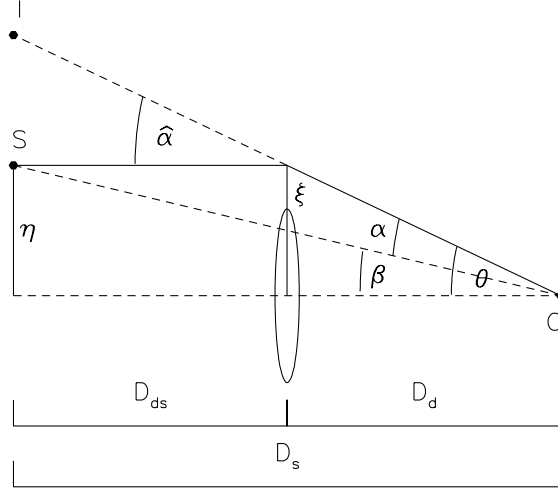
Figure 1.4: A schematic view of the geometry in a simple gravitational lens. An observes at O looking through a lens at a source S at a distance η from the optical axis. The source passes through the lens at a distance ξ from the axis. Angles β and θ correspond to the angular positions of the unlensed source and the lensed source respectively. Angle $\hat{\alpha}$ is the true deflection angle and α is the change in the position of the source called the reduced deflection angle. After the deflection the source appears at position I. The distances D_d, D_s and D_{ds} are the angular diameter distances between the observer and the deflector, observer and source, and deflector and source respectively.

and ξ also the distances D_d, D_s need to be known. Since the distances used are angular diameter distances the angular positions β and θ are related to the projected physical ones η and ξ by definition like,

$$\beta = \eta/D_s, \text{ and } \theta = \xi/D_d. \tag{1.11}$$

In addition the deflection angle $\hat{\alpha}$ is related to the reduced deflection angle α by

$$\alpha(\xi) = \frac{D_{ds}}{D_s} \hat{\alpha}(\xi). \tag{1.12}$$

The deflection angle $\hat{\alpha}$ depends only on the mass distribution and the point where the light ray intersects the lens plane. The change, α, in the angular position β of the source as compared to a universe with out the lens depends also on the relative distances between the observer, the lens and the source. Gravitational lensing is

inefficient for lenses that are close to either the observer or the source. The maximum geometrical efficiency is achieved when the lens lies exactly half way between the source and the observer, i.e. $D_{ds}=D_d$.

Once the image position and the mass distribution of the deflector are known it is in principle very easy to calculate the position of the source. For more general non-symmetric mass distributions, equation 1.9 for the deflection angle of a point mass can be extended for small deflection angles (most astronomical applications) by simple superposition arguments. It can then be be written as

$$\hat{\alpha}(\boldsymbol{\theta}) = \frac{4GM}{c^2 D_d} \int \frac{(\boldsymbol{\theta} - \boldsymbol{\theta}') \, \Sigma(\boldsymbol{\theta}')}{|\boldsymbol{\theta} - \boldsymbol{\theta}'|^2} \, d^2\boldsymbol{\theta}. \tag{1.13}$$

In the above equation all the mass of the deflector is assumed to be at a fixed distance D_d from the observer. The surface mass density $\Sigma(\boldsymbol{\theta})$ can be obtained from the three dimensional mass density $\rho(\boldsymbol{\theta}, z)$ by projecting it on to the lens plane. This is done by integrating over the line of sight from the observer to the source at a distance of D_s,

$$\Sigma(\boldsymbol{\theta}) = \int_0^{D_s} \rho(\boldsymbol{\theta}, D) \, dD. \tag{1.14}$$

Since the extent of the deflector is generally much smaller than the distances D_d, D_s and D_{ds} this so called thin lens approximation is valid for all simple cases. The extent of deflectors (along the line of sight) become important if other mass concentrations of a similar order of magnitude than the lens are on the same line of sight. This can be another galaxy cluster or in the case of cosmic shear the large scale structure of the universe.

Other than the deflection angle and surface mass density, some other important quantities in gravitational lensing are the effective lensing potential ψ, the scaled surface mass density κ and the gravitational shear $\boldsymbol{\gamma}$. The deflection angle can be thought of as a kind of a generalised force, and just like gravitational force and electric force have their respective potentials, a potential can also be attached to the deflection angle. The use of a potential has some powerful mathematical implications making it easy to obtain observable quantities such as κ and $\boldsymbol{\gamma}$ for simple mass distributions. The effective lensing potential ψ can be obtained from the Newtonian potential Φ,

$$\psi(\boldsymbol{\theta}) = \frac{D_{ds}}{D_s \, D_d} \int_0^{D_s} \Phi(D_d \, \boldsymbol{\theta}, D) \, dD. \tag{1.15}$$

This is similar to what was done earlier when the matter density was projected to the lens plane.

α, κ and γ are then related to the derivatives of the potential ψ w.r.t. θ in the following way,

$$\alpha(\theta) = \nabla\psi(\theta), \ \ \kappa(\theta) = \frac{1}{2}\nabla^2\psi(\theta), \ \text{ and} \tag{1.16}$$

$$\gamma_1 = \frac{1}{2}(\psi(\theta)_{11} - \psi(\theta)_{22}) \ , \ \gamma_2 = \psi(\theta)_{12} = \psi(\theta)_{21}, \tag{1.17}$$

where the double indices indicate derivates w.r.t. θ_1 and θ_2. The gravitational lensing shear γ is a complex number and the two components describe the distortion of the image shape locally. κ is defined as the ratio of the local surface mass density Σ and the critical density of the universe Σ_{cr},

$$\kappa = \frac{\Sigma}{\Sigma_{\text{cr}}}, \ \text{ where } \ \Sigma_{\text{cr}} = \frac{c^2}{4\pi G} \frac{D_s}{D_{ds} \, D_d}. \tag{1.18}$$

An important quantity in gravitational lensing that gives also physical insights into the quantities κ and γ is the Jacobian matrix A,

$$A \equiv \frac{\partial\beta}{\partial\theta} = \begin{pmatrix} 1-\kappa-\gamma_1 & -\gamma_2 \\ -\gamma_2 & 1-\kappa+\gamma_1 \end{pmatrix} = (1-\kappa)\begin{pmatrix} 1 & 0 \\ 0 & 1 \end{pmatrix} - \gamma\begin{pmatrix} \cos 2\phi & \sin 2\phi \\ \sin 2\phi & -\cos 2\phi \end{pmatrix}, \tag{1.19}$$

where $\gamma=|\gamma|$ gives the magnitude and ϕ the orientation of the shear. All the quantities are in general functions of θ and depend on the mass distribution. Magnification μ in gravitational lensing is defined as the ratio of the area of the image to that of the source. Since surface brightness is conserved by gravitational lensing this means that the flux is also magnified by the same ratio. Locally the magnification can be defined as $\delta\theta^2/\delta\beta^2$. This is just the inverse of the determinant of the Jacobian matrix A. The magnification μ is then such that $\mu^{-1} = |(1-\kappa)^2 - \gamma^2|$. The magnification in gravitational lensing makes it possible to study galaxies that would otherwise be too faint to be observed.

1.2.2   Strong, weak and micro

After the first observational confirmation of gravitational lensing by Eddington in 1919 it took 60 years until Walsh et al. observed gravitational lensing in the form of two quasars very close to each other, separated by only 5.7". The quasars QSO 0957+561 A and B are both at a redshift of 1.4 and have very similar spectra. The idea that two quasars are images of the same quasar is a natural conclusion especially since between the two images is a foreground galaxy that can act as the lens. Figure 1.5 shows an HST image of the two images (A,B) of the quasar and the lensing galaxy (G1).
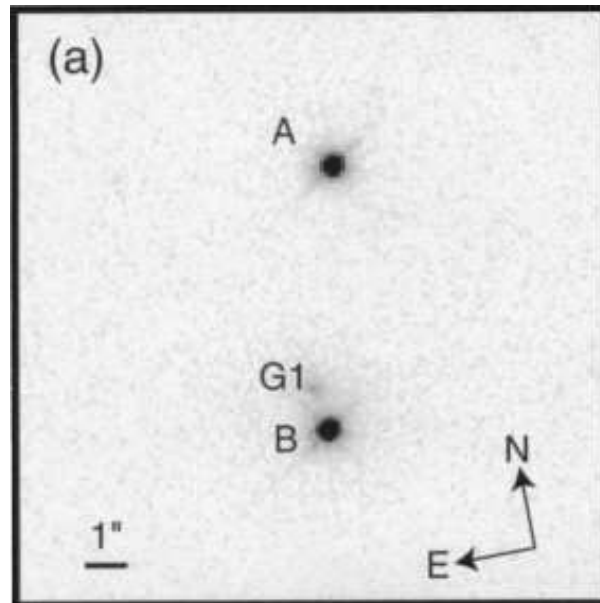
Figure 1.5: The two images A and B of the quasar QSO 0957+561 and the lensing galaxy G1 can be seen in this HST F555W image of the lensing system (Bernstein et al., 1997).

During the time between the observations of Eddington and those of Walsh et al. the field of gravitational lensing had been studied theoretically by many people. Both in the ways of observing the possible phenomena, and applications to cosmology. Many of the ideas from that time have become observational reality by now. Zwicky realised in the late 30's that galaxies could act as viable lenses. He speculated that gravitational lensing by galaxies could be used to not only test General Relativity but also to measure galaxy masses and to study magnified background galaxies. In the early sixties Refsdal considered the possibility of measuring the Hubble constant with gravitational lensing.

Gravitational lensing phenomena are often classified to three distinct regimes: the strong, the weak and the microlensing regimes. The first observed gravitational lensing effect, the bending of light rays by the Sun and the change in the measured positions of stars near the limb of the Sun, has very limited use since the true source positions are almost never known and this effect will not be discussed further here. In the following sections we give only brief qualitative properties and applications of the three regimes.

1.2.2.1   Strong lensing

In the strong lensing regime the lensing effect is strong enough to produce multiple images of the same source. In order to form multiple images, it is necessary for the surface mass density κ of the lens to exceed unity at some point. The separation of the images depends on the mass of the lens and is typically a few arcseconds for a galactic lens and up to several arcminutes in galaxy clusters. The regime where the image separation is of the order of micro seconds (too small to be directly observable) is also technically strong lensing but is often treated separately as microlensing.

In strong lensing mass reconstructions one tries to obtain the mass distribution of the lens by requiring that the mass distribution reproduces the observed properties of the lensed source or sources. The most obvious property to investigate in strong lensing is the image positions. Additional constraints include morphological as well as photometric properties of the images. The distances to the source and the lens are important to know so that overall mass scale can be fixed. The scale is represented by the angular diameter distances D_d, D_s and D_{ds}.

Since the multiple images are assumed to originate from the same source, one property of a lensed source is that all the images of the source are mapped to the same point in the source plane. This works generally well, but due to the mass sheet degeneracy present in lensing, can bias the results towards mass distributions with high magnification.[1]

One can also look for a mass distribution and a source position that produce images at the observed locations on the sky. This is called image plane minimisation and directly compares the model with the observations. The difficulty with image plane minimisation is that in the lens equation (equation 1.10) the deflection angle is a function of the image position θ and not of the source position β. This makes the inversion of the lens equation numerically very intensive and sometimes unfeasible.

Refsdal (Refsdal, 1964) realised that the light rays of multiple images have to travel different path lengths from the source to us. This distance can be measured if a variable source is lensed and the time delays between the variations in the different images can be measured. The size of the Universe depends on the Hubble constant and hence the time delay also. Unfortunately the time delay depends also on the mass distribution of the lens. The mass in the lens needs to be modelled accurately before the Hubble constant can be measured with any certainty. Quasars are well suited for this task since they are very bright and can be seen out to large distances. The lens is also generally a single galaxy, although the effect of the environment surrounding

---

[1]Since the deflection angle depends only on the mass within the images, lensing cannot constrain the mass profile within that area. Lenses that have high magnification map a source to a large area in the image plane. This then also means that images from a large part of the sky are all mapped to the same source position.

Figure 1.6: Highly distorted images of a galaxy (blue objects) behind galaxy cluster Cl0024. The mass in the galaxy bends light rays and acts as a lens, distorting and magnifying images of a distant background galaxy.

the lens is also important. As the observations have improved it has also become evident that the lenses themselves have substructure. The relative magnifications of the different multiple images of a quasar shows variations from smooth galaxy models for the lensing galaxy. The current status of this field is nicely summarised in a conference contribution by P. Schechter (Mellier & Meylan, 2005). The value of H_0 from lensing is H_0=61±7 km/s/Mpc. This is a little lower than the canonical value of $H_0 = 71^{+4}_{-3}$ km/s/Mpc from WMAP data (Spergel et al., 2003).

Strong gravitational lensing can also be seen on larger scales of galaxy clusters. In cluster lensing images of background galaxies are distorted to giant arcs, and possibly many multiple images. These can be used to study the mass distribution of the clusters. One of the first striking examples of this phenomenon observed in nature is shown in figure 1.6. The cluster CL0024+1654 at a redshift of 0.39 lenses a galaxy at a redshift of 1.675 (Broadhurst et al., 2000) into at least 4 easily identifiable images. The cluster has been studied intensively by several groups (e.g. Kassiola et al., 1992; Tyson et al., 1998). Numerical simulations with cold dark matter predict cuspy inner mass profile slopes between -1 and -1.5 (Navarro et al., 1996; Moore et al., 1998). Tyson et al. (1998) exclude an NFW type profile with high confidence finding strong evidence for

a flat inner core. This has later been criticised in Broadhurst et al. (2000); Shapiro & Iliev (2000) who find that an NFW profile in fact does provide a good fit to the data. They claim that the isothermal sphere obtained in Tyson et al. (1998) has much too high a velocity dispersion for the cluster. This highlights the debate that is still active: the slope of the inner mass profiles of clusters obtained by different authors often disagree.

1.2.2.2 Weak lensing

In the weak lensing regime only the shapes of background sources are distorted by the intervening inhomogeneous mass distribution. Both the scaled surface mass density κ and the shear γ are less than unity and no multiple images of the same source are observed. A concentrated mass overdensity, like a galaxy or a cluster of galaxies, induces correlated changes in the ellipticities of the galaxies behind them. Although the effect is small and the background galaxies have intrinsic ellipticity variations the effect can be measured provided sufficient numbers of background galaxies can be observed. Weak lensing can be used to measure the sizes and total masses of the dark matter haloes of galaxies (galaxy-galaxy lensing), the masses and mass profiles of clusters of galaxies and also the large scale structure of the universe (cosmic shear).

The first parameter free inversion technique was presented in Kaiser & Squires (1993). It allows one to reconstruct the surface mass density from the measured ellipticities of sources. The method takes advantage of the connection between κ and γ through the derivatives of the deflection potential ψ. Since 1993 many other reconstruction algorithms have emerged, improving on the limitations of the original method proposed by Kaiser & Squires (1993) (e.g. Kaiser et al., 1995; Broadhurst et al., 1995; Rhodes et al., 2000; Bernstein & Jarvis, 2002, to mention a few).

An exciting recent result by Clowe et al. (2006) provides strong evidence for dark matter in clusters of galaxies. The largely collisionless galaxies and dark matter in the bullet clusters 1E 0657–558 have separated from the intra cluster gas as the two cluster have travelled through each other. With weak lensing it can be seen that most of the mass remains in the smooth dark matter haloes around galaxies. If the larger gravitational force at large distances would be due to modified Newtonian dynamics (MOND) one would expect to see more of the mass concentrated in the intra cluster gas than is observed by Clowe et al. in 1E 0657–558.

A new prospect for weak lensing lies in cosmic shear and weak lensing tomography where the large scale structure of the universe acts as the lens. Cosmic shear and weak lensing tomography can be used to constrain the equation of state of dark energy, and by considering lensed sources in redshift slices also the evolution of w with redshift (time).
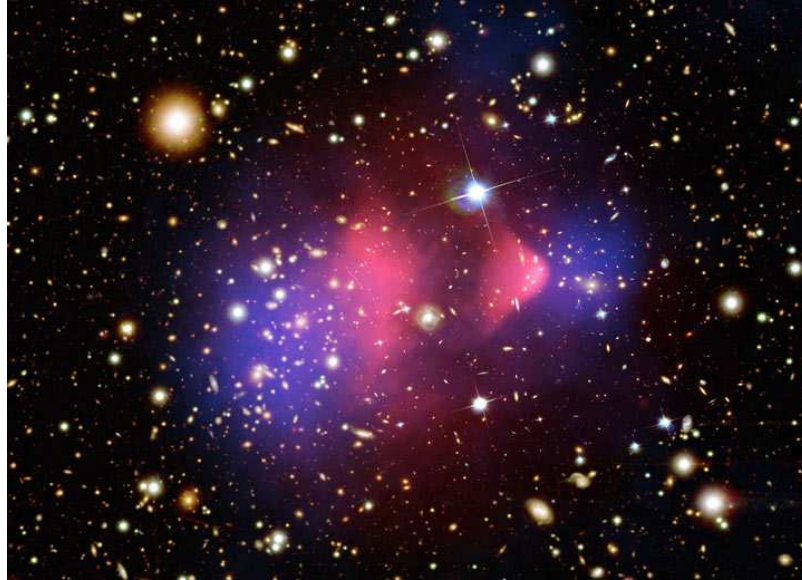
Figure 1.7: The intra cluster gas (red) has been separated from the galaxies and dark matter (blue) in the Bullet clusters 1E 0657–558. The mass estimate is based on a weak lensing analysis of Clowe et al. (2006), the gas is detected from its X-ray emission (Markevitch et al., 2002). The offset between the mass and the gas is difficult to understand in the framework of MOND but is easily explained by dark matter.

1.2.2.3 Microlensing

Microlensing refers to lensing phenomena where the image separation of multiple images is too small to be resolved, of order micro second. If the source and the lens are both on the same line of sight, or very nearly so, the gravitational magnification can still be observed as a brightened source. Since both the lens and the source are generally moving with respect to the observer this magnification changes over time and a light curve can be constructed. This light curve has a characteristic shape and is the same in all wavelengths since gravitational lensing is achromatic. The applications of microlensing are many from finding extrasolar planets to detecting MACHOs in the haloes of galaxies near and far.

1.2.3 Gravitational lensing in clusters of galaxies

One of the most useful and important properties of gravitational lensing is that it is sensitive to any kind of matter that acts gravitationally. This makes it very effective for the study of the mass profiles of galaxy clusters where the hot intra cluster gas emitting X-rays is not necessarily in hydrostatic equilibrium, the velocity dispersion

measurements are affected by complex dynamical structure and most of the mass is in the form of dark matter that cannot be observed directly. With gravitational lensing one measures all the mass from the gas and stars and dark matter. Additionally the dynamical state of the cluster does not affect the results.

In galaxy clusters the dense central regions (typically several hundred kpc) are efficient strong lenses producing multiple images and spectacular giant arcs. The giant arcs constrain the mass within the Einstein radius[1] of the cluster tightly. The cluster centre needs to be well determined for this to yield accurate masses if only one arc is visible. By identifying counter images of the arc on the opposite side of the cluster, mass estimates can be significantly improved.

Clusters where one can identify many multiply imaged sources are more interesting. With multiple images at many different projected cluster centric distances one can effectively measure the mass of the cluster at different radii and accurate radial mass profiles in the central regions can be obtained. If the redshifts of the sources can also be estimated we can effectively break the mass sheet degeneracy mentioned earlier.

Regions outside the Einstein ring and the strong lensing regime distort that shapes of background galaxies and the mass can be estimated using weak lensing mass reconstruction algorithms. This means that the mass profiles of clusters can be extended out and beyond the virial radii of clusters (typically around 2 Mpc).

There is a region between the strong and weak lensing regimes where there are no multiple images but the images are significantly curved (flexion) and the current weak lensing mass reconstruction techniques cannot make full use of the information contained in the shapes of the images of background galaxies. The work to include also this region in the mass reconstruction is starting with papers treating flexion appearing in astro-ph (Goldberg & Natarajan, 2002; Okura et al., 2006; Goldberg & Leonard, 2006; Melchior et al., 2006). This could hopefully reduce the discrepancies sometimes seen between the cluster profile parameters derived from strong and weak lensing, e.g. in Abell 1689.

The masses and mass profiles of clusters are of great astronomical interest for several reasons. Since most of the matter, not only in clusters but also in galaxies and the universe as a whole, is expected to be in some form of cold dark matter the exact distribution of the mass in clusters can give us clues how dark matter interacts with normal baryonic matter and itself. Large cores in clusters could, for example, indicate that dark matter is self-interacting: the interactions between dark matter particles would lead to dissipation of energy and create flat cores for clusters. Accurate masses for large numbers of clusters and groups in the universe are needed to constrain also cosmological models. The initial conditions for structure formation are well know from

---

[1]A spherically symmetric lens produces a ring like image of a background source, if the source is located directly behind the lens. The ring is called an Einstein ring and its radius the Einstein radius.

the imprint left on the cosmic microwave background radiation and the evolution of the inhomogeneities to the present day can be calculated using numerical simulations. What is needed, is an equally good reference point at later evolutionary stages of the universe.

The first strong lensing clusters were discovered when giant luminous arcs were identified in CL2244-02 (Lynds & Petrosian, 1986) and A370 (Soucail et al., 1987). The nature of the arcs was not immediately recognised but spectroscopy of the arcs revealed them to be at high redshifts making gravitational lensing the only viable explanation for the highly elongated structures. Since then many more clusters with giant arcs and multiple images have been found.

Great effort has gone into the detailed studies of many clusters with weak and strong lensing methods as well as X-ray and dynamical mass estimates. Ideally one should obtain the same mass for a cluster regardless of the method but due to different approximations and assumptions in the methods the measured masses can have discrepancies as large as factor of 3 e.g. clusters A2218 (Kneib et al. 1995; Abdelsalam et al. 1998 although recent studies by Girardi et al. 1997; Cannon et al. 1999 claim to resolve this problem.) and A1689 (Girardi et al. 1997; Clowe & Schneider 2001; King et al. 2002; Xue & Wu 2002; Andersson & Madejski 2004). In some other clusters however a good agreement is found. An example of such a cluster is CL2244 (Ota et al., 1998).

The discrepancies are most likely associated with complicated dynamical states of the clusters. Mergers and subcomponents in the mass structure of a cluster can increase the measured line of sight velocity dispersions. The X-rays mass estimates are affected by non-spherical mass distributions in clusters and deviations from hydrostatic equilibrium. Lensing on the other hand is affected by mass structures along the line of sight not associated with the cluster and unknown redshifts of the background sources. The key to our understanding of galaxy clusters is to use all the methods at our disposal.

Another hotly debated issue is related to the exact profile of galaxy clusters. Weak lensing is most sensitive around the scale radius where both NFW and isothermal spheres have logarithmic gradients close to -2. This makes it very difficult to reject one of the profiles with high confidence using weak lensing alone. The inner slope can be obtained with strong lensing but also here controversy prevails with NFW matching the observations well in some clusters (e.g. CL0024, Kneib et al., 2003) and isothermal sphere in others (e.g. MS2137, Gavazzi et al., 2003).

1.2.3.1 Abell 1689

Abell 1689 is a very massive cluster at a redshift 0.18 that has been studied extensively with spectroscopy, X-rays and gravitational lensing. Most of the lensing work done so far is in the weak lensing regime, although some models based on the prominent giant arc have been constructed.

The first dynamical mass estimates measured a very high velocity dispersion of almost 2400 km/s Teague et al. (1990). This has since been reduced by a reanalysis of the data to a more moderate value of 1500 km/s (Girardi et al., 1997). The reanalysis revealed A1689 to have 3 significant substructures with well defined velocities that overlap spatially. Considering them all as one structure gives the very high dispersion of Teague et al. (1990). The 3 separate structure are a likely reason for the problems associated with the very different mass estimates from the 3 methods. The separate structures can increase the observed velocity dispersion of the cluster as well as complicates the mass estimates based on the X-ray emitting gas.

Of the mass estimates, X-ray (Allen, 1998; Xue & Wu, 2002; Andersson & Madejski, 2004) produces consistently the lowest mass estimates. Most recently Andersson & Madejski (2004) obtain a velocity dispersion of only 918 km/s.

Weak lensing has been used in many various forms to estimate the mass of the cluster (Tyson & Fischer, 1995; Taylor et al., 1998; Dye et al., 2001; Clowe & Schneider, 2001; King et al., 2002,?; Clowe, 2003; Broadhurst et al., 2005b). The weak lensing results generally favour a fairly small velocity dispersion of 1000-1200 km/s for an isothermal sphere, although there are also exceptions of the rule (Taylor et al., 1998; Dye et al., 2001).

For a long time the only strong lensing analysis of A1689 was that of Miralda-Escude & Babul (1995) who used two prominent arcs to construct a simple two halo model for the cluster. One of the haloes has a velocity dispersion of 1450 km/s and the other 700 km/s. This is in fairly good agreement with the dynamical mass estimate presented in Girardi et al. (1997).

What has been lacking until very recently is a thorough investigation using the full potential of a strong lensing analysis in this cluster. This deficit will be dealt with in this thesis.

That no proper strong lensing model exists is mainly due to the lack of deep images of the cluster taken with the Hubble Space Telescope. The use of space based observations is necessary in order to be able to resolve the many faint multiple images expected to be identifiable in the cluster. In this work we will use recent HST WFPC2 and ACS images in 6 passbands (WFPC2: F555W, F814W, ACS: F475W, F625W, F775W, F850L) in the HST Science Archive. Essentially the same data set has been used in several other recent strong lensing models of the cluster (Broadhurst et al., 2005a; Diego et al., 2005b; Zekser et al., 2006)

1.3 Outline of the thesis

After this short introduction to the important background and terminology to the subject presented here, the thesis will continue as follows.

In Chapter 2 we quickly describe the code developed as a part of this thesis to allow a flexible and efficient platform under which all the lensing analysis in this thesis could be performed. The GLens package includes the strong lensing mass reconstruction code and separate Yorick[1] routines used for further analysis and visualisation of the obtained cluster models.

The following 2 chapters are made from published journal articles. In Chapter 3 we reproduce an article to be published in the Monthly Notices of the Royal Astronomical Society. In the article we present two parametric strong lensing models for the cluster along with mass profile of the cluster. In Chapter 4 we take advantage of the unprecedented number of multiple images in this cluster and the strong constraints imposed in the mass distribution to derive statistically sizes for the dark matter haloes of the cluster galaxies. This is the first time this has been done using strong galaxy-galaxy lensing in clusters.

In chapter 5 we attempt to explain the poor performance of strong lensing models generally obtained in galaxy clusters. This is done by assuming that the dark matter halo of the cluster as whole is not completely smooth as is assumed in the models but that the halo is composed of numerous smaller mini haloes.

We finally bring it all together and summarise the work in chapter 6.

---

[1]Yorick is an interpreted programming language, designed for post processing or steering large scientific simulation codes. It is freely available at http://www.maumae.net/yorick/doc/index.php

Chapter 2

GLens - a software package for strong lensing analysis

This chapter is intended to give a short introduction to the GLens package. For basic ideas in gravitational lensing see section 1.2 in the Introduction of this thesis and e.g. Schneider et al. (1992); Meylan et al. (2006) for through treatments of the topic.

Gravitational lensing is a powerful tool in studying different astronomical phenomena such as large scale structure in the universe, matter in clusters and galaxies, and extrasolar planets. GLens was written in order to study the dark matter profiles of galaxy clusters but can equally well be used to study individual galaxies also. It is a collection of tools written mainly in c++. It includes an extensive set of plotting routines that utilise Yorick, a diverse interpreted environment well suited for displaying scientific data.

GLens allows the user to model both simple single lens systems like lensing of quasars to strong lensing features identified in massive galaxy clusters where one can identify dozens of lensed sources and the features are created by hundreds of individual lenses. The package implements three parametric density profiles that are physically well motivated in scales ranging from galaxies to galaxy clusters. The parametric models are the universal dark matter profile (NFW Navarro et al. (1996)), and a family of isothermal sphere profiles including truncated isothermal sphere (Brainerd et al., 1996).

GLens inverts the lens equation and does a proper optimisation of the lens parameters in the image plane, that is minimising the distances between observed images and those predicted by the model. Optionally the user can choose minimise in the source plane. This is significantly faster than an image plane minimisation but can in some cases lead to biased model parameters. In calculating the source plane χ^2, the errors estimated for the image positions are scaled with the local magnification. The resulting χ^2 is in most cases a good tracer of the image plane χ^2.

2.1   Parametric Lensing Profiles

Parametric models of gravitational lenses are ideal in many situations due to their well described, and understood, properties and the usually fairly small number of constraints available. Even in over constrained systems with hundreds of multiple images parametric models can perform extremely well, due in part to the limited parameter space needed to explore in order to find good models which limits the danger of finding local minima present in the problem. The parametric profiles implemented in GLens are all well motivated in an astrophysical context through either theoretical arguments or numerical simulations. Although only a few profiles are implemented at the moment the inclusion of additional lensing profiles is very easy, and in principal only the deflection angle needs to be described analytically. The implemented profiles are described in some detail in this section.

2.1.1   Isothermal Sphere / Ellipsoid

A model often used in gravitational lensing for galaxies and clusters of galaxies is a singular isothermal sphere (SIS) (e.g. Gott & Gunn, 1974; Turner et al., 1984). SIS naturally reproduces the observed flat rotation curves of galaxies (e.g. Roberts & Rots, 1973). The following equations describe a non-singular (or softened) isothermal ellipsoid (Hinshaw & Krauss, 1987) where the singularity has been removed with a core radius, and additionally an ellipticity has been incorporated to better model the observed galaxy shapes (Seitz et al., 1998). The velocity dispersion is in principle a direct observable and can be obtained by measuring the velocities of individual cluster galaxies. It defines the overall mass scale of the system. The core radius is included to fit observational data that indicate that some clusters have constant density cores as opposed to an increasing density towards the centre.

In the equations below ellipticity is introduced to the gravitational potential, in a similar fashion to Kochanek et al. (1989), and not the mass distribution. This approach has some problems with large ellipticities, when the accompanying mass distribution can have negative values, as noted by Blandford & Kochanek (1987), Kormann et al. (1994) and others, but is numerically rather simple and straightforward to implement since all parameters of interest can be calculated from the analytic derivatives of the potential. An alternative approach is to have an elliptical mass distribution as demonstrated by Kormann et al. (1994) but the expressions for deflection angle (α), surface mass density (κ) and shear (γ) are considerably more complicated.

In the following equations ψ is gravitational potential, θ is (image) position on the lens plane, ζ is a core radius, $q=b/a=(1-\epsilon)/(1+\epsilon)$ is the axis ratio of the potential and θ_E is the Einstein radius of a singular isothermal sphere.

The equations for the deflection potential ($\psi(\boldsymbol{\theta})$), the deflection angle ($\boldsymbol{\alpha}$), κ and $\boldsymbol{\gamma}$ are

$$\psi(\boldsymbol{\theta}) = \frac{\psi_0}{\zeta} \sqrt{\zeta^2 + q\,\theta_1^2 + \frac{1}{q}\,\theta_2^2} = \theta_E\,C(\boldsymbol{\theta}) \,, \qquad (2.1)$$

with $\theta_E = \frac{\psi_0}{\zeta} = 4\pi \frac{D_{ds}}{D_s}(\frac{\sigma}{c})^2$ and $C(\boldsymbol{\theta}) = \sqrt{\zeta^2 + q\,\theta_1^2 + \frac{1}{q}\,\theta_2^2}$,

$$\boldsymbol{\alpha}(\boldsymbol{\theta}) = \nabla\psi(\boldsymbol{\theta}) = \frac{\theta_E}{C(\boldsymbol{\theta})} \cdot \left(q\,\theta_1,\; \frac{1}{q}\,\theta_2 \right) , \qquad (2.2)$$

$$\kappa(\boldsymbol{\theta}) = \frac{1}{2}\nabla^2\psi(\boldsymbol{\theta}) = \frac{1}{2}\,\frac{\theta_E}{C(\boldsymbol{\theta})^3} \left(Q_+\,\zeta^2 + \theta_1^2 + \theta_2^2 \right) , \qquad (2.3)$$

with $Q_\pm = q \pm \frac{1}{q}$,

$$\gamma_1(\boldsymbol{\theta}) = \frac{1}{2}\,\frac{\theta_E}{C(\boldsymbol{\theta})^3} \left(Q_-\,\zeta^2 - \theta_1^2 + \theta_2^2 \right) , \qquad (2.4)$$

$$\gamma_2(\boldsymbol{\theta}) = -\frac{\theta_E\,\theta_1\,\theta_2}{C(\boldsymbol{\theta})^3} \,, \qquad (2.5)$$

2.1.2   Universal Dark Matter Profile

The universal dark matter profile is an analytic fit to results of numerical N-body simulations of galactic haloes by Navarro et al. (1996). These simulations showed that density profiles of galactic haloes of very different sizes (two decades in radius) could be fitted with a single 'universal' profile. At small radii (r<r_s or x=r/r_s <1) the NFW-profile is flatter than (singular) isothermal with, $\rho \propto r^{-1}$, whereas for large radii (x>1), where $\rho \propto r^{-3}$, it is steeper than isothermal which has $\rho \propto r^{-2}$ everywhere. Numerical simulations at higher resolution than the original Navarro et al. (1996) paper (e.g. Navarro et al., 2004; Tasitsiomi et al., 2004; Diemand et al., 2004) show that the cusp in the centre of a dark matter halo remains and is not a numerical artifact. The origin of the break in the logarithmic slope of density has been attributed to mass accretion processes (Fukushige & Makino, 2001; Salvador-Solé et al., 2005; Lu et al., 2006, end references therein).

Lensing by NFW-profile has been studied in a number of papers (e.g. Bartelmann, 1996; Kneib et al., 1996; Wright & Brainerd, 2000; Golse & Kneib, 2002). We have implemented an elliptical NFW-profile (ENFW) following the formalism described in Meneghetti et al. (2003). They have introduced the ellipticity to the deflection angle rather than the potential (or mass distribution). Here we show only the expression for

the deflection angle. For details of the derivation see Meneghetti et al. (2003).

The deflection angle for a spherical NFW mass distribution at x=r/r_s is

$$\alpha^{NFW}(x) = \frac{4\kappa_s}{x} g(x), \tag{2.6}$$

with

$$g(x) = \ln \frac{x}{2} + \begin{cases} \frac{2}{\sqrt{1-x^2}} \text{arctanh} \sqrt{\frac{1-x}{1+x}} & , x < 1 \\ 1 & , x = 1 \\ \frac{2}{\sqrt{x^2-1}} \text{arctan} \sqrt{\frac{x-1}{x+1}} & , x > 1 \end{cases} \tag{2.7}$$

We approximate an elliptical mass distribution with axis ratio q by elliptical contours of the deflection angle,

$$x \to \chi = \sqrt{q x_1^2 + \frac{1}{q} x_2^2},$$

$$\alpha_1^{ENFW} = \alpha^{NFW}(\chi) \frac{q\, x_1}{\chi}, \quad \alpha_2^{ENFW} = \alpha^{NFW}(\chi) \frac{x_2}{q\, \chi}$$

The surface mass density (κ) and shear (γ) are calculated from the elliptical deflection angles by numerical differentiation;

$$\kappa(\boldsymbol{x}) = \nabla \alpha(\boldsymbol{x}), \tag{2.8}$$

$$\gamma_1 = \frac{1}{2} \Big(\alpha_{1,1}(\boldsymbol{x}) - \alpha_{2,2}(\boldsymbol{x}) \Big), \quad \gamma_2 = \alpha_{1,2}(\boldsymbol{x}) = \alpha_{2,1}(\boldsymbol{x}), \tag{2.9}$$

where $\alpha_{i,j}(\boldsymbol{x}) = \left(\frac{\partial \alpha(\boldsymbol{x})}{\partial \boldsymbol{x}_i} \right)_j$

2.1.3   Truncated isothermal sphere

The truncated isothermal sphere has been introduced by Brainerd et al. (1996) in the framework of galaxy-galaxy lensing. The two parameters of BBS profile are truncation radius (s) and central velocity dispersion (σ). The density profile of the BBS model is then given by

$$\rho(r) = \frac{\sigma^2}{2\pi G r^2} \frac{s^2}{(r^2 + s^2)} \tag{2.10}$$

For $r < s$ the density profile is similar to a singular isothermal sphere ($\rho(r) \propto 1/r^2$) where as for $r > s$ the density falls off quicker ($\rho(r) \propto 1/r^4$) to avoid the infinite mass of an isothermal sphere. The BBS profile parameterisation can also be used to study the dependence of the truncation radius of a galaxy on the environment. Galaxies in high density environments are expected to have less extended haloes due to tidal truncation. The velocity profiles of galaxies as measured from different optical tracers are relatively little affected and remain nearly isothermal but the dark haloes that extend beyond the visible parts of galaxies are strongly truncated.

The deflection angle of a BBS profile is

$$\alpha^{BBS}(x) = \frac{4\pi\sigma^2 D_{ds}}{D_s c^2 x} \left[1 + x - \sqrt{1 - x^2} \right] \tag{2.11}$$

with $x = r/s$.

We have included the ellipticity in the BBS profile in the same way Meneghetti et al. (2003) did for the NFW profile. The deflection angle of a BBS profile with axis ratio q is

$$x \to \chi = \sqrt{qx_1^2 + \frac{1}{q}x_2^2}$$

$$\alpha_1^{EBBS} = \alpha^{BBS}(\chi)\frac{q\,x_1}{\chi}, \quad \alpha_2^{EBBS} = \alpha^{BBS}(\chi)\frac{x_2}{q\,\chi}$$

The surface mass density and shear are calculated from elliptical deflection angles by numerical differentiation as for the NFW profile.

2.2   Finding Optimal Model Parameters

Goodness of fit in strong gravitational lensing can be quantified in two ways. The proper way is to calculate a χ^2 in the image plane, i.e. how far an image predicted by a model is from the observed one. In calculating the positions of predicted images of an image system, we assume that the images of a system originate from the average source of the images. The expression for an image plane χ^2 is then

$$\chi^2 = \sum_k \sum_i \frac{|\boldsymbol{\theta}_{k,i} - \boldsymbol{\theta}_i(<\boldsymbol{\beta}_{k,i}>)|^2}{\sigma_k^2}, \tag{2.12}$$

where $\boldsymbol{\theta}_{k,i}$ is the position of image i in image system k and $\boldsymbol{\theta}_i(<\boldsymbol{\beta}_{k,i}>)$ is the predicted image position corresponding to image at $\boldsymbol{\theta}_{k,i}$ from mean source of system k at $<\boldsymbol{\beta}_{k,i}>$ and σ_k is the error in image positions for system k (estimated to be 1 pixel for all images).

Calculating image plane χ^2 is unfortunately very time consuming since the lens equation needs to be inverted numerically. An additional complication is that for some values of the model parameters not all observed images necessarily exist. This means that an image plane χ^2 does not necessarily converge to the optimal parameters but is trapped in a local minimum.

Goodness of fit can also be estimated by requiring that all images of an image system originate from the same source and hence minimise the dispersion of the source positions. The problem in this case is that the errors are measured in the image plane and do not necessarily represent the errors in source positions. We take account of this by rescaling errors in the image plane with local magnification. Rescaling by magnification largely avoids bias towards cluster parameters with high magnification (large core radius for the NSIE model or small concentration for ENFW model). The source plane χ^2, $\widetilde{\chi}^2$, can be written in the following way,

$$\widetilde{\chi}^2 = 2 \sum_k \sum_i \sum_{j>i} \frac{|\boldsymbol{\beta}_{k,i} - \boldsymbol{\beta}_{k,j}|^2}{\sigma_{k,i}^2/\mu_{k,i} + \sigma_{k,j}^2/\mu_{k,j}}, \tag{2.13}$$

where $\boldsymbol{\beta}_{k,i}$ is the source position of image i in system k, $\sigma_{k,i}$ is the error in the corresponding image position and $\mu_{k,i}$ is the local image magnification.

The advantage of $\widetilde{\chi}^2$ over χ^2 is that for every image position it is always possible to calculate a corresponding source position and so $\widetilde{\chi}^2$ can be calculated for all values of the model parameters making $\widetilde{\chi}^2$ converge well.

To find optimal model parameters it is often a good idea to first minimise $\widetilde{\chi}^2$ to obtain model parameters close to the optimal ones to ensure that the identified multiple images can be reproduced by the models. The optimal model parameters can now found by minimising χ^2 properly in the image plane.

The optimisation of all the free parameters of the lenses and multiple images is based on Powell's directional method in multi-dimensions (Numerical Recipes, Press et al., 1992). For the source plane minimisation the method is fast, the direction of the fastest improvement in $\widetilde{\chi}^2$ is calculated and the free parameters are changes accordingly until convergence is reached or the desired number of minimisation steps has been performed. For the image plane minimisation the implementation contains nested minimisations. For each set of free parameters we need to calculate image positions for a given source. This is done by assuming a starting position for the image at the observed position after which Powell's directional method is used to minimise the

distance between the source of the observed image and the source position we want to predict images for. Since this needs to be done for all images every time a parameter of the model has been changed the minimisation time in the image plane is significantly higher than in the source plane.

2.2.1 Degeneracies

Any multiple image system can only constrain the mass contained within the images. This leads to degeneracies in the derived surface mass profile. The so called mass sheet degeneracy states that if a given surface mass density satisfies image constraints then a new surface mass density can be found, by suitably rescaling this surface mass density and by adding a constant mass sheet. This new surface mass density satisfies image positions as well as relative magnifications equally well, i.e. the mapping $\kappa \rightarrow (1-\lambda)\kappa + \lambda$ leaves all observable image properties intact.

For haloes with variable mass profile this can also create a degeneracy between the parameters of the profile. For the NSIE model a high core radius can be compensated for by a larger velocity dispersion and for NFW a higher scale radius demands a lower concentration parameter.

These degeneracies can be broken if multiple image systems at different redshifts and at different radii can be found. Position of a radial critical line, and so radial arcs, depends critically on the mass distribution in the central regions and hence the core radius. On the other hand tangential arcs give strong constraints on the mass on larger scales. When choosing the parameterisation of the lens one should carefully consider the constraints and choose the number of individual lenses and the free parameters of the lenses accordingly.

2.2.2 Using GLens

The configuration of the lens and observed multiple images is easy and intuitive. Since the diameter distances of the lenses and sources depend on the cosmology, the configuration file starts with the definitions of the energy densities Ω_{m}, Ω_{Λ} and the Hubble constant H_0. The image and lens positions are given in pixels and for the conversion to physical units a pixel scale is also required. For the calculation of the deflection angle, surface mass density and the shear, also the region of the sky in which these quantities are wanted needs to be defined. The format of the header is the following:

```
omega_matter    value
omega_lambda    value
h0              value
pixelscale      value
sky             x_min x_max y_min y_max step
```

The number of lenses can (in principle) be arbitrarily large to accommodate any possible substructure in the lens. For each lens, key profile parameters and a position, ellipticity and position angle can be defined. Any of the above mentioned parameters can also be allowed to have a range of values and the program will then find an optimal value for that parameter in the range provided. In the following we show the configuration of an NSIE lens.

```
lens
nsie
x y             0/1 (x_min x_max y_min y_max)
redshift
sigma           0/1  (min max)
core_radius     0/1  (min max)
ellipticy       0/1  (min max)
position_angle 0/1  (min max)
```

The configuration of a lens starts by defining its type. The type can be either nsie, enfw or bbs. Next follows the position of the lens in pixels and a 0 or a 1 indicating if the position is to be optimised. In case the position is to be optimised, then also the range in x and y need to be given. The last positional coordinate is the redshift. The meanings of the next two parameters depends on the lens profile. The first parameter gives the 'strength' of the lens and the second the 'shape'. For the NSIE profile these are the velocity dispersion and core radius. For the ENFW profile these are r_200 and concentrations. For the BBS profile the velocity dispersion and the truncation radius. The last two parameters are the ellipticity and the position angle of the ellipse. All parameters apart from the redshift can be marked as free parameters.

```
source redshift 0/1 min max
weight
image x y
image x y
image x y
```

The multiple images used are grouped by their sources. The strength of the lens depends on the distance of the source and so a redshift needs to be estimated for all the sources. Any of the redshifts can optionally be added to the list of free parameters of the model. This can be done in cases where the redshifts of the sources are unknown, or account for the errors in photometric redshifts. The multiple images of a given source are assumed to originate from a singe point in the minimisation. Therefore one should try to select clearly identifiable features in the multiple images. For the source one needs to define its redshift (and possible an allowed range), a weight and

the image positions. The weight can be used to give different relative importance to the different multiple images. The weight as well as the positions of multiple images are fixed.

The number of free parameters to be optimised is not limited, but the user should make sure that the number of free parameters is reasonable when compared to the constraints from the observed multiple images. Otherwise strong degeneracies between the model parameters can occur. More multiple images and lenses can be included by simply adding an lens or a source entry in the configuration file.

Once this has been done it is time to call GLens and let it do the work. GLens has many command line options but the most important are -s (–save) and -m (–minimise). -s takes no argument but -m needs to know whether the minimisations should be done in the source plane (1) or in the image plane (2). The optimised lens configuration will be saved in the same file (overwriting the old configuration) unless a different name for the output is given with the -o (–output) flag. If -s flag is used then the deflection angle, surface mass density and the shear data will be written to $< inputfile >$.fits (or to $< outputfile >$.fits if $< outputfile >$ is defined with -o flag).

```
halkola@cursa:~/glens>glens -s -m 2 <inputfile>
```

The fits data cube (where α, κ and γ are stored) is necessary for the plotting of critical curves and caustics as well as surface mass density contours. The critical curves are areas of very high magnification in the image plane. For a circular source this is also where the einstein ring would be seen. The caustics are the corresponding high magnification areas in the source plane. The data saved in the fits cube can also used to predict images and unlensing the observed multiple images in order to reconstruct the true source shape.

2.2.3 Yorick routines

The routines for plotting different aspects of the gravitational lens defined in the configuration file take advantage of the powerful array operations in Yorick. In the following we demonstrate some of the things that can be done with the plotting routines defined in the Yorick script-file glens.i.

```
> open_glens, <inputfile>
> source_z, 3.04
> objects,1,1
> kappa, levs=[ 0.2, 0.4, 0.6, 0.8, 1.0, 1.2, 1.4, 1.6 ]
> crit, color="blue"
> caus
> src_cont,id=1,levs=20,lcolor="magenta",scolor="cyan"
```
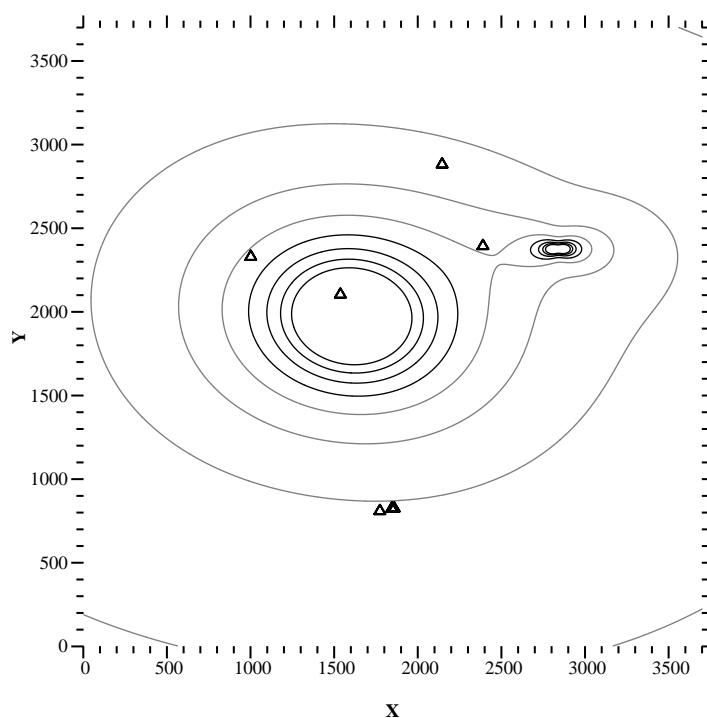
Figure 2.1: The surface mass density contours of a simple two lens system. $\kappa =$ [0.2, 0.4, 0.6, 0.8, 1.0, 1.2, 1.4, 1.6] contours are shown in grey ($\kappa < 1$) in black ($\kappa \geq 1$). The positions of images from one of the multiple image systems used in constraining the parameters of the lenses are shown with triangles. For these contours the lens has a redshift 0.18 and the source is at redshift 3.04.

The first line opens the lens configuration file and the associated data file. Next we define the source to have a redshift of 3.04. This is important since the surface mass density contours, critical curves and caustics all depend on the redshift of the source. The output of the next 2 commands are shown in Fig. 2.1, where the image positions for the first multiple image system are shown along with the surface mass density contours as defined with levs option in the plotting routine *kappa*. The $\kappa < 1$ contours are shown in grey while $\kappa \geq 1$ are shown in black. As can be seen from the surface mass density contours the lens configuration is relatively simple (only two NSIE lenses). This example is based on the strong lensing models that will be presented in the next chapter with the difference that mass is assumed to be in only two smooth haloes.

In Fig. 2.2 we show the output of the remaining 3 commands. First we display the critical lines (and define their colour to be blue), and the caustics (the default colour
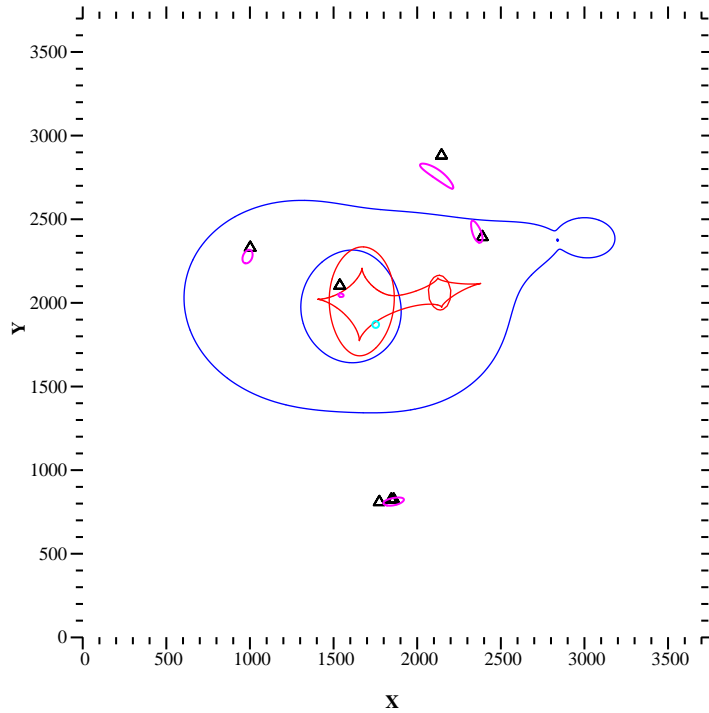
Figure 2.2: The critical curves (blue) and caustics (red) corresponding to the mass distribution shown in Fig. 2.1. Also shown is one of the multiple image systems used in constraining the parameters of the two lenses in the model (triangles). The magenta contours show the model expectations for the positions of the those multiple images, the cyan circle the unlensed source. Comparing magenta contours are clearly distorted from the circle used as the source and are significantly larger demonstrating the magnification effect of gravitational lensing.

is red). With the last command we place a circular source with a radius of 20 pixels at the mean source position of the images in image system 1. The source is shown as the cyan circle, and images of the circle are shown as magenta lines in the figure. The areas of the magenta contours show the relative magnification between the multiple images. Comparing the areas of the images to the area of the source gives the absolute magnifications of the images. The predicted images line fairly well with the input image positions shown with triangles. The reason for the offset is that the models were constrained by many more multiple image systems than just the one shown in these figures.

Chapter 3

Parametric Strong Gravitational Lensing Analysis of Abell 1689[1]

3.1 Abstract

We have derived the mass distribution of galaxy cluster Abell 1689 within 0.3 Mpc/h_{70} of the cluster centre using its strong lensing effect on 32 background galaxies, which are mapped in altogether 107 multiple images. The multiple images are based on those of Broadhurst et al. (2005a) with modifications to both include new and exclude some of the original image systems. The cluster profile is explored further out to ~ 2.5 Mpc/h_{70} with weak lensing shear measurements from Broadhurst et al. (2005b).

The masses of $\sim$200 cluster galaxies are measured with Fundamental Plane in order to accurately model the small scale mass structure in the cluster. The cluster galaxies are modelled as elliptical truncated isothermal spheres. The scaling of the truncation radii with the velocity dispersions of galaxies are assumed to match those of i) field galaxies (Hoekstra et al., 2004) and ii) theoretical expectations for galaxies in dense environments (Merritt, 1983). The dark matter component of the cluster is described by either non-singular isothermal ellipsoids (NSIE) or elliptical versions of the universal dark matter profile (ENFW). To account for substructure in the dark matter we allow for two dark matter haloes.

The fitting of a single isothermal sphere to the *smooth* DM component results in a velocity dispersion of 1450^{+39}_{-31} km/s and a core radius of 77^{+10}_{-8} kpc/h_{70} while an NFW profile has an r_{200} of 2.86±0.16 Mpc/h_{70} (M_{200}=3.2× 10^{15}M$_\odot$ h_{70}) and a concentration of $4.7^{+0.6}_{-0.5}$.

The *total* mass profile is well described by either an NSIS profile with

---

σ=1514$^{+18}_{-17}$ km/s and core radius of r_c=71±5 kpc/h$_{70}$, or an NFW profile with C=6.0±0.5 and r_{200} = 2.82 ± 0.11 Mpc/h$_{70}$ (M$_{200}$=3.0× 10^{15}M$_{\odot}$ h$_{70}$). The errors are assumed to be due to the error in assigning masses to the individual galaxies in the galaxy component. Their small size is due to the very strong constraints imposed by multiple images and the ability of the smooth dark matter component to adjust to uncertainties in the galaxy masses. The agreement in total mass profile between this work and that of Broadhurst et al. (2005a) is better than 1-σ at all radii despite the considerable differences in the methodology used.

Using the same image configuration as Broadhurst et al. (2005a) we obtain a strong lensing model that is superior to that of Broadhurst et al. (2005a) (rms of 2.7" compared to 3.2"). This is very surprising considering the larger freedom in the surface mass profile in their grid modelling. The difference is most likely a result of the careful inclusion of the cluster galaxies.

Using also weak lensing shear measurements from Broadhurst et al. (2005b) we can constrain the profile further out to $r \sim$2.5 Mpc/h$_{70}$. The best fit parameters change to σ=1499±15 km/s and r_c=66±5 kpc/h$_{70}$ for the NSIS profile and C=7.6±0.5 and r_{200} = 2.55±0.07 Mpc/h$_{70}$ (M$_{200}$=2.3× 10^{15}M$_{\odot}$ h$_{70}$) for the NFW profile.

3.2   Introduction

Abell 1689 at a redshift of 0.18 is one of the richest clusters of galaxies on the sky. Its closeness and richness should allow a straightforward mass determination using the gravitational lens effect on background galaxies, the dynamics of cluster members and the X-ray emission of the intra-cluster gas. Nevertheless, these methods have come up with strikingly different results in the past.

Observations with the *Chandra* (Xue & Wu, 2002) and *XMM-Newton* (Andersson & Madejski, 2004) satellites yield masses roughly a factor 2 lower than strong lensing measurements (e.g. Dye et al., 2001). The first line-of-sight (LOS) velocity measurements of cluster members (Teague et al., 1990) had resulted in a velocity dispersion of $\sigma \approx 2355$ km/s, compared to a value of only $\sigma \approx 1028$ km/s for a singular isothermal fit to weak lensing measurements by, for example, King et al. (2002). Therefore the singular isothermal sphere velocity dispersion estimates of the cluster from strong lensing, X-ray and weak lensing analysis originally implied a mass estimate different by a factor of up to 5.

The apparently incompatible weak and strong lensing results for an isothermal sphere are most puzzling since both methods measure the (same) line-of-sight projected two dimensional surface mass density of the cluster. If parameters obtained with these two methods on different angular scales do not agree for a given mass profile, it implies that i) the assumed mass profile does not describe the true mass distribution at all, or ii) that one analysis (more likely the weak lensing analysis) suffers from underes-

timated systematic errors. Broadhurst et al. (2005a) have shown that this is the case for A1689, i.e. that in previous analyses the contamination of the 'background galaxies' with cluster members could have biased the lensing signal of the background galaxies. Their background galaxies show (compared to Clowe & Schneider (2001); King et al. (2002)) a factor of roughly two higher lensing signal on large scales and make the order of magnitude mass estimate in the weak and strong lensing analysis agree. This discrepancy is much less in new works by Broadhurst et al. (2005b) and Bardeau et al. (2005) as well as in the reanalysis of Clowe & Schneider (2001) in Clowe (2003) in which additional filters were included and a cleaner background source catalogue was used.

The discrepant results from the cluster dynamics and the X-ray data relative to the strong lensing analysis can potentially be explained, if some assumptions in the interpretation of the dynamics of galaxies and the X-ray emitting intracluster gas, i.e. having *one* spherically symmetric isothermal structure in dynamical equilibrium, are not valid. Indeed, Girardi et al. (1997) identified three substructures (using spectroscopic data from Teague et al. (1990)) in Abell 1689 which are well separated in velocity but overlap along the line of sight. This reduced the previous value of the cluster's velocity dispersion from 2355 km/s by Teague et al. (1990) to 1429 km/s, a value in good agreement with strong lensing results. Evidence for substructure and merging was also found in velocity differences of X-ray emission lines and in X-ray temperature maps by Andersson & Madejski (2004). They pointed out that the X-ray mass estimate (lower by a factor of two) would double if two equal mass structures along the line-of-sight are responsible for the X-ray emission in stead of just one structure. The X-ray surface brightness map, however, and the weak lensing data of A1689 indicate an almost circular (2D projected) mass distribution centred on the cD galaxy. This is not necessarily contradicting the substructure results summarised above, as long as the two major contributions in mass are on the same line of sight, and each of them is a fairly relaxed structure. The issue of relax/unrelaxed systems and the cluster X-ray temperature - mass relation is studied in 10 X-ray luminous galaxies by Smith et al. (2005) using Chandra X-ray and weak and strong lensing. They find that a large fraction of their clusters are experiencing, or recovering from, a cluster-cluster merger and that the scatter in the cluster X-ray temperature - mass relation is significantly larger than expected from theory.

The current status of the strong lensing, weak lensing, the dynamical and the X-ray mass estimates for A1689 are defined by the works of Broadhurst et al. (2005a), Broadhurst et al. (2005b), Girardi et al. (1997) and Andersson & Madejski (2004) respectively. The mass estimates agree well with the exception of the still low X-ray mass estimate. The X-ray mass can be brought in line with the masses from other methods if two equal mass substructures along the LOS are responsible for the X-ray emission (Andersson & Madejski, 2004).

Broadhurst et al. (2005b) also carried out a combined strong and weak lensing analysis. They rule out a softened isothermal profile at a 10-σ level. According to their work, a universal dark matter profile (NFW) with a concentration of $C=13.7^{+1.4}_{-1.1}$ and a virial radius of $r_{vir} = 2.04 \pm 0.07\ Mpc/h_{100}$ fits the shear and magnification based on weak and strong lensing data well. For a flat universe with Ω_m=0.3 the virial overdensity with respect to the critical density is Δ_c=100. They point out that the surprisingly large concentration for A1689 together with results from other clusters could point to an unknown mechanism for the formation of galaxy clusters. The strong rejection of an isothermal sphere type profile has also been reported in galaxy cluster Cl 0024+1654 by Kneib et al. (2003) who probed the cluster profile to very large clustercentric radius (5 Mpc). They also find that both a power law profile and an NFW profile provide a good fit.

Oguri et al. (2005) however have demonstrated that halo triaxiality can lead to large apparent central concentrations, if these haloes are analysed assuming spherical symmetry. This is because a highly elongated structure along the LOS imitates a high central density if investigated in projection only. Allowing for triaxiality the central concentration is less well constrained and not in disagreement with results from numerical simulations of cluster mass profiles.

In our work we want to address the following points:

- Does one obtain the same mass profile with an analysis of the strong lensing effect using a different method? We concentrate on differences between grid method used by Broadhurst et al. (2005a) and our parametric method.

- Are mass profiles from weak (WL) and strong (SL) lensing at all compatible with each other, or does the combination of both observations already rule out an NFW or an isothermal profile?

- How much does the large concentration and the level of compatibility of the WL and SL results depend on the values of two outermost WL shear data points?

- How good is the relative performance of a non-singular isothermal sphere vs. an NFW profile, based on both the strong and weak lensing analyses?

We aim to investigate all these points with parametric cluster models. Our basic assumptions are that substructure follows galaxies and the cluster mass can be described by mass associated with the galaxies (both luminous and dark) plus a smooth component. The multiple image configurations determine if there are one or more of these smooth components necessary, e.g. two haloes of similar mass like in A370 (see e.g. Kneib et al. (1993); Abdelsalam et al. (1998)) , or a massive halo plus less massive, group-like components.

We describe the smooth component by 2 parametric halo profiles. Deviations from symmetry are accounted for by elliptical deflection angles (ENFW) or potentials (NSIE) depending on the model. The first halo profile is the so called universal dark matter profile (hereafter NFW profile), an outcome of numerical simulations of cold dark matter cosmologies (Navarro et al., 1996). The second is a non-singular isothermal ellipsoid (NSIE) which naturally reproduces the observed flat rotation curves of both late and early-type galaxies.

The profiles of cluster galaxies are described with an elliptical truncated isothermal sphere profile (Blandford & Kochanek, 1987) whose velocity dispersions are determined using both Fundamental-Plane and Faber-Jackson relations.

Provided a range of plausible radial mass profiles are tested with parametric halo profiles, a significantly better performance of grid methods, like the one used by Broadhurst et al. (2005a) (also Diego et al. (2005a,b); Zekser et al. (2006)), can give clues to the existence of dark matter substructure not traced by galaxies (dark mini haloes) if these dark haloes are numerous/massive enough to influence the lensing observables on a relevant level. The difference can also result from the details of a particular modelling, e.g. the treatment of the cluster galaxy component and the dark matter profiles used in modelling the smooth DM of the cluster.

In section 3.3 we give a brief summary of the data and data analysis used in this paper. Section 3.4 describes our method to obtain the best fitting lensing models, results are given and discussed in section 3.5. We draw conclusions in section 3.6.

The cosmology used throughout this paper is Ω_m=0.30, Ω_Λ=0.70 and H_0=70 km/s/Mpc, unless otherwise stated. With this cosmology 1" corresponds to 3.1 kpc.

3.3 Data and Data Analysis

We have used archived optical *HST* (Wide Field Planetary Camera 2, WFPC2 and Advanced Camera for Surveys, ACS) data in filters F555W and F814W (WFPC2) and F475W, F625W, F775W and F850LP (ACS). A summary of the data can be seen in Table 3.1. The limiting 2" aperture AB magnitude in the table has been estimated from the number counts of objects and where they start to depart from a power law. The relatively wide field-of-view (202x202 arcsec^2) and high resolution (pixelscale 0.05") of ACS allow us to probe A1689 over the area where most of the multiple images are formed. WFPC2 data are used to further constrain the photometric redshifts in the central region of A1689 covered by the observations.

Table 3.1: A summary of the data used in this study.

Filter	t^1 (ks)	# of exposures[2]	psf^3 ($''$)	m^4_{lim}
F555W (WFPC2)	44.2	17	0.17	27.2
F814W (WFPC2)	5.0	5	0.20	26.7
F475W (ACS)	9.5	8	0.11	27.2
F625W (ACS)	9.5	8	0.10	26.8
F775W (ACS)	9.5	8	0.10	26.6
F850LP (ACS)	16.6	14	0.11	26.3

[1] Total exposure time in kilo seconds

[2] Number of exposures combined

[3] FWHM of point sources

[4] The limiting AB 2" aperture magnitude estimated
   from the departure of number counts from a power law.

3.3.1   Data Reduction

3.3.1.1   *HST* - WFPC2

The WFPC2 data in filters F555W and F814W come from *HST* proposal 6004 by Tyson (1995). We use pipeline flatfielded images which were combined using iraf[1] tasks in combination with psf fitting cosmic ray rejection algorithms developed in house (Gössl & Riffeser, 2002). The steps of data reduction were as follows. First all features with FWHM less than 1 pixel and a high signal to noise were marked as cosmic rays and not used in any further analysis. In the second step the four chips of each WFPC2 exposure were transformed to a single coordinate system. In this step both the geometrical distortions of the WFPC2 chips as well as translation and rotation between the different CCDs and exposures were taken care off. The description of Holtzman et al. (1995) was used to remove the geometrical distortions. The different chips have slightly different photometric zeropoints and before the images were stacked all the images were normalised to the zeropoint of the planetary camera. The stacking was done by taking a kappa-sigma clipped mean of each pixel. It was found during the reduction process that the two stage cosmic ray rejection was necessary in order to remove all the cosmic rays efficiently. Most of the cosmic rays were removed by psf- fitting in the first stage and larger pointlike cosmic rays were removed in the stacking stage by the kappa-sigma clipping.

---

[1]IRAF is distributed by the National Optical Astronomy Observatories, which are operated by the Association of Universities for Research in Astronomy, Inc., under cooperative agreement with the National Science Foundation.
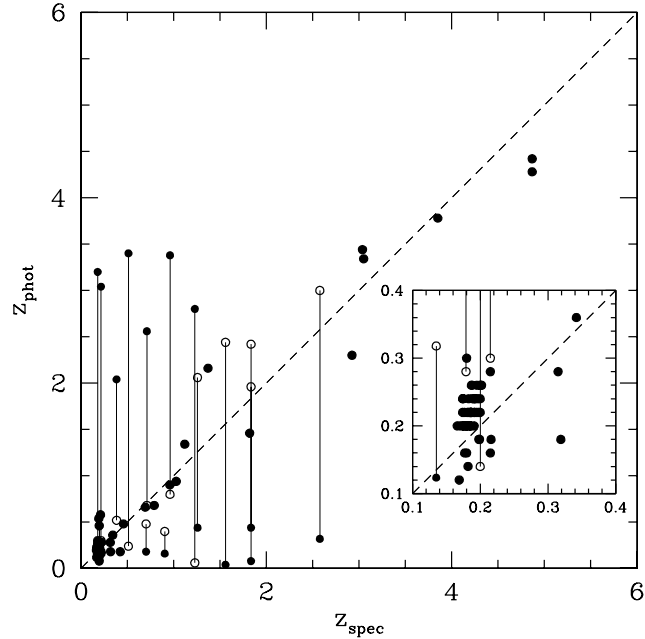
Figure 3.1: Comparison between spectroscopic and photometric redshifts. Notice how the reddest cluster ellipticals have been pushed to higher redshifts to compensate for the relative blueness of the model elliptical SED in the SED library used to compute the photometric redshifts. Filled symbols show the most likely redshift, open symbols the second most likely for the objects where it is closer to the true redshift.

3.3.1.2 *HST* - ACS

The advanced Camera for Surveys has a larger field of view than WFPC2 at a similar resolution. The data in filters F475W, F625W, F775W and F850LP come from *HST* proposal 9289 by Ford (2002). The "on the fly re-processing" (OTFR) provides flat-fielded and calibrated data. The individual exposures were transformed to a common coordinate system using PyDrizzle in pyraf. The cosmic rays were again removed in 2 stages as with the WFPC2 data.

3.3.2 Object Catalogues

The object catalogue was obtained with SExtractor (Bertin & Arnouts, 1996). To opti-mise the extraction parameters of Sextractor - detection threshold and number of con-tiguous pixels - a procedure similar to that in Heidt et al. (2003) was followed. Sources

were detected from a signal-to-noise weighted sum of the four ACS filters. The photometry for the detected sources was then done in all filters. Output of SExtractor used later in the lensing model include total and aperture photometry as well as source ellipticities and their position angles.

3.3.3   Spectroscopic redshifts[1]

The redshift data are collected from several published studies of Abell 1689 (Girardi et al. 1997, Balogh et al. 2002, Duc et al. 2002, Golse 2002[2], Frye et al. 2002). In total 84 spectroscopic redshifts were available in the ACS field of A1689. Except Golse, these studies concentrate on the line-of-sight velocities of the cluster members in order to obtain the velocity dispersion and hence an estimate of the dynamical mass of the cluster. The redshift information is used to get secure cluster members for the lensing analysis, to exclude galaxies which are not part of the cluster and to compare photometric redshifts with spectroscopic ones.

3.3.4   Photometric redshifts[3]

We have calculated photometric redshifts using the method described in Bender et al. (2001). For the central regions we were able to use all 6 filters, otherwise only the 4 available ACS filters were used. Comparison between photometric redshifts and available spectroscopic ones is shown in Fig. 3.1. Unfortunately spectroscopic redshifts are not numerous and those that exist are mainly for cluster members. The model elliptical galaxy in the spectral energy distribution (SED) library used to calculate the photometric redshifts is bluer than the reddest cluster members and hence the cluster galaxies are pushed to redshifts slightly higher than that of the cluster. The slope of the cluster redsequence causes the large spread in photometric redshifts of the cluster members. The photometric redshift distribution of all objects is shown in Fig. 3.2. The cluster appears as a narrow peak at z~0.2 on the redshift histogram. Objects at z~3-4 are either gravitationally lensed background galaxies or cluster galaxies whose 4000 Å break was misidentified as Lyman break. This places them to redshifts ~3. To

---

[1]This is an additional remark to the accepted paper. The redshift of an astronomical object can be measured very accurately from the emission and absorption lines observable in the electromagnetic spectrum of an object. From an observational point of view this is very time consuming however and is only suitable for bright objects.

[2]Available at http://tel.ccsd.cnrs.fr/documents/archives0/00/00/22/79/

[3]This is an additional remark to the accepted paper. In stead of using fine details of the spectrum it is also possible to use the gross features of the spectrum, and estimate the redshift with photometry. The errors on the derived redshifts are considerably larger than those of spectroscopic redshifts but photometric redshifts can be easily obtained for large numbers of objects. Since the lensing efficiency of the cluster (shown in Fig. 3.11) depends only weakly on the redshift already at moderate redshifts ($\lesssim$ 10% for $z > 1$) this is not going to be a limitation for the derived results.
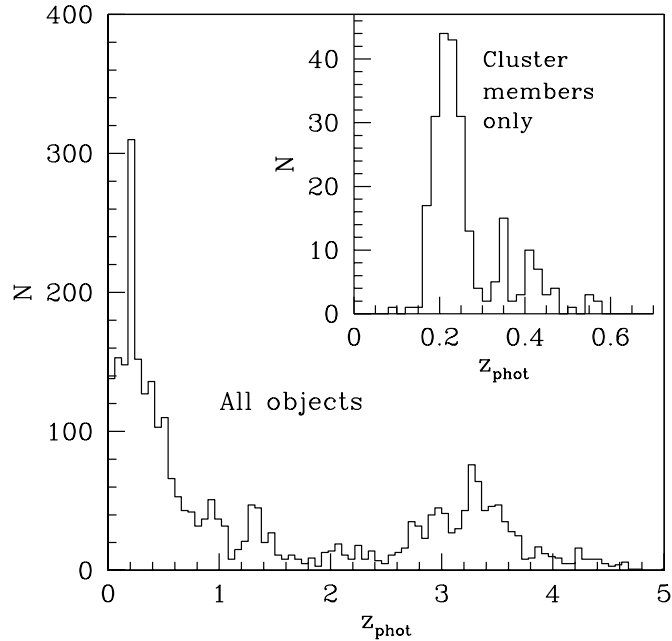
Figure 3.2: Photometric redshift distribution of objects in the field of A1689. The cluster is clearly visible as a peak at z~0.2. The inlaid figure shows objects considered as cluster galaxies. In a number of cases the 4000 Å break of cluster galaxies was misinterpreted as Lyman break and hence a redshift z~3 was assigned (see text for details).

clearly discriminate between the two breaks we would need both redder and especially bluer filters than the ones available. This confusion is not important in our case since photometric redshifts are used to constrain redshifts of the multiple images. For these the low redshift peak can be excluded because gravitational lensing is inefficient if the background source is close to the lens.

3.4 Lensing Models

In this section we describe how the lensing models of A1689 were constructed; the different mass components of the cluster, the multiple image systems and the optimisation of model parameters. The lensing profiles are described in detail in appendix 3.7.1.

3.4.1 Cluster Galaxy Component[1]

The cluster galaxies were selected using the redsequence method supported by spectroscopic redshifts where available. The spectroscopic data are taken from Girardi et al. (1997) (using data from Teague et al. (1990)), Balogh et al. (2002) and Duc et al. (2002). We have excluded 6 objects from the cluster catalogue obtained with the redsequence method based on fore/background objects listed in Balogh et al. (2002) and Duc et al. (2002). Fig. 3.3 shows a colour-magnitude diagramme of the cluster. We chose to use filters F475W and F775W from the ACS observations as the cluster redsequence is seen particularly clearly in these two filters. Galaxies included in the lensing analysis are marked by triangles in Fig. 3.3. Solid triangles show the galaxies which have been spectroscopically confirmed to be cluster members in one or more of the referred papers. To find more members a redsequence in the CM diagramme was determined by fitting a line to the bright end of the redsequence. Those galaxies whose F475W-F775W colour deviated by less than 0.3 mag from the fitted sequence were included as cluster members (region between the two inclined dashed lines in Fig. 3.3).

Fig. 3.4 shows the positions of cluster members in the field of A1689 (using the same symbols as in Fig. 3.3). The coordinate systems in all the figures of A1689 are centred on the cD galaxy at (RA +$13^h11^m29^s$.66, Sec. $-1°20'27''$.86) and has 1-b/a=0.14 ± 0.01 and a position angle 144 ± 1°.

The cluster galaxies were modelled with an elliptical BBS profile (Brainerd et al., 1996, see appendix 3.7.1 for further details). We have treated the two parameter profile as a one parameter profile by assuming that truncation radius $s = s(\sigma)$. For radii smaller than s from the galaxy centre the profile is isothermal with $\rho_{3D}(r < s) \propto r^{-2}$ where as for $r > s$, $\rho_{3D}(r > s) \propto r^{-4}$. We base our models for the tidal stripping of galaxies on observational work by Hoekstra et al. (2004) for galaxies in the field ($s \propto \sigma^2$) and theoretical expectations for galaxies in cluster environment ($s \propto \sigma$) (Merritt, 1983). We only take the scaling of the truncation radii with the velocity dispersions of the galaxies from the aforementioned works and find the normalisation of the truncation radius, s_*, to fit the multiple images. The two scaling laws adopted in the paper are then 1) $s = s_* \times (\sigma_{gal}/136km/s)^2$ and 2) $s = s_* \times (\sigma_{gal}/136km/s)$, where for both scaling laws and all Models we have found the s_* that best reproduces the observed multiple images. The scaling law for the truncation of galaxies in cluster environment will be treated in more detail in a forth coming publication (Halkola et al., 2006 in preparation). Assuming the usual scaling relations, $s = s_*(\sigma/\sigma_*)^\alpha$ and $\sigma = \sigma_*(L/L_*)^{1/4}$, with the equation for

---

[1]The work on Fundamental Plane and the determination of the galaxy velocity dispersions is done by Maurilio Pannella who is a co-author of the published paper.
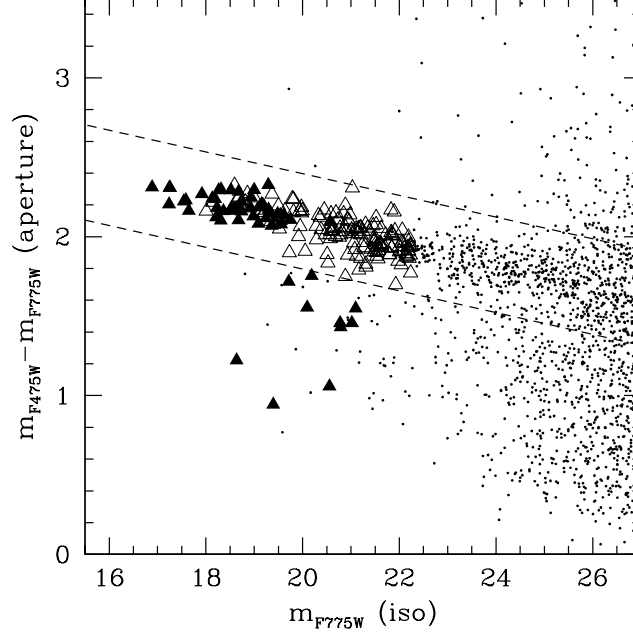
Figure 3.3: Cluster redsequence in ACS F475W/F775W colour-magnitude diagramme. Only non-stellar objects are plotted. The solid triangles represent cluster galaxies with spectroscopic redshifts, open triangles all other objects which were considered as cluster members in the lensing analysis. The remaining objects are represented by dots. A clear cluster redsequence can be seen. Galaxies fainter than 22 in F775W were not included in analysis since these have Einstein radii well below one pixel. See section 3.4.1 for details on the selection criterion for cluster membership.

the total mass of a BBS halo $M_{tot} \propto s\,\sigma^2$ we obtain,

$$M/L \propto s_* \sigma_*^2 (L/L_*)^{\alpha/4 - 1/2}. \tag{3.1}$$

This means that for $\alpha=1$ we have a constant M/L ratio where as for $\alpha=1$ M/L $\propto$ L$^{-1/4}$.

We find the fit to multiple images with a galaxy component described by the values for s_* (=185 h^{-1} kpc) and σ_* (=136 km/s) and the scaling ($s = s_* \times (\sigma/\sigma_*)^2$) found for galaxies in the Red-Sequence Cluster Survey (Hoekstra et al., 2004) is very poor. We obtain the best with s_*=~37 kpc for their scaling law. This means that the galaxy haloes in A1689 must be significantly stripped. The stripping of galaxies in cluster environment has been reported earlier by e.g. Natarajan et al. (1998, 2002) who have
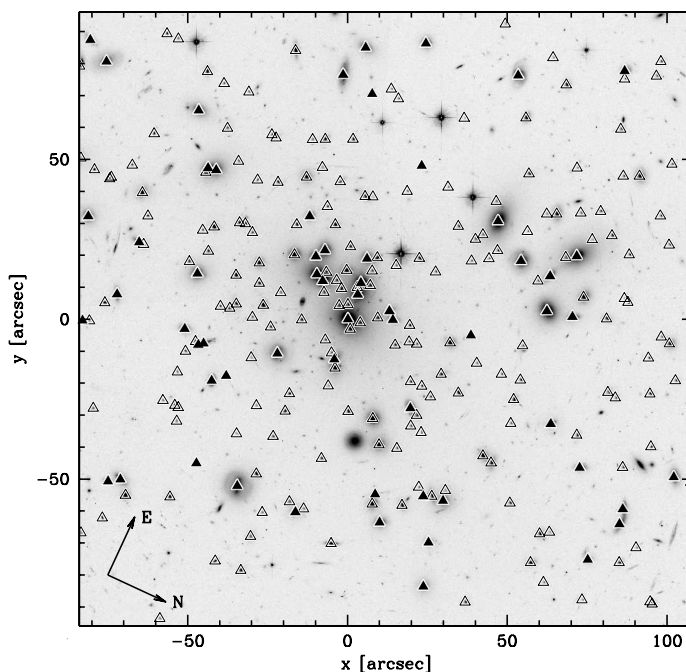
Figure 3.4: Positions of cluster galaxies in the field of Abell 1689. The symbols correspond to those in Fig. 3.3. Origin of the coordinate system is on the central cD galaxy. The box width is 200" (corresponding to ~625kpc at z=0.18).

used galaxy–galaxy lensing in clusters to study the properties of galaxy haloes in 6 clusters at redshifts Z=0.17-0.58. They found strong evidence for tidally truncated haloes around the galaxies compared to galaxies in the field. Gavazzi et al. (2004) were only able to derive upper limits in MS0302+17 due to the smoothing scale employed in their analysis.

The positions, ellipticities (of surface brightness) and position angles were taken from SExtractor output parameters. The velocity dispersions of cluster galaxies were determined mostly using the Fundamental Plane. For a small number of galaxies also the Faber-Jackson relation was used.

3.4.1.1   Central Velocity Dispersions of Cluster Galaxies & Halo Velocity Dispersions

The Fundamental Plane (hereafter FP) links together, in a tight way, kinematic (velocity dispersion), photometric (effective surface brightness) and morphological (half light radius) galaxy properties (Dressler et al., 1987; Djorgovski & Davis, 1987; Ben-

der et al., 1992). We assume that the central velocity dispersion of a galaxy, as derived from the FP, is equal to the halo velocity dispersion, and that mass in disk can be neglected.

The FP relation allows us to estimate the velocity dispersion of galaxies more accurately than the standard Faber-Jackson relation approach (Faber & Jackson, 1976). We model the 2–dimensional light profiles of cluster galaxies with PSF–convolved Sersic (Sersic, 1968) profiles using two packages, GALFIT (Peng et al., 2002) and GIM2D (Simard et al., 1999), to have a better handle on the systematics. The analysis was performed on the F775W ACS image. 176 objects with AB magnitudes brighter than 22 mag were fitted. The point spread function (PSF) used to convolve the models was derived by stacking stars identified in the field. The results coming out from the two completely different softwares agree very well.

In order to be able to use a FP determination for cluster galaxies at redshift ∼ 0.2 in restframe Gunn r filter (Jørgensen et al., 1996; Ziegler et al., 2001; Fritz et al., 2005), all the observed $F775W_{AB}$ surface brightnesses (extinction corrected) were converted to restframe Gunn r_{GT} (Thuan & Gunn, 1976) ones and corrected for the cosmological dimming. Since the observed F775W passband is close to restframe Gunn r at the redshift of A1689, the conversion factor between observed F775W and restframe Gunn r is small.

The mean observed surface brightness within r_e is:

$$\langle \mu_e \rangle_{F775W} = F775W_{observed} + 2.5\log(2\pi) + 5\log(r_e) - 10\log(1+z), \qquad (3.2)$$

where the last term corrects for the dimming due to the expansion of the Universe. It is then converted to restframe Gunn r_{GT} by:

$$\langle \bar{\mu}_e \rangle_r = \langle \bar{\mu}_e \rangle_{F775W} - A_{F775W} + K(r, F775W, z) + GT_{corr}, \qquad (3.3)$$

The Galactic extinction correction A_{F775W} is calculated from the list of A/E(B-V) in table 6 of Schlegel et al. (1998), along with their estimate of E(B-V) calculated from *COBE* and *IRAS* maps as well as the Leiden-Dwingeloo maps of HI emission. We adopted for A_{F775W} a value of 0.06.

The "k-correction colour", K(r,F775W,z), is the difference between rest frame Gunn r and observed F775W magnitude and includes also the $2.5\log(1+z)$ term. It was obtained by using an elliptical template from CWW (Coleman et al., 1980) and synthetic SEDs obtained for old stellar populations (10 Gyr, i.e. $z_f = 5$ observed at z=0.2) with the Bruzual & Charlot (2003) models. All models give a conversion factor of approximately 0.174. The correction needed to pass from the AB photometric system to the Gunn&Thuan system is $GT_{corr} \approx 0.17$.

We used the FP coefficients from Fritz et al. (2005). For the Gunn r band then

$$1.048 * \log R_e = 1.24 * \log \sigma - 0.82 * \langle I \rangle_e + ZP_{FPr}, \qquad (3.4)$$

where the $\langle I \rangle_e$ term, i.e. the mean surface brightness in units of $L_\odot/pc^2$, is given for the Gunn r band by the equation:

$$\log \langle I \rangle_e = -0.4(\langle \mu_r \rangle_e - 26.4). \qquad (3.5)$$

The zero–point of the FP ZP_{FPr} is a quantity changing with both the cluster peculiarity and, mainly, with the cluster redshift. We used for ZP_{FPr} the value published in Fritz et al. (2005). Their study was focused on A2218 and A2390, two massive clusters at almost the same redshift as A1689. They applied a bootstrap bisector method in estimating the ZP_{FPr} and relative uncertainties, finding a value of 0.055±0.022.

Finally, we inserted the values derived from our morphological fitting procedures into the FP relation. The uncertainties on the derived velocity dispersions were estimated by taking into account the errors on the morphological parameters, the propagated photometric uncertainties, the error on the ZP_{FPr} value and the intrinsic scatter of the FP relation, which gives the main contribution. We found that an estimate of 0.1 in $\log(\sigma)$ is a good value for the total uncertainty in velocity dispersion for objects having a velocity dispersion greater than 70 km/s. For lower velocity dispersions down to 24 km/s, we assumed an overall uncertainty of 0.2 dex. The fitted parameters for the 80 most massive galaxies are tabulated in Table 3.7.

A comparison between total observed magnitude - σ relations in three clusters at redshift ~0.2 are shown in Fig. 3.5. Red points are measured values taken from Ziegler et al. (2001) for A2218 (z=0.18), green points are values taken from Fritz et al. (2005) for A2390 (z=0.23) and full (empty) black points refer to the velocity dispersion estimates obtained in this paper for A1689 using the GIM2D (GALFIT) morphology. The literature values have been transformed to F775W$_{AB}$ magnitudes by applying relatively small colour terms (0.04,-0.4) and the AB correction (0.4).

Additionally, we have obtained the velocity dispersions of 26 galaxies using the Faber-Jackson relations derived using the 176 galaxies for which we have obtained the velocity dispersions via FP. These are all faint galaxies with $\sigma <$60 km/s.

The Einstein-radius of an isothermal sphere can then be written as $\theta_E = 1.4''(\sigma/220 km/s)^2$ D, where D is a geometrical factor of order unity depending on redshifts of the objects and cosmology (0.78 < D < 0.92 for $1 < z_s < 6$ and our adopted cosmology). The pixelscale of the ACS camera on the *HST* is 0.05"/pixel and so 1.4"corresponds to 28 pixels. Cluster members with $\sigma > 24$ km/s were included in the galaxy component of the cluster. This limit is somewhat arbitrary and below the luminosity limit where FP and FJ are determined. An Einstein radius smaller than the pixel size of the ACS ensures that all galaxies which could significantly affect image morphologies locally are included when external shear and convergence from the other cluster galaxies and the cluster halo are present.
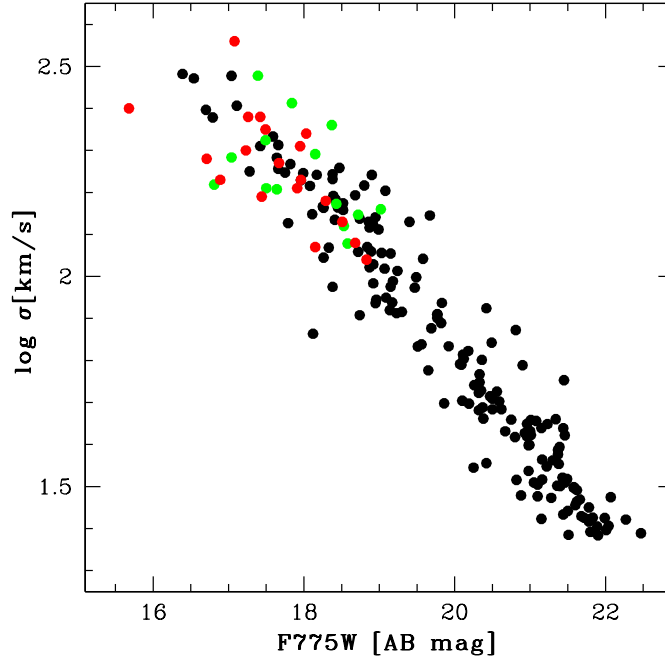
Figure 3.5: Total observed magnitude - σ relation for three z~0.2 clusters. Red points are measured values taken from Ziegler et al. (2001) for A2218 (z=0.18), green points are values taken from Fritz et al. (2005) for A2390 (z=0.23) and full (empty) black points refer to the velocity dispersion estimates obtained in this paper for A1689 using the GIM2D (GALFIT) morphology. The literature values have been transformed to $F775W_{AB}$ magnitudes by applying relatively small colour terms (0.04,-0.4) and the AB correction (0.4).

3.4.1.2 Ellipticities of Cluster Galaxies and Their Haloes

Blandford & Kochanek (1987), Kormann et al. (1994) and others have noted that for elliptical potentials the accompanying surface mass density can have negative values. We have used elliptical potential for our NSIE profile since it is straightforward to implement (all parameters of interest can be calculated from the analytic derivatives of the potential). An alternative approach is to have an elliptical mass distribution as demonstrated by Kormann et al. (1994) but the expressions for α, κ and γ are considerably more complicated.

For the ENFW and BBS profiles we have introduced the ellipticity to the deflection angle, see appendix 3.7.1 for details and references. The effect of using an elliptical deflection angle instead of an elliptical mass distribution is shown in Fig. 3.6. The

ellipticities of the mass distributions were estimated by fitting an ellipse to $\kappa=0.2$ isodensity contours for both BBS (top) and ENFW (bottom) haloes with 6 different ellipticities (0, 0.05, 0.1, 0.15, 0.2 and 0.25). On the right panel a quarter of the $\kappa=0.2$ isodensity contour for different profile ellipticities are drawn in solid. Dashed lines show the best fit ellipses. For the BBS model the isodensity contours start to deviate from an ellipse at $\epsilon_{\text{defl}} > 0.15$, where the contours first appear boxy before turning peanut shaped. For the ENFW profile the contours are only slightly peanut shaped at $\epsilon_{\text{pot}}=0.25$. Left panels of Fig. 3.6 show how the ellipticity of mass deviates from $\epsilon_{\text{kappa}}=2\epsilon_{\text{defl}}$ and $\epsilon_{\text{kappa}}=3\epsilon_{\text{defl}}$ lines shown dashed. We have assumed that light and mass have the same ellipticity and used the relation in Fig. 3.6 to convert the measured galaxy ellipticities (ϵ_{kappa}) to BBS model ellipticities (ϵ_{defl}). A histogram of the ellipticities of the included cluster galaxies are shown in Fig. 3.7.

3.4.2   Dark Matter Not Associated with Galaxies

Different studies have shown that Abell 1689 is not a simple structure with only one component. In an early strong lensing analysis of A1689 Miralda-Escude (1995) assumed two halo components based on the distribution of galaxies. Girardi et al. (1997), on the other hand, spectroscopically identified three distinct groups in Abell 1689. More recently Andersson & Madejski (2004) have also found evidence for substructure and possible merger in X-ray data. This prompted us to model the cluster dark matter in A1689 with two dark matter haloes. The use of more haloes in the modelling is not desired since this increases problems related to a large number-of free parameters; larger parameter space to explore, increased difficulty of finding global minimum and degeneracies between the free parameters. Both haloes have 6 free parameters: position (x,y), ellipticity, position angle and in the case of NSIE profile velocity dispersion σ and core radius r_c and for the NFW profile virial radius r_{200} and concentration parameter C.

For all the following modelling we have constrained the first halo to reside within 50" in x and y from the cD galaxy in order to reduce the volume of the parameter space and to reduce the degeneracy between the parameters of the two haloes. We do not want to tightly connect the halo with any of the galaxies but use the position of the cD as a first guess for the position of the cluster centre. This is supported by X-ray maps of Abell 1689 (Xue & Wu, 2002; Andersson & Madejski, 2004) as well as weak lensing studies (King et al., 2002) which place the centre of the mass distribution very near the cD galaxy. The position of the second halo was initially set to coincide with the visually identified substructure to the north-east of the cluster centre but was left unconstrained in the optimisation.
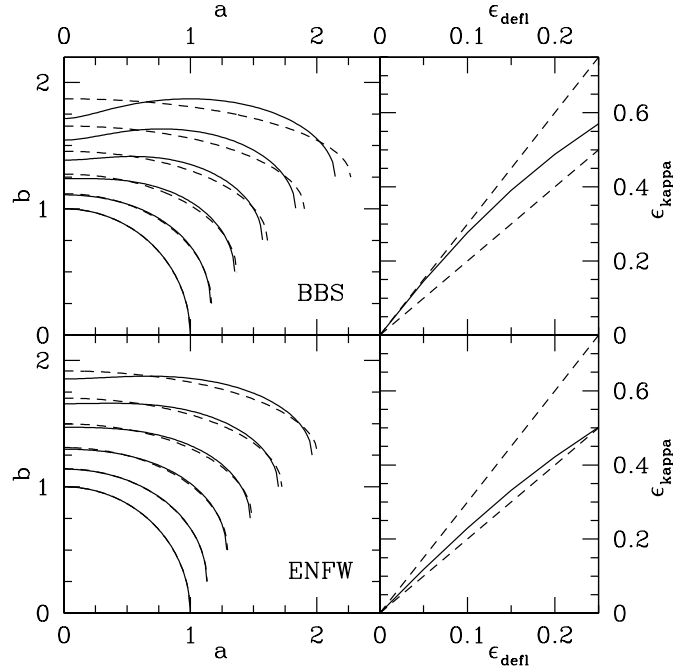
Figure 3.6: Ellipticity of surface mass density vs. profile ellipticity (in deflection angle) for the two profiles (BBS is on the top two panels and ENFW on the bottom two). The ellipticity of κ is estimated by fitting an ellipse to lines of constant surface mass density. Right panels show κ=0.2 isodensity contours in solid and fitted ellipses in dashed lines. Profile ellipticities are 0.0, 0.05, 0.10, 0.15, 0.20, 0.25 and increase from bottom to top. The curves have an offset of 0.25 in b for clarity. Left panels show ϵ_{kappa} as a function of profile ellipticity ϵ_{defl}. The dashed lines are $\epsilon_{kappa} = 3\ \epsilon_{defl}$ and $\epsilon_{kappa} = 2\ \epsilon_{defl}$ lines.

3.4.3 Multiple Images & Arcs

It is evidently of great importance for the modelling to find as many multiple images as possible. The colour and surface brightness of an object are unaffected by gravitational lensing and we have hence used the colour, surface brightness and the morphology of the images to identify multiple image systems. We have first identified arcs and obvious multiple images which were then used to find an initial set of halo parameters. Initial constraints include images from image systems 1, 3, 4, 5, 6, 12 and arcs that contain images systems 8, 14, 20 and 32. A model based on these images could now be used to search for more images for the existing image systems as well as new image systems which could be included in the model and constrain the model parameters further. New images were searched for by looking for image positions whose source
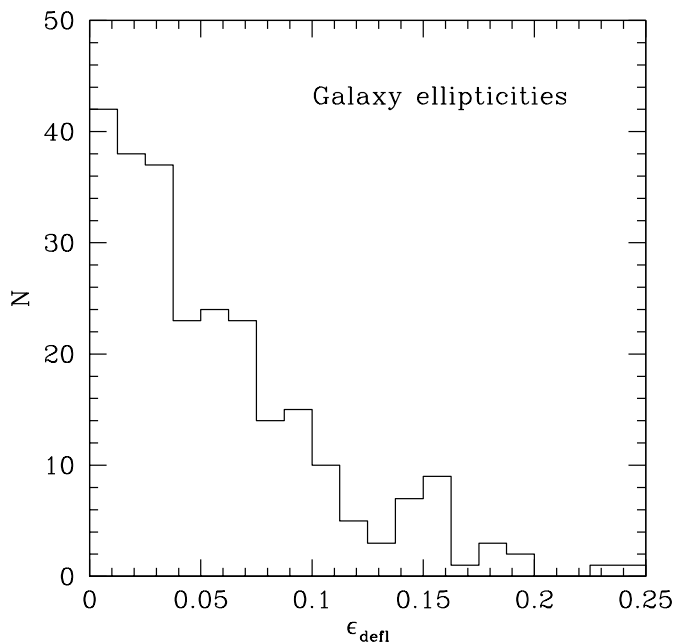
Figure 3.7: A histogram of the ellipticities, ϵ_{defl}, for the BBS profiles used to model the cluster galaxies. Most of the galaxies have an ellipticity well below 0.15 where the isodensity contours of surface mass density start to appear peanut shaped.

lies within a specified distance, e.g. 5", from the source of an existing image. This method is basically the same as described in Schramm & Kayser (1987) and Kayser & Schramm (1988).

The images we have found are with a few exceptions also identified in the pioneering work of Broadhurst et al. (2005a). For our analysis we have merged the two image catalogues to obtain a catalogue of 107 multiple images in 32 image systems one of which is an long arc. In the merging we have split the image system 12 from Broadhurst et al. (2005a) to two separate systems (12 and 13) with 2 additional images from our catalogue. The splitting includes separating two images with the same spectroscopic redshift into two different image systems. We have done this based on the morphology of the images and our lensing models and we believe these to originate from 2 different sources. Also Seitz et al. (1998) in their analysis of cluster MS-1512 reported two sources at the same redshift. In the case of MS-1512 Teplitz et al. (2004) used near-infrared spectroscopy to confirm that the sources were indeed separate with a difference of only 400 km/s in velocity (0.0013 in redshift). To positively identify a set of images to originate from a single source is very difficult without extremely accurate

spectroscopy or obviously the same (complex) morphology. The field of A1689 has a vast number of images that can potentially be erroneously assigned to any multiple image system. In our work we have rather excluded an image than include it in an image system. For this reason we have also excluded image system 20 from Broadhurst et al. (2005a) from our analysis. Image systems not used by Broadhurst et al. (2005a) are systems 31 and 32, a system with 2 images and a long arc respectively.

Eight of the image systems used have an even number of images. The missing images in these cases are always demagnified, and based on the lensing models mostly, are expected to lie near a galaxy making their identification very difficult.

In Fig. 3.8 we show all the multiple images used in this study. More details, such as positions and redshifts, of the image systems, arcs and images can be found in Appendix 3.7.3 Tables 3.8 and 3.9 as well as Broadhurst et al. (2005a). The redshifts of the multiple images were estimated using the values from both this work and that of Broadhurst et al. (2005a) where possible. Secure spectroscopic redshifts come from Golse (2002) and Frye et al. (2002). The redshift of image system 10 is taken from Broadhurst et al. (2005a) who in turn have taken it from Fort et al. (1997). We have not been able to confirm the validity of the redshift but have used in the analysis although the use of it is debatable.

A comparison between photometric redshifts from this work and those of Broadhurst et al. (2005a) is shown in Fig. 3.9. The overall agreement is very good. The one object with a z~1 from Broadhurst et al. (2005a) and z~3.4 from this work belongs to image system 1 and is one of the few objects with a spectroscopic redshift (z_{spec}=3.0).

In Fig. 3.10 we show the photometric redshift probability density of the 5 multiple image systems with a spectroscopically known redshift. In the figures the different colours represent the probability densities of individual multiple images of the system. In most of the cases the spectroscopic and photometric redshifts agree very well. Only image systems 10 and 12 have a broad photometric redshift probability density distribution.

The lensing power of a cluster depends on the ratio D_{ds}/D_s, where D_{ds} is the angular diameter distance between the cluster and the source and D_s is the angular diameter distance of the source. In Fig. 3.11 we show the power of a lens at redshift 0.18 for different source redshifts. Vertical lines in Fig. 3.11 show the range of allowed D_{ds}/D_s ratios for the image systems with photometric redshifts. The five squares mark the image systems with known redshifts (two have the same redshift). The D_{ds}/D_s ratio can be well constrained by photometric redshifts alone. With the help of the five spectroscopic redshifts we can very accurately separate the geometric factor from the deflection angle allowing us to constrain the cluster mass tightly.
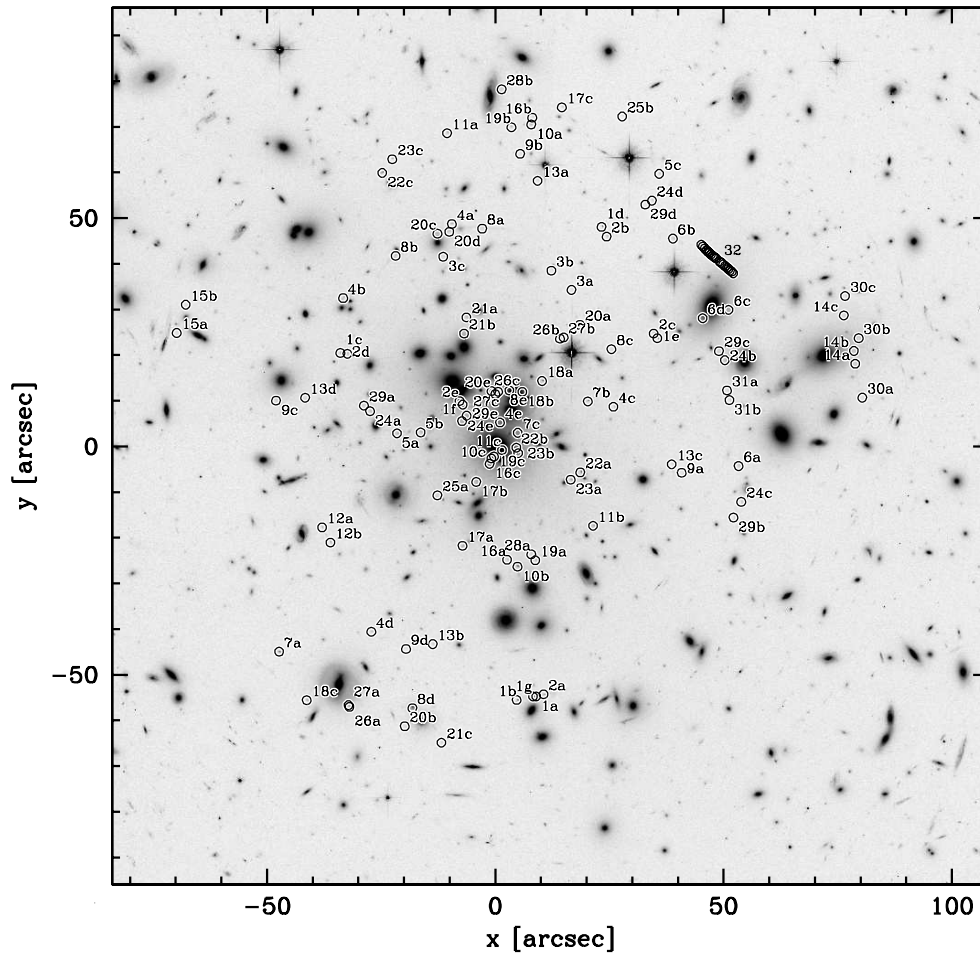
Figure 3.8: Positions of multiple images used in constraining the model parameters. The images from each multiple image system have the same number, the images within an image system are coded with letters. The box side is ~600 kpc with our cosmology.
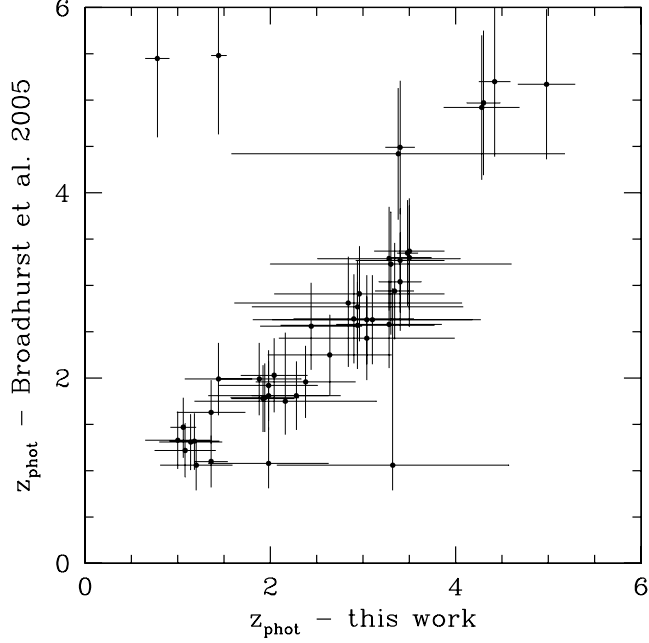
Figure 3.9: A comparison of photometric redshifts of multiple images from this work to those from Broadhurst et al. (2005a). The correspondence is very good and for most objects within the errors. The one object with a $z_{phot} \sim 1$ from Broadhurst et al. (2005a) and $z_{phot} \sim 3.4$ from this work has a spectroscopic redshift of $z_{spec} = 3.04$.

3.4.4   Finding Optimal Model Parameters

Goodness of fit in strong gravitational lensing can be quantified in two ways. The proper way is to calculate a χ^2 in the image plane, i.e. how far an image predicted by a model is from the observed one. In calculating the positions of predicted images of an image system we assume that the images of a system originate from the average source of the images. The expression for an image plane χ^2 is then

$$\chi^2 = \sum_k \sum_i \frac{|\boldsymbol{\theta}_{k,i} - \boldsymbol{\theta}_i(<\boldsymbol{\beta}_{k,i}>)|^2}{\sigma_k^2},\tag{3.6}$$

where $\boldsymbol{\theta}_{k,i}$ is the position of image i in image system k and $\boldsymbol{\theta}_i(<\boldsymbol{\beta}_{k,i}>)$ is the predicted image position corresponding to image at $\boldsymbol{\theta}_{k,i}$ from mean source of system k at
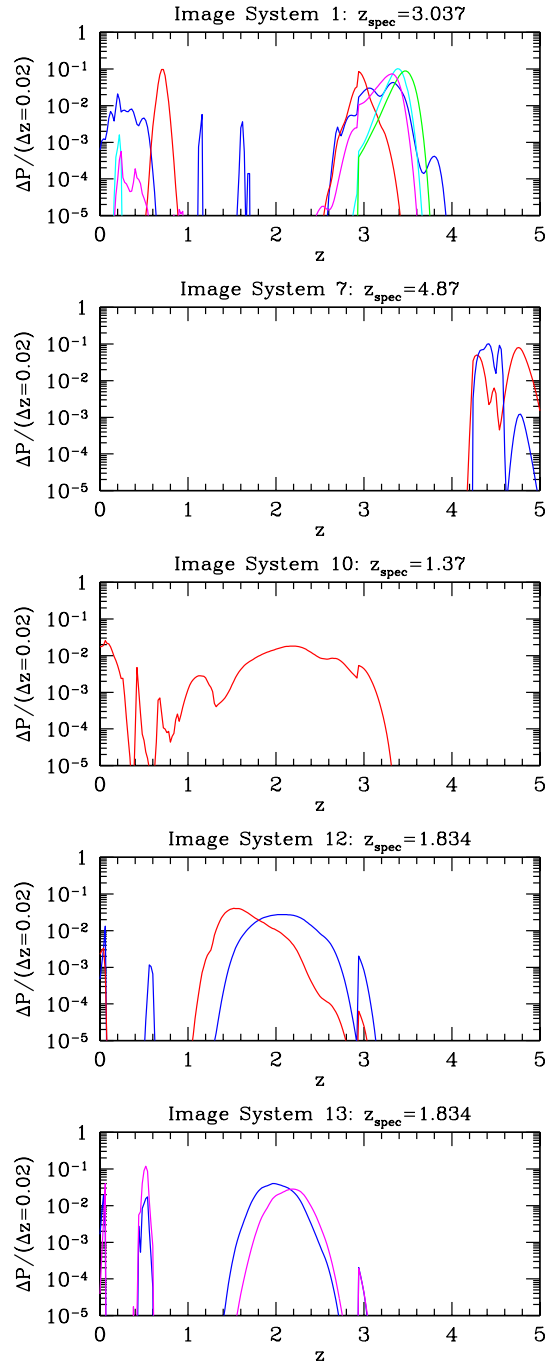
Figure 3.10: Photometric redshift probability density for the 5 image systems where spectroscopic redshift is known for at least one of the images in the system. In each panel the coloured thin lines represent individual redshift probability densities for the images in the system. Only image systems 10 and 12 have a broad photometric redshift probability density distribution, the other spectroscopic redshifts are recovered well.
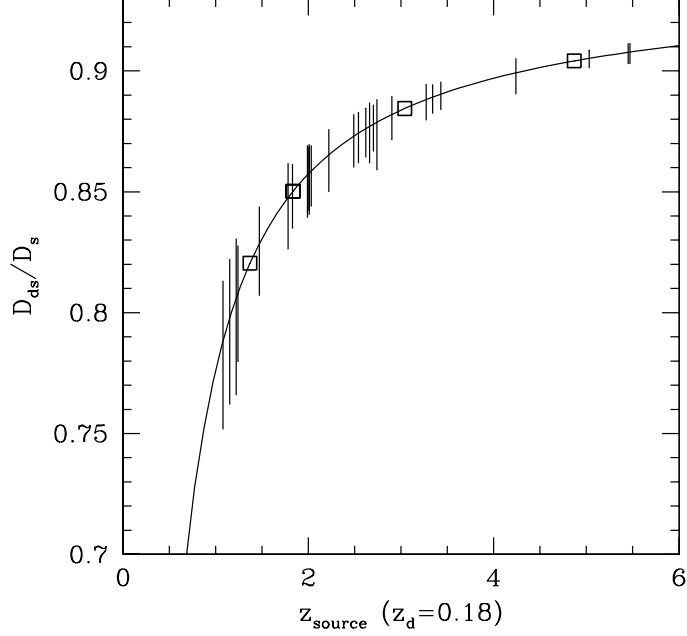
Figure 3.11: The lensing power of a cluster depends on the ratio D_{ds}/D_s, where D_{ds} is the angular diameter distance between the cluster and the source and D_s is the angular diameter distance of the source. This ratio flattens rapidly for redshifts larger than 0.5 (for a cluster at redshift 0.18). In the figure we show the allowed D_{ds}/D_s ratios of the different multiple image systems. The squares indicate objects with spectroscopic redshifts. Since D_{ds}/D_s varies only little for z>2 the redshifts of sources are not of great importance. The spectroscopic redshifts are important in fixing the overall mass scale.

$< \beta_{k,i} >$ and σ_k is the error in image positions for system k (estimated to be 1 pixel for all images).

Calculating image plane χ^2 is unfortunately very time consuming since the lens equation needs to be inverted numerically. An additional complication is that for some values of the model parameters not all observed images necessarily exist. This means that an image plane χ^2 does not necessarily converge to the optimal parameters but is trapped in a local minimum.

Goodness of fit can also be estimated by requiring that all images of an image system originate from the same source and hence minimise the dispersion of the source positions. The problem in this case is that the errors are measured in the image plane and do not necessarily represent the errors in source positions. We take account of

this by rescaling errors in the image plane with local magnification. Rescaling by magnification largely avoids bias towards cluster parameters with high magnification (large core radius for the NSIE model or small concentration for ENFW model). The source plane χ^2, $\widetilde{\chi}^2$, can be written in the following way,

$$\widetilde{\chi}^2 = 2 \sum_k \sum_i \sum_{j>i} \frac{|\boldsymbol{\beta}_{k,i} - \boldsymbol{\beta}_{k,j}|^2}{\sigma_{k,i}^2/\mu_{k,i} + \sigma_{k,j}^2/\mu_{k,j}}, \tag{3.7}$$

where $\boldsymbol{\beta}_{k,i}$ is the source position of image i in system k, $\sigma_{k,i}$ is the error in the corresponding image position and $\mu_{k,i}$ is the local image magnification.

The advantage of $\widetilde{\chi}^2$ over χ^2 is that for every image position it is always possible to calculate a corresponding source position and so $\widetilde{\chi}^2$ can be calculated for all values of the model parameters making $\widetilde{\chi}^2$ converge well.

To find optimal model parameters we have first minimised $\widetilde{\chi}^2$ to obtain model parameters close to the optimal ones to ensure that the identified multiple images can be reproduced by the models. The optimal model parameters were then found by minimising χ^2 properly in the image plane.

3.4.5 Degeneracies

Any multiple image system can only constrain the mass contained within the images. This leads to degeneracies in the derived surface mass profile: the so called mass sheet degeneracy states that if a given surface mass density satisfies image constraints then a new surface mass density can be found, by suitably rescaling this surface mass density and by adding a constant mass sheet, which satisfies image positions as well as relative magnifications equally well.

For haloes with variable mass profile this can also create a degeneracy between the parameters of the profile. For the NSIE model a high core radius can be compensated for by a larger velocity dispersion and for NFW a higher scale radius demands a lower concentration parameter.

These degeneracies can be broken if multiple image systems at different redshifts and at different radii can be found. Position of a radial critical line, and so radial arcs, depends critically on the mass distribution in the central regions and hence the core radius. On the other hand tangential arcs give strong constraints on the mass on larger scales. Well defined halo parameters can be determined by having radial arcs, a large number of multiple images at different redshifts and by minimising in the image plane.

3.5   Constructing Lensing Models

We have constructed in total 4 strong lensing models for the cluster. The mass distributions are composed of two components as described in the previous section: the cluster galaxies and a smooth dark matter component. They give us the best fitting NSIE and ENFW parameters for the *smooth* dark matter component and the mass profile of the different mass components as well the total mass profile of the cluster. With Models I and II we aim to establish a well defined total mass profile for the cluster using the multiple image positions and the photometric redshifts of the sources. The difference between Models I and II is in the scaling law used for the cluster galaxies. Model I assumes a $s \propto \sigma^2$ law where as for Model II we use $s \propto \sigma$ law. Models Ib and IIb replicate the setup of Broadhurst et al. (2005a) and with these we want to compare results of our parametric models to those of their more flexible kappa-in-a-grid model. For Models Ib and IIb we have used images from Broadhurst et al. (2005a) only and have left the photometric redshifts of the sources free as was done in Broadhurst et al. (2005a). We have kept the spectroscopic redshifts fixed as these help to define the mass scale of the cluster. The difference between Models Ib and IIb is again in the scaling law adopted.

In addition to the 4 strong lensing Models above we have also constructed 2 further Models in order to derive NSIS and NFW parameters of the total cluster mass profile and to facilitate the comparison of our results with earlier methods used to measure cluster masses, and numerical simulations. In Model III we have fitted a NSIS and an NFW profile to the total mass obtained with Models I and II. With Model IV we combine the strong lensing constraints from Model III and the weak lensing constraints from Broadhurst et al. (2005b) and derive accurate NSIS and NFW parameters for the total mass profile out to ~15' (~2.5 Mpc).

Most of the image systems are very well reproduced by the Models. Image systems 8, 12, 14, 15, 30, 31 and 32 are located close to critical lines where the image plane χ^2 is difficult to calculate due to ill determined image positions from the models. For these image systems we have always calculated the χ^2 in the source plane.

We quantify the quality of fit by the rms distance between an observed image position and one predicted by the models. For the images systems mentioned above the magnification weighted source separation was used instead. The rms distance between an image in an image system and the image position obtained with the models are given for each image system in Table 3.8 in the Appendix.

Additional information of the fit quality can be seen in appendix 3.7.4 where we show image stamps of all multiple images. In addition to the multiple images we also show two model reproductions for each image obtained with the two descriptions of the smooth dark matter component (NSIE and ENFW) for Model II.

Fig. 3.12 shows the total surface-mass-density contours obtained with Models I and II for the two smooth DM profiles. For each smooth DM profile we plot the mean κ of the in total 4000 cluster realisations used in deriving the best fit

parameters and errors. The dotted contours are for the NSIE and the dashed contours are for the ENFW profile. The contours are drawn at κ=0.25, 0.50, 1.0 and 2.0 levels for a source redshift of 1. The thin contour lines are for κ <1 and thick lines for $\kappa \geq 1$.

Fig. 3.13 shows the critical curves obtained with Models I and II for the two smooth DM profiles. For each smooth DM profile we plot the critical curves of the average cluster of the in total 4000 cluster realisations used in deriving the best fit parameters and errors. The dotted contours are for the NSIE and the dashed contours are for the ENFW profile. The thin contours are drawn for a source redshift of 1 and the thick contours for a source redshift of 5.

3.5.1   Models I and II: Strong Lensing Mass Reconstruction

The first two strong lensing models aim to establish a total mass profile for further analysis. The smooth dark matter component of the cluster mass was modelled in exactly the same way for both models (detailed in section 3.4), for the galaxy component we vary the scaling of the truncation radius of the BBS model with the velocity dispersion. For Model I we have assumed that the galaxies follow a scaling law similar to the field galaxies, namely that the truncation radius s of a galaxy scales like $s = s_* \times (\sigma/136 \, km/s)^2$ with the velocity dispersion σ of the galaxy. For Model II we have assumed a scaling law expected for galaxies in cluster, $s = s_* \times (\sigma/136 \, km/s)$. The normalisation of the scaling law for each Model and smooth DM profile is shown in Table 3.2. The haloes are strongly truncated. This is a real effect but the actual values obtained for s_* can be affected by the optimisation process. Mass lost from galaxies due to truncation can in part be compensated by the smooth dark matter component, leading to possibly significant uncertainties in the truncation radii. It is not our aim in this paper to attempt to constrain the truncation radii of the galaxies in the cluster but instead to reproduce the observed multiple images as accurately as possible. The truncation of galaxies in a cluster environment will be discussed in detail in a forth coming publication (Halkola et al., 2006 in preparation).

The constraints for Models I and II are the positions of the multiple images and their redshifts. The redshifts of sources were allowed to find the optimal redshift within the 1-σ errors of the photometric redshifts, except sources with spectroscopic redshifts for which we have fixed the redshift to the measured one. The allowed ranges for the source redshifts are tabulated in Table 3.8 in appendix 3.7.3.

The best fit parameters for the smooth dark matter component of the models are summarised in Table 3.2. The errors are caused by errors in determining the correct galaxy masses and in measuring the multiple image position. The derivation of errors is explained in section 3.5.3.

Our best fitting model is Model I with a dark matter component described by an ENFW profile. The differences in the fit quality between the models and smooth dark
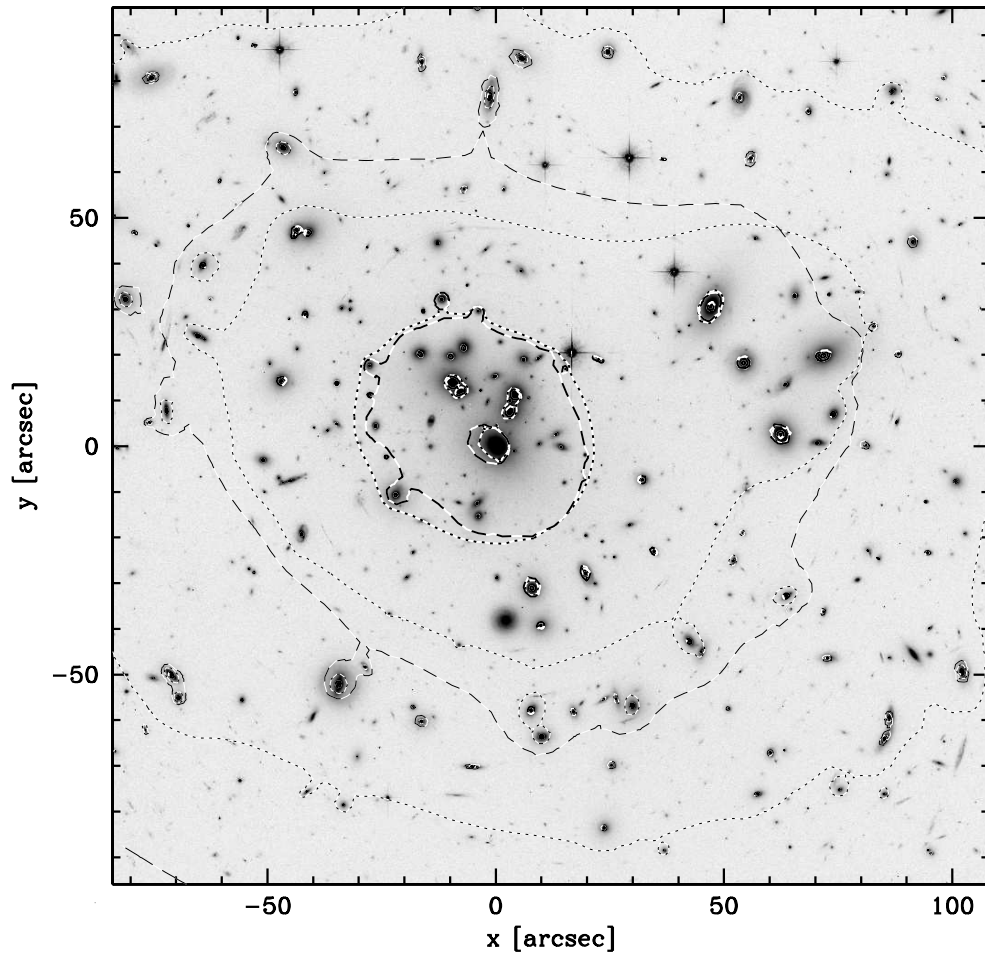
Figure 3.12: Surface mass density contours for NSIE (dotted) and ENFW (dashed) profiles for Model I. For each smooth DM profile we plot the mean κ of the in total 4000 cluster realisations used in deriving the best fit parameters and errors. The contours are drawn at κ=0.25, 0.50, 1.00 and 2.00 levels for a source at redshift of 1.0. The thin contour lines are for $\kappa <1$ and thick lines for $\kappa \geq 1$. The secondary mass concentration on the upper right can also be seen clearly in the surface mass density contours.
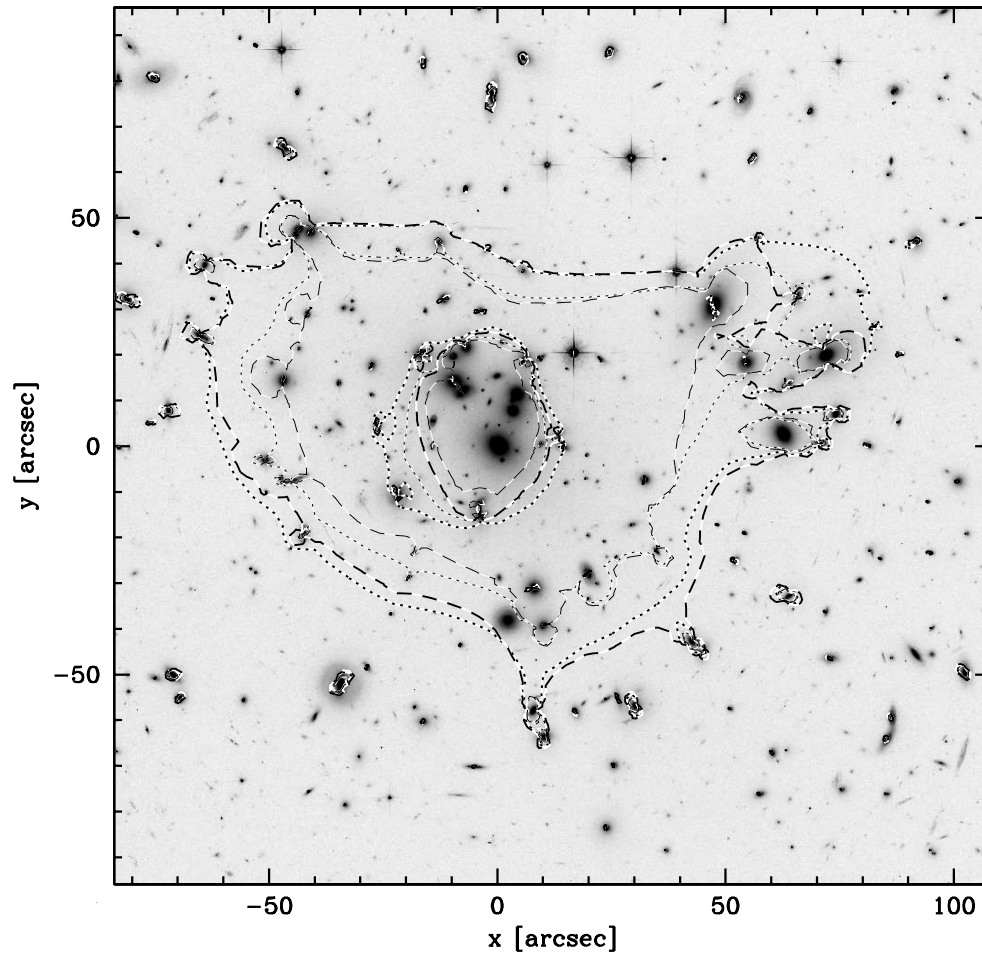
Figure 3.13: The critical curves obtained with Models I and II for the two smooth DM profiles. For each smooth DM profile we plot the critical curves of the average cluster of the cluster realisations used in deriving the best fit parameters and errors. The dotted contours are for the NSIE and the dashed contours are for the ENFW profile. The thin contours are drawn for a source redshift of 1 and the thick contours for a source redshift of 5.

matter profiles used are generally small as can be seen from Table 3.2 although both Models perform better when the smooth DM is modelled with an ENFW profile. The fit quality is 0.5" better than that achieved by Broadhurst et al. (2005a) in their analysis of the cluster. This can be due to better modelling of the cluster mass or to a different set of multiple images used. If the difference is due to the changes in multiple image systems then the χ^2 in the case Broadhurst et al. (2005a) of is driven by a only a few image systems since most of the images systems are infact identical. Another difference are the constraints imposed on the redshifts of the images in our modelling.

3.5.2 Models Ib and IIb: Comparison to Broadhurst et al. 2005

In order to directly compare the performance of our parametric models to the grid model of Broadhurst et al. (2005a) we have constructed two further models that mimic their setup. The models are constrained only by the multiple image positions from Broadhurst et al. (2005a); the photometric redshifts of the images were thus ignored and were included as free parameters. We have fixed the spectroscopic redshifts however since it is necessary to define an overall mass scale for the cluster. The rest of the modelling is identical to that of Models I and II. The results for Models Ib and IIb are shown in Table 3.3.

The very good performance of our models relative to Broadhurst et al. (2005a) is remarkable considering the large freedom in the mass profile allowed in their modelling. This also means that the mass profile can be very well described by parametric models making the additional freedom allowed by non-parametric mass modelling unnecessary, even undesirable if one is interested in comparing the performance of different parametric mass profiles.

Assuming that the smooth mass component of Broadhurst et al. (2005a) is able to reproduce both NSIE and ENFW halo profiles the other major difference between our mass modelling and that of Broadhurst et al. (2005a) is in the treatment of the galaxy component. The assumptions needed on the properties of the cluster galaxies in our modelling seem to be well justified based on the superior performance of our models.

3.5.3 Estimation of Errors in the Parameters of the Smooth Dark Matter Component

Our primary source of uncertainty in the parameters of the smooth dark matter component are the velocity dispersions of the galaxies in the cluster.

In order to estimate the effect of measurement errors in the cluster galaxy component on the parameters of the smooth cluster component, we have created 2000 clusters for Models I, II, Ib and IIb and the two profiles by varying the velocity dispersions of cluster galaxies and positions of multiple images by the estimated measurement errors.

For each galaxy we have assigned a new velocity dispersion from a Gaussian distribution centred on the measured values with a spread corresponding to the error. The truncation radii of the cluster galaxies were adjusted accordingly. For the scaling law we have used the normalisation as for the original cluster galaxies. New positions for the multiple images were assigned similarly by assigning new positions from a Gaussian distribution centred on the measured positions.

Optimal parameters for the smooth cluster component for each cluster were found by minimising $\widetilde{\chi}^2$ in the source plane due to the large number of minimisations required. However, in all subsequent analysis we have used the image plane χ^2 calculated after the optimal parameters in the source plane were found.

To justify the use of $\widetilde{\chi}^2$ instead of χ^2 in the error estimation, we show in Fig. 3.14 the final χ^2 against $\widetilde{\chi}^2$ for a large number of models after minimising $\widetilde{\chi}^2$. In the figure both χ^2 and $\widetilde{\chi}^2$ have been scaled by the minimum $\widetilde{\chi}^2$ of the models. The good correspondence between the two, even at high values of χ^2, and that $\chi^2(\widetilde{\chi}^2)$ is a monotonically increasing function (unfortunately with some scatter) gives us confidence in the source plane minimisation and our error analysis.

The optimal parameters of the generated clusters have a spread around the best fit parameters determined for the 'real' cluster. The number density of the optimal parameters in the parameter space cannot be directly used to quantify the random error since areas of high density could in fact also include a large number of relatively poor fits to the data. To include also information of the quality of fit we weight each realisation of the Monte-Carlo simulation with the final $1/\chi^2$ of the realisation. In Fig. 3.15 we show the number density contours for the NSIE (top panel) and ENFW (bottom panel) halo parameters of the realisations after weighting by the final $1/\chi^2$. The solid lines are for Model I and the dashed lines for Model II. The contour lines show the regions in which 68 and 95 per cent of the weighted realisations lie.

3.5.4   Model III: Parameters for the Total Mass Profile

It is important to realise that the multiple images constrain the combined mass of the cluster, be it baryonic or dark. The division of the mass to two components is done in order to take the mass we can observe into account as accurately as possible. The uncertainty of the description of the galaxy component is reflected in how well we can determine the profile parameters of the smooth dark matter component. The parameters for the total mass distribution, constrained directly by the multiple images, can be determined significantly better. For this reason we have also fitted single NFW and NSIS haloes to the total mass obtained from Models I and II.

We estimate the total mass profile of the cluster by combining all mass profiles from the error analysis. In Fig. 3.16 we show the 68.3 per cent confidence regions of mass for the two mass components and the total mass. The galaxy component is

Table 3.2: Best fit halo parameters of the smooth dark matter components for Models I and II. The rms error quoted for each model and halo type is the rms distance between the measured image positions and those predicted by the models expect for image systems where the calculations of an image plane χ^2 was not possible (8, 12, 14, 15, 30, 31 and 32) for which we have used the source plane χ^2 defined in equation 3.7. The values given are for the best fitting halo optimised in the image plane. The values in brackets refer to the mean values obtained from the simulations (optimised in the source plane), the errors in the halo parameters are derived from the spread of the values in the simulations. For details of the models and error derivation see text body.

	Model I		Model II	
NSIE	rms error 3.17" (3.51±0.15")		rms error 3.13" (3.45±0.16")	
	s_{bbs} = 24 kpc*$(\sigma_{gal}/136$km/s$)^2$		s_{bbs} = 37 kpc*$(\sigma_{gal}/136$km/s)	
Parameter	**Halo One**	**Halo Two**	**Halo One**	**Halo Two**
σ (km/s)	1298 (1293^{+11}_{-10})	603 (595±20)	1285 (1281^{+10}_{-9})	618 (613±17)
r_c (kpc)	77 (76^{+4}_{-3})	75 (72±5)	75 (74^{+3}_{-3})	75 (73±4)
x (arcsec)	-5.4 (-5.5±0.4)	58.6 (57.4±3.2)	-5.4 (-5.3±0.3)	56.5 (55.3±5.0)
y (arcsec)	1.3 (1.2±0.5)	33.8 (33.3±1.1)	1.1 (1.0±0.5)	32.9 (32.6±1.0)
ϵ	0.066 (0.064±0.003)	0.20 (0.19±0.01)	0.067 (0.064±0.003)	0.18 (0.19±0.01)
PA (°)	-33.1 (-32.8±1.9)	12.6 (12.3±1.9)	-32.5 (-32.0±1.8)	13.0 (12.6±1.7)
ENFW	rms error 2.73" (3.12±0.20")		rms error 2.48" (3.08±0.19")	
	s_{bbs} = 21 kpc*$(\sigma_{gal}/136$km/s$)^2$		s_{bbs} = 36 kpc*$(\sigma_{gal}/136$km/s)	
Parameter	**Halo One**	**Halo Two**	**Halo One**	**Halo Two**
C	6.5 (6.3±0.2)	0.5 (0.5±0.1)	6.2 (6.2±0.1)	0.7 (0.7±0.1)
r_{200} (Mpc)	2.04 (2.03±0.03)	2.79 (2.81±0.06)	2.07 (2.06±0.03)	2.52 (2.53±0.06)
x (arcsec)	-2.8 (-4.4±0.15)	34.6 (30.6±3.9)	-3.5 (-4.3±0.10)	36.8 (31.6±1.3)
y (arcsec)	0.8 (0.5±0.9)	31.8 (30.8±4.6)	0.6 (1.3±0.7)	32.1 (31.6±1.8)
ϵ	0.104 (0.104±0.006)	0.19 (0.19±0.01)	0.100 (0.097±0.007)	0.19 (0.19±0.02)
PA (°)	-43.7 (-45.2±1.9)	24.5 (23.8±1.8)	-42.1 (-42.7±1.7)	24.6 (24.4±1.7)
Model free parameters	parameters of the smooth dark matter component		parameters of the smooth dark matter component	
Model constraints	images from this work and Broadhurst et al. (2005a) z_{phot} of sources		images from this work and Broadhurst et al. (2005a) z_{phot} of sources	

Table 3.3: Best fit halo parameters of the smooth dark matter components for Models Ib and IIb. The rms error quoted for each model and halo type is the rms distance between the measured image positions and those predicted by the models expect for image systems where the calculations of an image plane χ^2 was not possible (8, 12, 13, 14, 20 and 30) for which we have used the source plane χ^2 defined in equation 3.7. The values given are for the best fitting halo optimised in the image plane. The values in brackets refer to the mean values obtained from the simulations (optimised in the source plane), the errors in the halo parameters are derived from the spread of the values in the simulations. For details of the models and error derivation see text body.

	Model Ib		**Model IIb**	
NSIE	rms error 3.03" (3.27±0.20")		rms error 2.65" (3.29±0.21")	
	$s_{bbs} = 30$ kpc*$(\sigma_{gal}/136\text{km/s})^2$		$s_{bbs} = 43$ kpc*$(\sigma_{gal}/136\text{km/s})$	
Parameter	**Halo One**	**Halo Two**	**Halo One**	**Halo Two**
σ (km/s)	1223 (1222±13)	647 (645±18)	1210 (1216±11)	658 (660±15)
r_c (kpc)	56 (60±3)	75 (74±3)	58 (60±3)	74 (74±2)
x (arcsec)	-4.7 (-4.9±0.4)	56.7 (49.8±2.1)	-4.9 (-4.7±0.4)	45.5 (48.8±1.8)
y (arcsec)	2.1 (1.1±0.4)	33.1 (31.6±1.1)	1.2 (1.0±0.3)	29.9 (31.0±0.9)
ϵ	0.079 (0.078±0.004)	0.20 (0.19±0.02)	0.078 (0.077±0.004)	0.19 (0.18±0.02)
PA (°)	-33.6 (-35.2±1.5)	16.3 (15.3±2.0)	-34.0 (-34.4±1.5)	15.5 (15.3±1.8)
ENFW	rms error 2.74" (3.30±0.15")		rms error 2.72" (3.31±0.15")	
	$s_{bbs} = 31$ kpc*$(\sigma_{gal}/136\text{km/s})^2$		$s_{bbs} = 51$ kpc*$(\sigma_{gal}/136\text{km/s})$	
Parameter	**Halo One**	**Halo Two**	**Halo One**	**Halo Two**
C	6.4 (6.4±0.2)	1.5 (1.6±0.1)	6.5 (6.4±0.2)	1.6 (1.7±0.1)
r_{200} (Mpc)	2.12 (2.08±0.04)	1.87 (1.86±0.05)	2.08 (2.04±0.04)	1.85 (1.83±0.05)
x (arcsec)	-3.8 (-3.9±0.6)	42.2 (39.0±3.1)	-3.9 (-3.7±0.5)	46.0 (39.1±2.0)
y (arcsec)	0.9 (0.2±0.6)	30.8 (31.0±2.3)	1.1 (-0.2±0.5)	30.7 (30.9±2.0)
ϵ	0.087 (0.088±0.009)	0.21 (0.2±0.01)	0.082 (0.086±0.009)	0.20 (0.18±0.02)
PA (°)	-41.7 (±)	22.4 (21.9±2.9)	-41.1 (-41.1±2.1)	21.9 (21.3±2.7)
Model free parameters	parameters of the smooth dark matter component, z_{phot} of sources		parameters of the smooth dark matter component, z_{phot} of sources	
Model constraints	images from Broadhurst et al. (2005a)		images from Broadhurst et al. (2005a)	
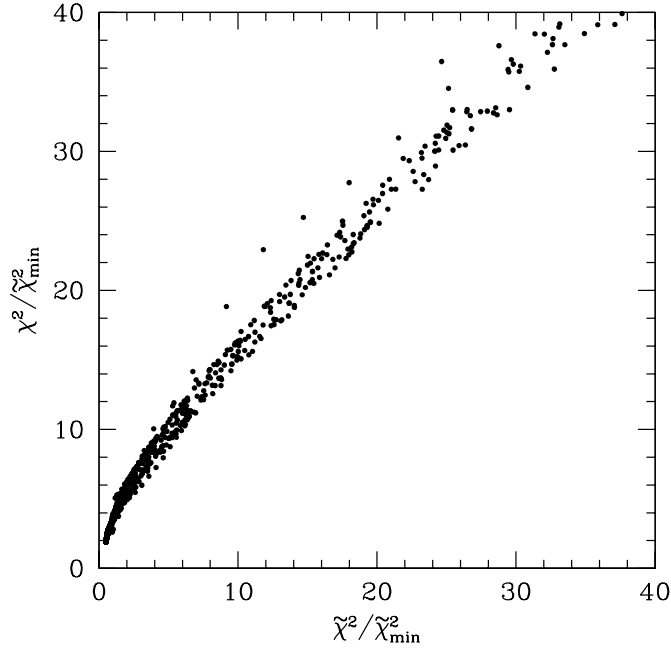
Figure 3.14: A comparison between χ^2 (image plane χ^2) and $\widetilde{\chi}^2$ (source plane χ^2) for ~3000 different model configurations. The important property of $\chi^2(\widetilde{\chi}^2)$ for the minimisation is that it is a monotonically increasing function making $\widetilde{\chi}^2$ a reliable tracer for χ^2 when used in finding optimal model parameters in the error analysis.

shown as a solid grey region, smooth dark matter as a striped grey and the total mass as a solid black region. The regions were determined by taking the best 68.3 per cent of the galaxy component realisations from both Models I and II regardless of the smooth DM profile used. We have decided to combine the individual mass profiles from both models and smooth dark matter profiles since they all provide similar fit qualities and by combining them we allow a greater freedom in the total mass profile.

In Fig. 3.17 we show again the envelope of the total masses encompassed by the best 68.3 per cent fits of all the model galaxies from the error analysis in striped grey. For comparison we also show the strong lensing mass measurement of Broadhurst et al. (2005a) (long dashed), weak lensing mass from King et al. (2002) (NFW dashed, SIS dot dashed) and X-ray mass estimate of Andersson & Madejski (2004) (dashed - long dashed). For Broadhurst et al. (2005a) and Andersson & Madejski (2004) points we plot the 1-σ errors. The Broadhurst et al. (2005a) mass has been integrated from the radial surface mass density profile in their fig. 26, and the errors have been inferred from the errors in surface mass density. Andersson & Madejski (2004)
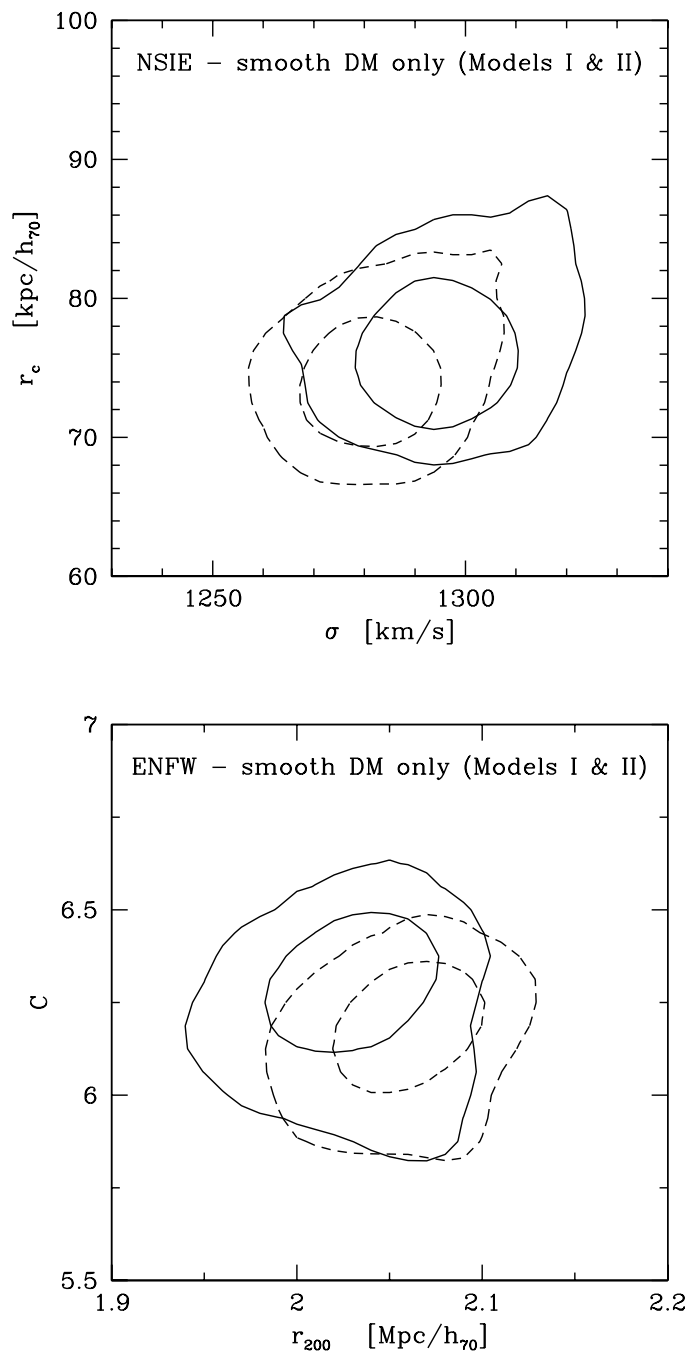
Figure 3.15: Estimates of the profile parameter uncertainties for the main halo of the smooth DM component (NSIE top, NFW bottom). In both panels Model I is represented by the solid contours and Model II by the dashed contours. Contours are drawn at 68 and 95 per cent confidence levels. The uncertainty is mostly due the errors in determining the contribution of the cluster galaxies to the total mass.
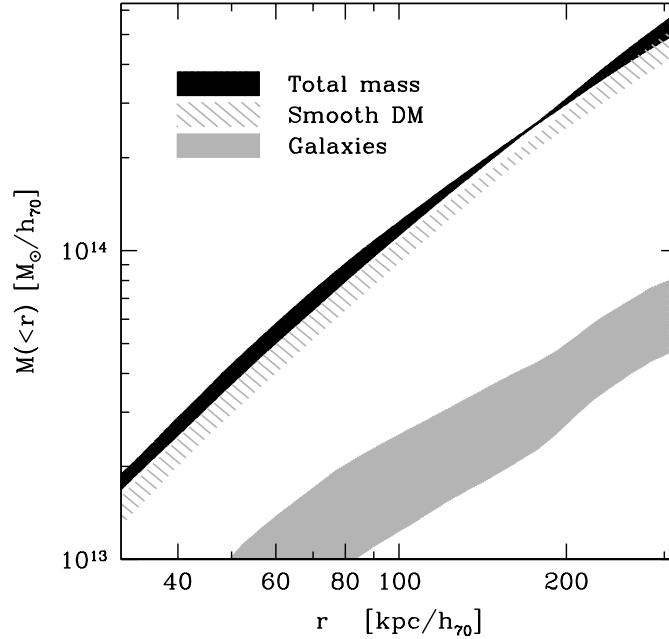
Figure 3.16: 1-σ confidence regions of projected mass M(<r) inside radius r for two mass components and total mass. The mass associated with galaxies is shown as a solid grey, the smooth dark matter as a striped grey and the total mass as a solid black region. The large uncertainty in the galaxy component is well balanced by the smooth dark matter component to produce a tight M(<r) profile for the total mass.

have also provided an estimate of the projected X-ray mass so that the profile can be compared with lensing mass measurements. The agreement between our work and that of Broadhurst et al. (2005a) is very good, well within 1-σ at all radii. The mass measured using strong lensing is factor ~2 larger than the mass from X-ray estimates. For a discussion on the low mass from X-ray estimates, please refer to Andersson & Madejski (2004).

To estimate the NSIS and NFW parameters of the total mass we can simply fit the mass profile obtained with Models I and II with a single NSIS or NFW halo. One should not forget that the total mass profile was derived using the NSIE and NFW profiles themselves. The total mass profile is composed of the mass in the galaxies and two elliptical smooth DM haloes and hence the total mass is no longer a pure NSIE or ENFW profile. In fitting a single halo we also do not include ellipticity. The excellent agreement between the total mass profile obtained in this work and that of Broadhurst
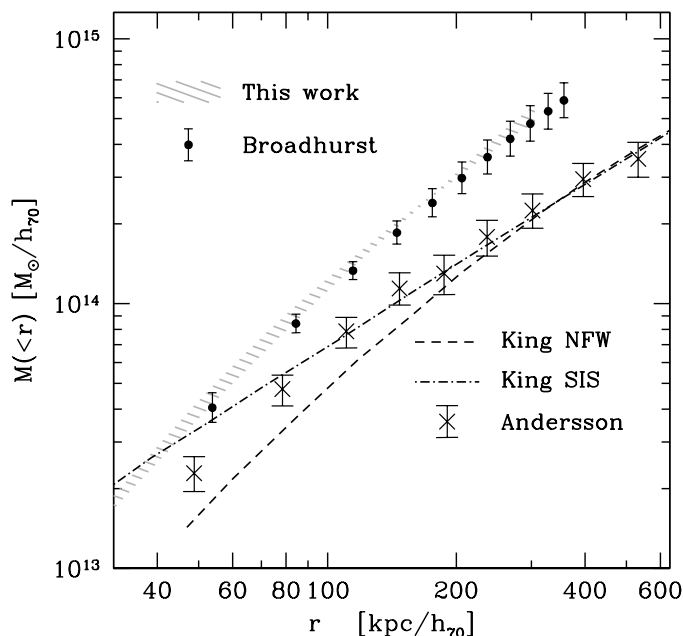
Figure 3.17: 1-σ confidence region of projected mass M(<r) inside radius r from this work (striped grey region) compared with Broadhurst et al. (2005a) (long dashed), King et al. (2002) (NFW dashed, SIS dot dashed) and Andersson & Madejski (2004) (dashed - long dashed). The error bars shown for Broadhurst et al. (2005a) and Andersson & Madejski (2004) are 1-σ errors. The mass profile and errors for Broadhurst et al. (2005a) were obtained by integration from the surface mass density in their fig. 26.

et al. (2005a) and the superior performance of our models to theirs give us confidence that the parameters we have derived are indeed representative of the total mass profile of the cluster. We do not compare the quality of fit of NSIS and NFW haloes but instead the obtained parameters with those from weak lensing. This should help us to avoid problems arising from the underlying smooth DM profiles used in obtaining the total mass profile.

The 68.3, 95.4 and 99.7 per cent confidence contours for the NFW parameters are shown in Fig. 3.18 (solid black contours). Both the concentration and r_{200} are well constrained. The best fit values are $C=6.0\pm0.5$ and $r_{200}=2.82^{+0.11}_{-0.09}$.

Also the NSIS parameters are well constrained. The corresponding confidence contours are shown in Fig. 3.19. Both of the NSIS parameters depend on the halo profile in the region where the multiple images have significant constraints. Therefore the confi-

dence contours are also extremely tight. The best fit parameters are $\sigma=1514^{+18}_{-17}$ km/s and $r_c=71\pm5$ kpc. The best fitting profile parameters are summarised in Table 3.4.

As a comparison we have also fitted an NSIS and an NFW profile to the *smooth* DM component only. This results in an NSIS a velocity dispersion of 1450^{+39}_{-31} km/s and a core radius of 77^{+10}_{-8} kpc/h while an NFW profile has a concentration of $4.7^{+0.6}_{-0.5}$ and a virial radius of 2.86 ± 0.16 Mpc/h_{70}.

Table 3.4: Best fit halo parameters for the cluster profile. For Models III and IV we have fitted the measured cluster parameters with a single NSIS or NFW profile. The constraints for the cluster parameters were mass for Model III,both mass and shear for Model IV. For details of the models see text body.

	Model III	**Model IV**
NSIE	χ^2 / d.o.f. = 10.5 / 11	χ^2 / d.o.f. = 30.0 / 20
Parameter	**only one halo fitted**	**only one halo fitted**
σ	1514^{+18}_{-17} km/s	1499^{+15}_{-14} km/s
r_c	71 ± 5 kpc	66 ± 5 kpc
ENFW	χ^2 / d.o.f. = 0.8 / 11	χ^2 / d.o.f. = 31.9 / 20
Parameter	**only one halo fitted**	**only one halo fitted**
C	$6.0\pm.5$	$7.6^{+0.3}_{-0.5}$
r_{200}	$2.82^{+0.11}_{-0.09}$ Mpc	$2.55^{+0.07}_{-0.04}$ Mpc
Model free parameters	the above parameters of the halo profiles	the above parameters of the halo profiles
Model constraints	total mass obtained with Models I and II	total mass obtained with Models I and II shear from Broadhurst et al. 2005b

3.5.5   Model IV: Combining Information from Strong and Weak Lensing

In this subsection we include the new weak lensing shear data from Broadhurst et al. (2005b) in our analysis to use information of the cluster profile from larger cluster-centric radii.

Strong lensing in A1689 can only constrain the mass at best to out 200-300 kpc from the cluster centre. In order to constrain the scale radius of an NFW profile strongly it should lay within the multiple images. Unfortunately, in the case of A1689, the scale radius seems to be just outside the multiple images (and hence strong lensing cannot constrain it significantly) but too small to be well constrained by weak lensing data alone. On the other hand weak lensing can tell us something about the total mass of

the cluster and hence constrain r_{200}. By combining this with information from strong lensing (details of the profile at small radii) one should expect to have a handle on the cluster at all radii.

In their extensive work on this cluster Broadhurst et al. (2005a,b) conclude that the parameters derived from strong and weak lensing are not compatible. In the strong lensing regime an NFW halo has only a moderate concentration ($C=6.0\pm0.5$ in this work, Broadhurst et al. (2005a) find $C=6.5^{+1.9}_{-1.6}$) whereas in the weak lensing regime a very high concentration ($C=13.7^{+1.4}_{-1.1}$, Broadhurst et al., 2005b) is required, uncharacteristic to a halo of this size and typical to a halo with a much lower mass.

We have checked this inconsistency in the NFW parameters by fitting a single halo to both the radial mass profile (Model III, this work) and shear profile (Broadhurst et al. (2005b)), shown in Figures 3.20 and 3.21. The fit is done simultaneously to the mass points from strong lensing shown in Fig. 3.20 and reduced shear points from weak lensing shown in Fig. 3.21. In the fitting all the points are given equal weighting and the χ^2 of a given halo is calculated from how it's mass fits the mass at $r \lesssim 2$' and the shear at $r \gtrsim 2$'. The best fitting NFW profile is plotted as a dashed black line in the two figures.

Unlike Broadhurst et al. (2005b) we do not include any prior ($C\leq30$) on the concentration in our fits since there is no obvious bias towards NFW profiles with higher concentrations: a high quality fit with a large concentration purely reflects the inability of shear measurements to constrain the central cluster profile. A prior could lead to a wrong determination of the minimum χ^2 and hence favour a smaller concentration without a physical significance.

Fitting a single NFW halo to the weak lensing shear from Broadhurst et al. (2005b) gives only a lower limit for the concentration but constrains r_{200} (or equivalently M_{200}) to ~ 2.0-2.5Mpc/h_{70} (68.3, 95.4 and 99.7 per cent confidence regions for C–r_s are shown in Fig. 3.18 as dotted lines). The best fit values are $C=30.4$ and $r_{200}=1.98$ Mpc/h_{70}. The fit is excellent with $\chi^2_{WLshear}/d.o.f. = 2.5 / 8$ (where d.o.f. is for degrees of freedom). The parameters of the NFW profile from fitting the total mass and shear independently disagree more than the estimated 3-σ errors. The difference between the NFW parameters obtained in this work and that of Broadhurst et al. (2005b) is unlikely to arise from the prior as Broadhurst et al. (2005b) have a flat prior for c<30. Broadhurst et al. (2005b) however do not fit an NFW profile to the shear measurements only. Instead they fit the the NFW profile to the surface mass density map obtained from the shear. In our work we fit the shear directly, avoiding the extra step involved.

By fitting both shear and mass simultaneously, we are able to combine the constraints from both small and large radii to obtain well defined NFW parameters for the halo. The NFW parameters in this case become $C=7.6^{+0.3}_{-0.5}$ and $r_{200}=2.55^{+0.07}_{-0.09}$ Mpc/h_{70} (confidence regions for the combined weak and strong lensing fit are shown with solid
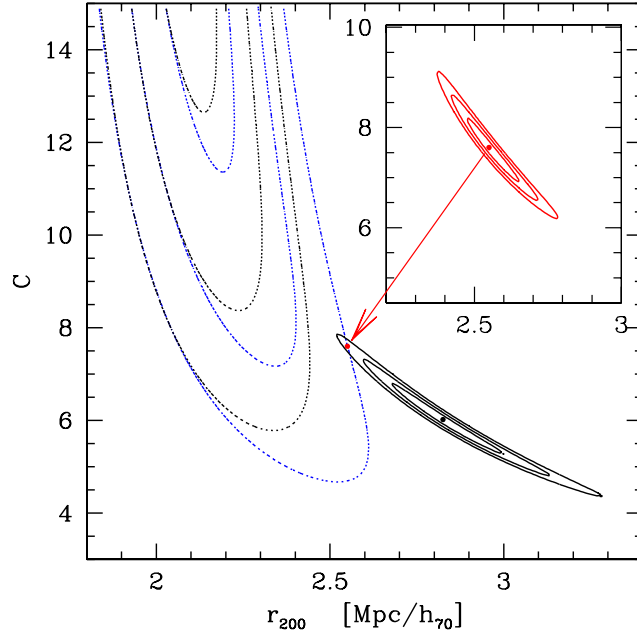
Figure 3.18: 68.3, 95.4 and 99.7 per cent confidence contours for the NFW parameters C–r_{200} for a fit to reduced shear (data from Broadhurst et al. (2005b)) only (dotted contours) and mass (data from this work) only (solid black contours). The dotted blue contours show the confidence regions from shear when the last two data points are excluded. The combined fit to both reduced shear and mass simultaneously is $\chi^2/d.o.f. \sim 31.9 / 20$ (shown in the inlet for clarity with the same scale). The best fitting parameters are $C=7.6^{+0.3}_{-0.5}$ and $r_{200}=2.55^{+0.07}_{-0.09}$ Mpc/h_{70}. A fit to shear only gives $C=30.4$ and $r_{200}=1.98$ Mpc/h_{70}.

red contours in Fig. 3.18). The mass and shear profiles of the best fitting NFW halo are shown in Figures 3.20 and 3.21 respectively as dashed lines.

We have repeated the experiment also for an NSIS halo. The corresponding contours are shown in Fig. 3.19, and mass and shear profiles in Figures 3.20 and 3.21 as solid lines.

Like with the NFW halo the core radius of the NSIS halo is poorly constrained by the weak lensing data alone though surprisingly a singular profile with $\sigma=1354$ km/s has the best fit. The fit is good with χ^2 / d.o.f. = 10 / 8. The best fitting parameters to both weak and strong lensing simultaneously are $\sigma=1499\pm15$ km/s and $r_c=66\pm5$ kpc/h_{70} with χ^2 / d.o.f. = 30 / 20. The agreement between the parameters for the NSIS halo is better than for the NFW profile, though still only at 2-σ level.
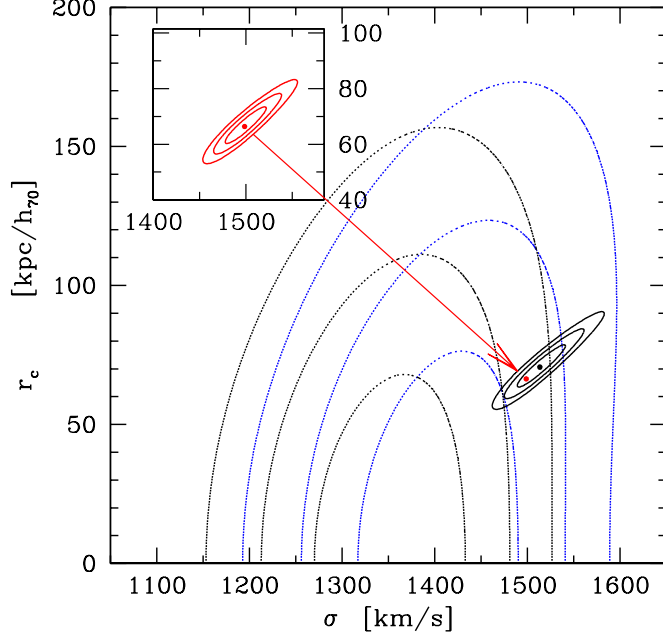
Figure 3.19: 68.3, 95.4 and 99.7 per cent confidence contours for the NSIS parameters σ–r_c for a fit to reduced shear (data from Broadhurst et al. (2005b)) only (dotted contours) and mass (data from this work) only (solid black contours). The dotted blue contours show the confidence regions from shear when the last two data points are excluded. The combined fit to both reduced shear and mass simultaneously (shown in the inlet with the same scale) is similar to that of NFW profile with $\chi^2/d.o.f. \sim 30/27$. The best fitting parameters are σ=1499±15 km/s and r_c=66±5 kpc/h_{70}. A fit to shear only gives a singular profile with σ=1354 km/s.

To see how important the last two shear data points are for the previously derived cluster parameters we have excluded the two outer most data points from the shear measurement. If compared to numerical simulations the concentration of the NFW halo remains unreasonably high although the disagreement between weak and strong lensing is reduced to just under 3-σ. For the NSIS halo the shear data is still fit best with a singular profile but higher values of core radius are allowed and the velocity dispersion is increased to make the weak and strong lensing parameters agree at better than 2-σ. The best fitting parameters are C=7.1±0.4 and r_{200}=2.63±0.06 Mpc/h_{70} for the NFW halo and σ=1505±15 km/s and r_c=68±5 kpc/h_{70} for the NSIS halo. The two profiles fit well with $\chi^2_{nsis}/d.o.f. \sim 22/18$ compared to $\chi^2_{nfw}/d.o.f. \sim 20/18$. The confidence regions with the last two shear points excluded are shown as dotted blue
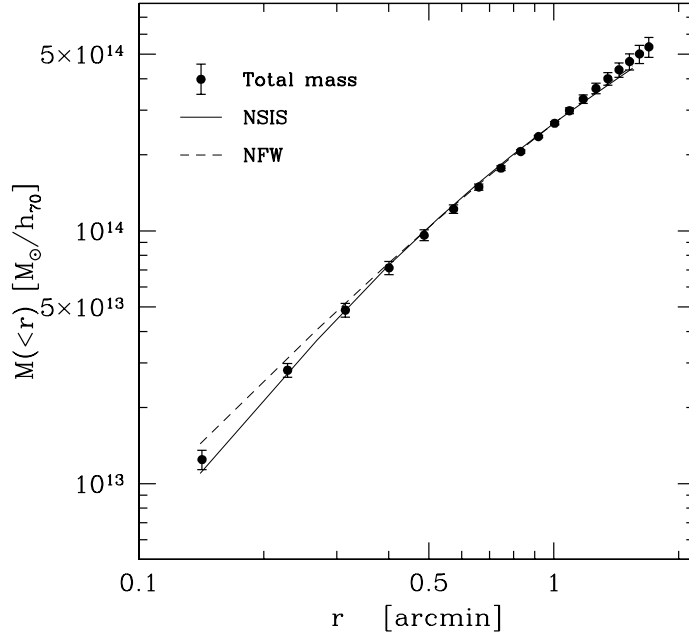
Figure 3.20: Radial profile of the total mass from this work (circles). The lines show the best fitting NSIS (solid line) and NFW (dashed line) profiles to a simultaneous fit of the shear in Fig. 3.21 and the mass in this Figure.

contours in Figures 3.18 and 3.19.

In a recent work Biviano & Salucci (2005) derived the mass profiles of the different luminous and dark components of cluster masses separately. They find that ratio of baryonic to total mass decreases from the centre to $r \sim 0.15$ virial radii and then increases again. We see the same trend also in our work (Fig. 3.16), where the galaxy component has a minimum contribution at around 200 kpc. This is smaller than expected (380 kpc) if we take the r_{200} of the NFW profile to be the virial radius of the cluster.

The best fit parameters are summarised in Table 3.4.

3.5.6   Comparison with Literature

The mass of Abell 1689 has been determined in a variety of ways with different weaknesses and strengths. Results from the three methods used (X-ray temperature, line-of-sight velocity and lensing (both weak and strong)) have disagreed considerably. This section makes a short summary and comparison of the results using the different meth-
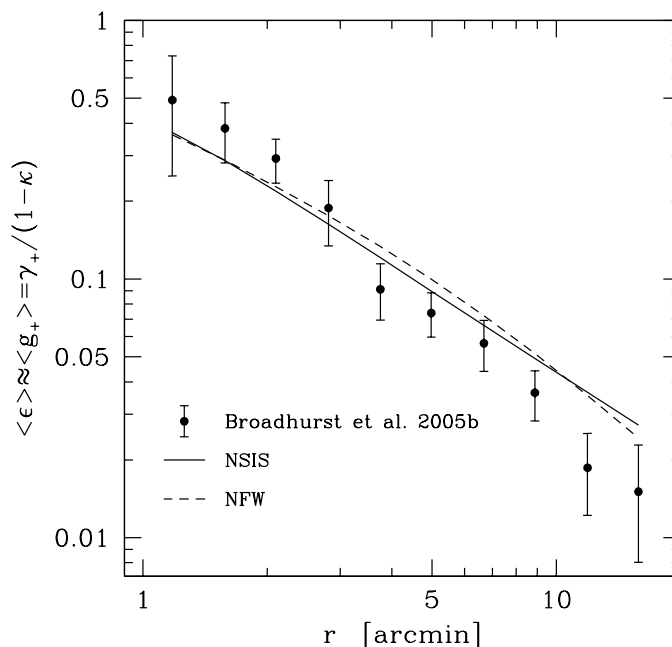
Figure 3.21: Radial profile of the tangential shear from Broadhurst et al. (2005b) (circles). The lines show the best fitting NSIS (solid line) and NFW (dashed line) profiles to a simultaneous fit of the shear in this figure and the mass in Fig. 3.20.

ods.

Recent results are summarised in Tables 3.5 and 3.6. Aperture mass fits are summarised in Table 3.5 and parametric model fits in Table 3.6. When comparing different mass estimates one should bear in mind that both X-ray and velocity dispersion measure a spherical mass where as lensing in the thin lens approximation measures projected mass, i.e. mass in a cylinder of a given radius, resulting in higher masses within a given radius. Only lensing measures the mass directly. Both X-ray and velocity dispersion rely on the cluster being a relaxed system.

3.5.6.1 X-ray

The most recent X-ray measurements of the mass of A1689 are those of Xue & Wu (2002) with the Chandra X-Ray Observatory and Andersson & Madejski (2004) with the XMM-Newton X-Ray Observatory. Both find nearly circular X-ray emission centred on the cD galaxy. Best fit NFW profile to Andersson & Madejski (2004) data has

Table 3.5: Comparison between mass estimates for Abell 1689 from different methods. The mass measured by Andersson & Madejski (2004) are underestimates of the total mass if the cluster is undergoing a merger. For our work the mass at $r=0.25$ Mpc/h_{70} is an extrapolation since the multiple images do not extend to such large clustercentric radii. All the masses given in this table are projected masses. This includes the Andersson & Madejski (2004) X-ray mass estimate taken from their paper.

$M(<r)$ $(10^{15}$ M$_\odot$ h$_{100}^{-1})$	r (Mpc h$_{100}^{-1}$)	Reference
0.14 ± 0.01	0.10	this work, Model III
0.082 ± 0.013	0.10	Andersson & Madejski (2004)
0.43 ± 0.02	0.24	Tyson & Fischer (1995)
0.20 ± 0.03	0.25	Andersson & Madejski (2004)
0.37 ± 0.06	0.25	this work, Model III
0.48 ± 0.16	0.25	Dye et al. (2001)

parameters $C = 7.7^{+1.7}_{-2.6}$ and $r_{200} = 1.87 \pm 0.36$ Mpc/h_{70}. They have also fitted a SIS profile to the data and obtain $\sigma = 918$ km/s. The NFW profile gives a much better fit to their data. We have also fitted an NSIS profile to Andersson & Madejski (2004) since it is clear that (single parameter) a SIS will not be able to reproduce the data. We have fitted the spherical mass of an NSIS profile with $\sigma = 1190$ km/s and $r_c = 27$ kpc to the data from fig. 9 of Andersson & Madejski (2004) and this provides a very good fit. The NSIS halo along with the fitted points are shown in Fig. 3.22. The low σ found by Andersson & Madejski (2004) is mainly driven by the low central mass of the cluster which the SIS profile can only accommodate with a low σ. By including a core radius in the fit the mass can be modelled very well everywhere also by an IS profile.

The total mass inside 140kpc from the cluster centre is 1.2×10^{14} M$_\odot$ and 1.9×10^{14} M$_\odot$ for Andersson & Madejski (2004) and Xue & Wu (2002) respectively. Andersson & Madejski (2004) also discuss the effect a merger would have on the X-ray mass estimates. The estimated X-ray masses could increase by a factor of ~2 (velocity dispersion by factor $\sqrt{2}$) assuming that two equal mass haloes are considered as one in the X-ray analysis. This would be enough to bring X-ray mass of Abell 1689 in good agreement with lensing.

3.5.6.2 Spectroscopy

An early spectroscopic work by Teague et al. (1990) found a very high velocity dispersion of 2355km/s for Abell 1689. Girardi et al. (1997) have reanalysed the data from Teague et al. (1990) and found four different structures in A1689 with velocity dispersions of 1429km/s, 321km/s, 243km/s and 390km/s. A simple consideration
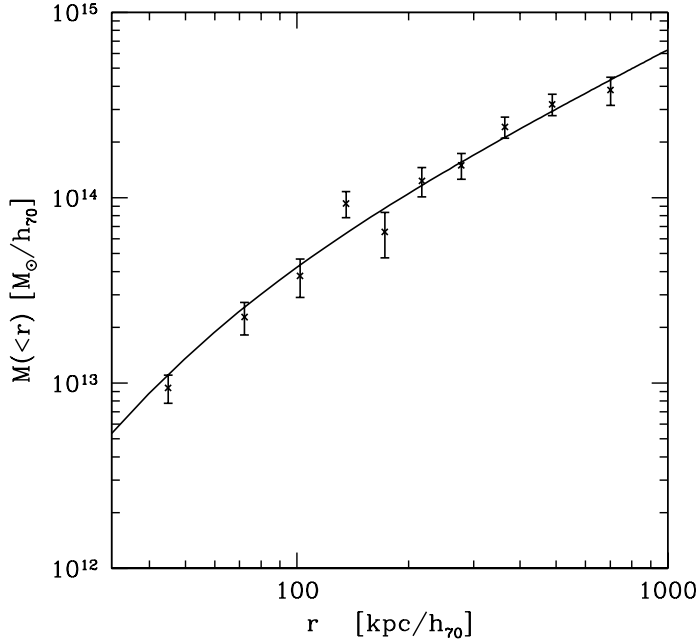
Figure 3.22: The spherical mass of A1689 from X-ray observations of the cluster by Andersson & Madejski (2004) (points) and our best fit NSIS halo to the points with σ=1190 km/s and r_c =27 kpc (line). The fit is very good with χ^2 / d.o.f. = 9.2 / 8. The low mass in the centre can only be fitted with an isothermal sphere if a core radius is included.

of total mass in the separate structures equals that of a single isothermal sphere with σ~1550km/s. The separate structures are more extended than the region of multiple images and the 2nd halo in this study does not correspond to any of the spectroscopically identified groups by Girardi et al. (1997).

Czoske (2004) have used VIsible MultiObject Spectrograph (VIMOS) on the Very Large Telescope (VLT) to obtain spectra for A1689. Their results are still preliminary but indicate a strong gradient in the velocity dispersion from ~2100km/s in the centre to ~1200km/s at larger clustercentric distances ($\gtrsim$1Mpc). The high velocity dispersion on the centre could be due to an unrelaxed system and not an indication of a high total mass of the cluster.

Lokas et al. (2005) have recently used published spectroscopic redshifts mainly from Teague et al. (1990), Balogh et al. (2002) and Duc et al. (2002) to show that cluster mass cannot be reliably estimated from galaxy kinematics due to the complex kinematical structure of A1689. The obtained velocity dispersion depends sensitively

on the chosen galaxy sample.

3.5.6.3   Weak Lensing

The mass of A1689 has been measured in a number of cases with weak gravitational lensing. The obtained masses are always considerably lower when compared to strong lensing masses or line-of-sight velocity dispersion (LOSVD) measurements with σ=1028 km/s, σ=998 km/s, σ=1030 km/s and σ=998 km/s (Clowe & Schneider (2001), King et al. (2002a,b) and Bardeau et al. (2005) respectively). Clowe & Schneider (2001); King et al. (2002) use the same catalogue of lensed background galaxies. The catalogue is very likely contaminated by unlensed galaxies in the foreground and only weakly lensed galaxies in the close proximity of the cluster (z <0.3) where lensing is inefficient. These galaxies reduce the average shear signal leading to lower mass estimates. The SIS velocity dispersion estimate of Clowe & Schneider (2001) increases to 1095 km/s if they assume that 87 per cent of the faint background galaxies have z >0.3. In Clowe (2003) colour information from Canada–France–Hawaii Telescope (CFHT) is added to better select background sources. They find that without the colour information the mass in the cluster core is underestimated due to cluster dwarf galaxies. The new values for A1689 become σ=1205 km/s for the SIS profile and C = 7.9 and r_{200}=2.04 Mpc. Bardeau et al. (2005) agree very well with Clowe & Schneider (2001); King et al. (2002) both for the SIS parameters and the M_{200} of an NFW profile although they find a low concentration of 3.5. Recent work by Broadhurst et al. (2005b) results in higher masses and only 1-2 σ discrepancy between weak and (our) strong lensing models.

Hoekstra (2001, 2003) investigate the effect of distant (along line-of-sight) large scale structure (LSS) on the errors of derived on SIS velocity despersion (Hoekstra, 2001) and M_{200} and concentration of an NFW halo (Hoekstra, 2003). They conclude that the errors could be underestimated by a factor ~2. The effect is more noticeable at large clustercentric radii where the signal from the cluster itself is small. The more massive the cluster the better the concentration can be constrained. Also M_{200} can be derived with greater relative accuracy although the absolute error is increased. In Hoekstra (2001) they showed that the LSS increases the noise but does not bias the results. We expect the effect to be smaller in the strong lensing regime where the signal is completely dominated by the cluster mass.

3.6   Conclusion

We have identified 15 images systems in deep ACS images of galaxy cluster Abell 1689. Two of these are not in the 30 image systems identified by Broadhurst et al. (2005a). By excluding one of their image systems and splitting another in two we

have constructed a new catalogue with 107 multiple images. These from 31 image systems and we have additionally used one long arc in the modelling. The galaxy cluster was modelled with a two component mass model: mass associated with cluster galaxies and an underlying smooth dark matter component. Cluster galaxies were identified from the cluster redsequence and their halo masses were estimated using Fundamental-Plane and Faber-Jackson relations. The use of Fundamental-Plane in measuring the mass for most of the galaxies used in the cluster modelling is new and allows a very precise determination of the (central) galaxy mass. The galaxies were modelled with a truncated isothermal ellipsoid. The truncation of the galaxy haloes is necessary for accurate lensing models. The smooth dark matter component was modelled separately with two parametric elliptical halo profiles: elliptical NFW profile and a non-singular isothermal ellipsoid.

We find that both an ENFW and NSIE describe the smooth dark matter component very well. The best fit ENFW profile of the smooth dark matter component has a virial radius of 2.06±0.03 Mpc and a concentration parameter of 6.2±0.1, the best fitting NSIE profile has a core radius of 74±3 kpc and a velocity dispersion of 1281±10 km/s. The ellipticities of the two model haloes are small ($\epsilon = 0.06$ in both cases). The multiple images are reproduced very well. With the modified set of multiple images the best fitting model has an rms ~0.8" better than Broadhurst et al. (2005a).

By fitting a single NSIS and NFW halo to the total mass we can constrain the halo parameters of the cluster as a whole very strongly. The NFW parameters are C=6.0±0.5 and r_{200}=2.82±0.11 Mpc; the NSIS parameters are σ=1514$^{+18}_{-17}$ km/s and r_c=71±5 kpc.

Using the images of Broadhurst et al. (2005a) we obtain a fit with an rms distance between the identified multiple images and model predictions 0.6" better than the best model in Broadhurst et al. (2005a) (rms of 2.65" compared to 3.25"). This is surprising considering the large freedom in the mass model used by Broadhurst et al. (2005a) compared to parametric models. The superior performance of our model can in part be attributed to a careful analysis of the cluster galaxy component. It also indicates that small scale dark matter 'mini' haloes are not needed to explain the deflection field in A1689. The overall mass profiles are in good agreement however. This shows that strong gravitational lensing can be used to derive very accurate total mass profiles; different methods and assumptions agree very well in mass although the treatment of the cluster galaxies in particular can be quite different.

The low masses obtained from weak lensing in the past are no longer observed in new shear measurements by Broadhurst et al. (2005b). According to our analysis, at least for the NFW profile, the parameters obtained from strong and weak lensing disagree at ~3-σ level. The high concentration of an NFW profile fit to weak lensing data is incompatible with both the strong lensing results presented here and in

Broadhurst et al. (2005a). The discrepancy between halo parameters obtained with weak and strong lensing separately is present at <2-σ level in the case of an isothermal sphere dark matter halo. We do not find support for the strong rejection of a softened isothermal sphere by Broadhurst et al. (2005b) based on the combined strong and weak lensing mass profile.

The unusually high concentration of 13.7 found in Broadhurst et al. (2005b) (compared to 4 expected from numerical N-body simulations) can be explained by a suitably aligned tri-axial halo (Oguri et al., 2005). This cannot be used to solve the discrepancy between weak and strong lensing measurements which both measure the same projected mass, albeit at different radii.

Acknowledgements

Table 3.6: Comparison between best fit parametric mass models from different methods for Abell 1689. Andersson & Madejski (2004) is an X-ray, King et al. (2002); Bardeau et al. (2005) a weak lensing and Girardi et al. (1997) a line of sight velocity study of the cluster. The background galaxy catalogue used by King et al. (2002) suffers from contamination from galaxies at low redshifts where lensing is inefficient (discussed in more detail in Clowe & Schneider (2001)) which reduces the total measured mass of the cluster and hence the measured velocity dispersion.

NFW Parameters

Method	C	r_{200} (Mpc)	Reference
SL	6.0±0.5	2.82±0.11	this work
SL	$6.5^{+1.9}_{-1.6}$	2.02	Broadhurst et al. 2005a
SL	$5.70^{+0.34}_{-0.5}$	$4.14^{+0.48}_{-0.42}$	Zekser et al. 2006
X-ray	$7.7^{+1.7}_{-2.6}$	1.87±0.36	Andersson & Madejski 2004
WL	4.8	1.84	King et al. 2002
WL	$3.5^{+0.5}_{-0.3}$	1.99±0.25	Bardeau et al. 2005
WL	7.9	2.04	Clowe 2003

NSIE Parameters

Method	σ (km/s)	r_c (kpc)	Reference
SL	1514±18	71±5	this work
SL	1390	60	Broadhurst et al. 2005a
X-ray	918±27	SIS	Andersson & Madejski 2004
X-ray	1190	27	Andersson & Madejski 2004*
WL	998^{+33}_{-42}	SIS	King et al. 2002
WL	998±68	SIS	Bardeau et al. 2005
WL	1205	SIS	Clowe 2003
LOSVD	1429^{+145}_{-96}	-	Girardi et al. 1997

* data from Andersson & Madejski 2004, fitting done in this work.

3.7 Appendix

3.7.1 Gravitational Lensing by NSIE, NFW and BBS profiles

3.7.1.1 Isothermal Sphere / Ellipsoid

A model often used in gravitational lensing for galaxies and clusters of galaxies is a singular isothermal sphere (SIS) (e.g. Gott & Gunn, 1974; Turner et al., 1984). SIS naturally reproduces the observed flat rotation curves of galaxies (e.g. Roberts & Rots, 1973). The following equations describe a non-singular (or softened) isothermal ellipsoid (Hinshaw & Krauss, 1987) where the singularity has been removed with a core radius, and additionally an ellipticity has been incorporated to better model the observed galaxy shapes (Seitz et al., 1998). In the equations ellipticity is introduced to the gravitational potential, in a similar fashion to Kochanek et al. (1989), and not the mass distribution. This approach has some problems with large ellipticities, when the accompanying mass distribution can have negative values, as noted by Blandford & Kochanek (1987), Kormann et al. (1994) and others, but is numerically rather simple and straightforward to implement since all parameters of interest can be calculated from the analytic derivatives of the potential. An alternative approach is to have an elliptical mass distribution as demonstrated by Kormann et al. (1994) but the expressions for deflection angle (α), surface mass density (κ) and shear (γ) are considerably more complicated. Kassiola & Kovner (1993) have done a thorough comparison between elliptical potentials and elliptical mass distributions. We have estimated the effect of an elliptical potential on the ellipticity of the surface mass density, illustrated in Fig. 3.6. This will be discussed later in more detail.

In the following equations ψ is gravitational potential, $\boldsymbol{\theta}$ is (image) position on the lens plane, ζ is a core radius, q=b/a=$(1-\epsilon)/(1+\epsilon)$ is the axis ratio of the potential and θ_E is the Einstein radius of a singular isothermal sphere.

The equations for the deflection potential ($\psi(\boldsymbol{\theta})$), the deflection angle (α), κ and $\boldsymbol{\gamma}$ are

$$\psi(\boldsymbol{\theta}) = \frac{\psi_0}{\zeta} \sqrt{\zeta^2 + q\,\theta_1^2 + \frac{1}{q}\,\theta_2^2} = \theta_E\,C(\boldsymbol{\theta})\,, \tag{3.8}$$

with $\theta_E = \frac{\psi_0}{\zeta} = 4\pi \frac{D_{ds}}{D_s}(\frac{\sigma}{c})^2$ and $C(\boldsymbol{\theta}) = \sqrt{\zeta^2 + q\,\theta_1^2 + \frac{1}{q}\,\theta_2^2}$,

$$\boldsymbol{\alpha}(\boldsymbol{\theta}) = \nabla\psi(\boldsymbol{\theta}) = \frac{\theta_E}{C(\boldsymbol{\theta})} \cdot \left(q\,\theta_1,\ \frac{1}{q}\,\theta_2\right), \tag{3.9}$$

$$\kappa(\boldsymbol{\theta}) = \frac{1}{2}\nabla^2\psi(\boldsymbol{\theta}) = \frac{1}{2}\,\frac{\theta_E}{C(\boldsymbol{\theta})^3}\left(Q_+\,\zeta^2 + \theta_1^2 + \theta_2^2\right), \tag{3.10}$$

with $Q_\pm = q \pm \frac{1}{q}$,

$$\gamma_1(\boldsymbol{\theta}) = \frac{1}{2} \frac{\theta_E}{C(\boldsymbol{\theta})^3} \left(Q_- \, \zeta^2 - \theta_1^2 + \theta_2^2 \right), \tag{3.11}$$

$$\gamma_2(\boldsymbol{\theta}) = -\frac{\theta_E \, \theta_1 \, \theta_2}{C(\boldsymbol{\theta})^3} \, , \tag{3.12}$$

3.7.1.2   Universal Dark Matter Profile

The universal dark matter profile is an analytic fit to results of numerical N-body simulations of galactic haloes by Navarro et al. (1996). These simulations showed that density profiles of galactic haloes of very different sizes (two decades in radius) could be fitted with a single 'universal' profile. At small radii ($r < r_s$ or $x = r/r_s < 1$) the NFW-profile is flatter than isothermal with, $\rho \propto r^{-1}$, where as for large radii ($x > 1$), where $\rho \propto r^{-3}$, it is steeper than isothermal which has $\rho \propto r^{-2}$ everywhere.

Lensing by NFW-profile has been studied in a number of papers (e.g. Bartelmann, 1996; Wright & Brainerd, 2000; Golse & Kneib, 2002). We have implemented an elliptical NFW-profile (ENFW) following the formalism described in Golse & Kneib (2002). They have introduced the ellipticity to the deflection angle rather than the potential (or mass distribution). The treatment in Golse & Kneib (2002) is very general explaining also how to obtain analytic values for κ and γ for the NFW profile as well as other profiles.

For the ellipticity parameters $a_{1\epsilon}$ and $a_{2\epsilon}$ in Golse & Kneib (2002) we have followed the example of Meneghetti et al. (2003) so that $a_{1\epsilon}=1-\epsilon=a/b=q$ and $a_{2\epsilon}=1/(1-\epsilon)=b/a=1/q$.

The deflection angle for a spherical NFW mass distribution at $x = r/r_s$ is

$$\alpha^{NFW}(x) = \frac{4\kappa_s}{x} g(x), \tag{3.13}$$

with

$$g(x) = \ln \frac{x}{2} + \begin{cases} \frac{2}{\sqrt{1-x^2}} \text{arctanh} \sqrt{\frac{1-x}{1+x}} & , x < 1 \\ 1 & , x = 1 \\ \frac{2}{\sqrt{x^2-1}} \text{arctan} \sqrt{\frac{x-1}{x+1}} & , x > 1 \end{cases} \tag{3.14}$$

We approximate an elliptical mass distribution with axis ratio q by elliptical contours of the deflection angle,

$$x \rightarrow \chi = \sqrt{q x_1^2 + \frac{1}{q} x_2^2}, \tag{3.15}$$

$$\alpha_1^{ENFW} = \alpha^{NFW}(\chi) \frac{q\, x_1}{\chi}, \quad \alpha_2^{ENFW} = \alpha^{NFW}(\chi) \frac{x_2}{q\, \chi} \tag{3.16}$$

The surface mass density (κ) and shear ($\boldsymbol{\gamma}$) are calculated from the elliptical deflection angles by numerical differentiation. For analytic expressions please refer to Golse & Kneib (2002).

3.7.1.3 Truncated isothermal sphere

The truncated isothermal sphere has been introduced by Brainerd et al. (1996) in the framework of galaxy-galaxy lensing. The two parameters of BBS profile are truncation radius (s) and central velocity dispersion (σ). The density profile of the BBS model is then given by

$$\rho(r) = \frac{\sigma^2}{2\pi G r^2} \frac{s^2}{(r^2 + s^2)} \tag{3.17}$$

For $r < s$ the density profile is similar to a singular isothermal sphere ($\rho(r) \propto 1/r^2$) where as for $r > s$ the density falls off quicker ($\rho(r) \propto 1/r^4$) to avoid the infinite mass of an isothermal sphere.

The deflection angle of a BBS profile is

$$\alpha^{BBS}(x) = \frac{4\pi\sigma^2 D_{ds}}{D_s c^2 x} \left[1 + x - \sqrt{1 - x^2} \right] \tag{3.18}$$

with $x = r/s$.

The ellipticity is included in the deflection angle in exactly the same way as was done for the ENFW halo. The surface mass density and shear were also calculated from elliptical deflection angles by numerical differentiation.

3.7.2   Fundamental Plane

Table 3.7: Table of galaxy properties from fitting cluster galaxies with a Sersic profile and using the Fundamental Plane. The parameters of the 80 most massive galaxies are tabulated.

ID	RA	Dec	m_{AB}[1]	n_{ser}	R_e[2] (kpc)	$1-b/a$	PA (°)	σ_{est}[3] (km/s)
1	+13:11:25.53	-1:20:37.09	17.13 ± 0.15	3.1 ± 0.3	8.1 ± 0.5	0.37 ± 0.02	10 ± 1	178 (224/141)
2	+13:11:25.28	-1:19:31.12	19.09 ± 0.10	6.0 ± 0.1	2.2 ± 0.1	0.06 ± 0.01	70 ± 3	108 (136/86)
3	+13:11:28.19	-1:18:43.80	18.75 ± 0.14	2.6 ± 0.1	2.5 ± 0.1	0.57 ± 0.03	32 ± 1	115 (144/91)
4	+13:11:26.09	-1:19:51.99	18.39 ± 0.13	3.9 ± 0.2	2.5 ± 0.1	0.23 ± 0.01	79 ± 1	144 (181/114)
5	+13:11:26.67	-1:19:03.88	19.64 ± 0.14	3.2 ± 0.1	1.8 ± 0.1	0.38 ± 0.01	79 ± 1	80 (100/63)
6	+13:11:26.38	-1:19:56.51	18.33 ± 0.14	3.4 ± 0.1	1.7 ± 0.1	0.35 ± 0.01	34 ± 1	181 (228/144)
7	+13:11:27.06	-1:19:36.88	18.25 ± 0.01	6.0 ± 0.1	4.9 ± 0.1	0.17 ± 0.01	5 ± 1	147 (185/117)
8	+13:11:24.62	-1:21:11.10	18.24 ± 0.13	4.4 ± 0.3	2.1 ± 0.1	0.55 ± 0.03	136 ± 1	170 (215/135)
9	+13:11:25.55	-1:20:17.25	19.17 ± 0.10	6.0 ± 0.1	2.6 ± 0.1	0.15 ± 0.02	96 ± 3	97 (122/77)
10	+13:11:27.30	-1:19:05.17	19.62 ± 0.15	3.8 ± 0.1	1.7 ± 0.2	0.33 ± 0.01	171 ± 2	81 (102/64)
11	+13:11:28.50	-1:18:44.81	18.64 ± 0.09	3.9 ± 0.1	3.0 ± 0.2	0.56 ± 0.03	179 ± 1	115 (144/91)
12	+13:11:29.55	-1:18:34.66	18.25 ± 0.13	4.1 ± 0.2	2.0 ± 0.1	0.41 ± 0.01	172 ± 1	175 (221/139)
13	+13:11:25.27	-1:20:02.92	19.65 ± 0.12	1.0 ± 0.1	1.7 ± 0.1	0.78 ± 0.01	93 ± 1	81 (102/65)
14	+13:11:27.56	-1:20:02.51	17.74 ± 0.01	8.9 ± 0.1	8.0 ± 0.1	0.15 ± 0.01	57 ± 1	147 (185/116)
15	+13:11:26.62	-1:19:47.96	19.69 ± 0.01	3.5 ± 0.1	2.4 ± 0.1	0.35 ± 0.01	165 ± 1	75 (95/60)
16	+13:11:24.36	-1:21:07.57	18.83 ± 0.12	6.1 ± 0.2	1.5 ± 0.1	0.11 ± 0.02	173 ± 7	138 (174/110)
17	+13:11:28.27	-1:19:31.55	18.38 ± 0.14	6.0 ± 0.1	2.4 ± 0.2	0.32 ± 0.02	148 ± 1	149 (188/119)
18	+13:11:27.99	-1:20:07.71	17.66 ± 0.01	5.3 ± 0.1	3.8 ± 0.1	0.06 ± 0.01	176 ± 1	205 (259/163)
19	+13:11:28.90	-1:19:02.55	19.00 ± 0.14	5.1 ± 0.1	3.6 ± 0.3	0.42 ± 0.01	84 ± 1	83 (105/66)
20	+13:11:29.47	-1:19:16.58	18.77 ± 0.13	4.0 ± 0.1	1.0 ± 0.1	0.58 ± 0.02	56 ± 1	174 (220/139)
21	+13:11:28.52	-1:19:58.47	18.27 ± 0.14	3.3 ± 0.1	2.6 ± 0.1	0.42 ± 0.02	159 ± 1	153 (192/121)
22	+13:11:31.57	-1:19:32.70	17.04 ± 0.01	2.3 ± 0.1	4.9 ± 0.1	0.20 ± 0.01	150 ± 1	258 (325/205)
23	+13:11:28.38	-1:20:43.40	17.75 ± 0.01	5.6 ± 0.1	7.6 ± 0.1	0.12 ± 0.01	17 ± 1	177 (223/140)
24	+13:11:27.29	-1:20:58.41	19.06 ± 0.12	1.3 ± 0.1	2.4 ± 0.1	0.44 ± 0.03	169 ± 1	97 (123/77)
25	+13:11:29.24	-1:19:46.93	19.53 ± 0.14	4.7 ± 0.4	0.6 ± 0.1	0.60 ± 0.02	142 ± 1	140 (176/111)
26	+13:11:30.91	-1:18:52.53	20.28 ± 0.14	4.3 ± 0.1	0.7 ± 0.1	0.45 ± 0.01	104 ± 1	84 (106/67)
27	+13:11:31.68	-1:19:24.65	18.82 ± 0.10	4.1 ± 0.1	3.4 ± 0.1	0.43 ± 0.04	90 ± 1	96 (121/77)
28	+13:11:28.62	-1:20:25.10	18.41 ± 0.01	6.0 ± 0.1	2.7 ± 0.1	0.09 ± 0.01	24 ± 1	136 (172/108)
29	+13:11:30.23	-1:20:42.74	17.11 ± 0.01	3.1 ± 0.1	5.7 ± 0.1	0.16 ± 0.01	83 ± 1	255 (321/202)
30	+13:11:28.78	-1:20:26.54	18.38 ± 0.02	4.8 ± 0.1	7.2 ± 0.2	0.44 ± 0.05	50 ± 2	94 (119/75)
31	+13:11:30.44	-1:20:29.13	17.62 ± 0.02	2.6 ± 0.1	1.9 ± 0.1	0.10 ± 0.02	65 ± 3	238 (299/189)
32	+13:11:29.66	-1:20:27.86	16.39 ± 0.01	1.2 ± 0.1	10.1 ± 0.1	0.14 ± 0.01	144 ± 1	303 (382/241)
33	+13:11:28.08	-1:21:36.68	18.76 ± 0.16	3.8 ± 0.5	1.9 ± 0.3	0.57 ± 0.03	175 ± 1	132 (166/105)
34	+13:11:32.03	-1:18:53.65	19.06 ± 0.17	4.5 ± 0.3	3.5 ± 0.5	0.05 ± 0.01	167 ± 6	82 (103/65)
35	+13:11:32.88	-1:19:31.48	16.36 ± 0.02	5.5 ± 0.1	10.1 ± 0.2	0.29 ± 0.01	61 ± 1	233 (293/185)
36	+13:11:30.11	-1:19:55.90	18.72 ± 0.14	2.9 ± 0.1	1.9 ± 0.1	0.07 ± 0.01	107 ± 1	135 (170/107)
37	+13:11:28.02	-1:21:12.90	18.90 ± 0.18	4.7 ± 0.4	2.6 ± 0.4	0.20 ± 0.01	95 ± 1	104 (131/83)
38	+13:11:30.15	-1:20:40.11	17.66 ± 0.01	2.5 ± 0.1	5.3 ± 0.1	0.36 ± 0.01	52 ± 1	180 (227/143)
39	+13:11:30.40	-1:20:51.69	17.64 ± 0.01	6.0 ± 0.1	6.0 ± 0.1	0.15 ± 0.01	89 ± 1	192 (241/152)
40	+13:11:32.28	-1:19:46.72	17.59 ± 0.01	5.2 ± 0.1	4.4 ± 0.1	0.04 ± 0.01	144 ± 1	215 (271/171)

[1] Total F775W AB magnitude obtained from the surface brightness profile fitting
[2] Circularized physical half light radius in units of kpc
[3] Estimated galaxy velocity dispersion, see text for details, and the corresponding 1σ range

Table 3.7: Table of galaxy properties continued...

ID	RA	Dec	m_{AB}[1]	n_{ser}	R_e[2] (kpc)	$1-b/a$	PA (°)	σ_{est}[3] (km/s)
41	+13:11:32.15	-1:19:24.22	18.26 ± 0.13	4.4 ± 0.4	2.5 ± 0.1	0.19 ± 0.01	24 ± 3	156 (196/124)
42	+13:11:30.20	-1:20:28.41	17.54 ± 0.01	2.5 ± 0.1	3.2 ± 0.1	0.13 ± 0.01	125 ± 6	197 (248/156)
43	+13:11:29.18	-1:21:16.67	17.99 ± 0.01	4.6 ± 0.1	4.6 ± 0.1	0.10 ± 0.01	178 ± 1	176 (222/140)
44	+13:11:30.04	-1:20:15.10	19.02 ± 0.01	3.8 ± 0.1	2.7 ± 0.1	0.37 ± 0.02	116 ± 1	86 (109/69)
45	+13:11:30.18	-1:20:17.29	19.50 ± 0.01	6.0 ± 0.1	1.3 ± 0.1	0.41 ± 0.01	59 ± 1	108 (136/86)
46	+13:11:29.17	-1:20:53.83	18.95 ± 0.12	2.7 ± 0.1	1.0 ± 0.1	0.19 ± 0.01	178 ± 1	160 (201/127)
47	+13:11:32.83	-1:19:58.55	16.15 ± 0.01	4.6 ± 0.1	8.3 ± 0.1	0.31 ± 0.01	22 ± 1	292 (370/230)
48	+13:11:29.93	-1:21:00.55	18.84 ± 0.01	5.2 ± 0.1	1.9 ± 0.1	0.12 ± 0.01	25 ± 1	114 (143/90)
49	+13:11:32.26	-1:19:36.44	18.92 ± 0.01	4.8 ± 0.1	3.5 ± 0.1	0.36 ± 0.01	39 ± 6	81 (102/64)
50	+13:11:30.75	-1:20:43.62	17.82 ± 0.01	3.5 ± 0.1	4.2 ± 0.1	0.12 ± 0.01	174 ± 1	185 (233/147)
51	+13:11:30.56	-1:20:34.81	18.97 ± 0.02	3.5 ± 0.1	1.4 ± 0.1	0.35 ± 0.01	70 ± 6	124 (153/100)
52	+13:11:30.56	-1:20:45.35	18.13 ± 0.01	4.3 ± 0.1	2.0 ± 0.1	0.12 ± 0.02	92 ± 3	173 (213/135)
53	+13:11:29.49	-1:21:05.48	19.82 ± 0.01	3.0 ± 0.1	0.8 ± 0.1	0.24 ± 0.01	179 ± 1	77 (98/62)
54	+13:11:29.26	-1:21:37.37	18.77 ± 0.09	3.1 ± 0.1	1.9 ± 0.1	0.53 ± 0.03	118 ± 1	131 (165/104)
55	+13:11:29.30	-1:21:55.18	18.45 ± 0.01	4.1 ± 0.1	3.1 ± 0.1	0.28 ± 0.01	144 ± 1	146 (184/116)
56	+13:11:33.36	-1:19:16.81	20.81 ± 0.02	2.7 ± 0.1	0.5 ± 0.1	0.06 ± 0.01	167 ± 5	77 (96/61)
57	+13:11:33.49	-1:19:42.82	18.76 ± 0.15	5.3 ± 0.1	2.9 ± 0.3	0.10 ± 0.03	17 ± 2	107 (135/85)
58	+13:11:31.31	-1:21:25.05	17.79 ± 0.01	5.0 ± 0.1	6.3 ± 0.2	0.09 ± 0.01	65 ± 2	145 (179/116)
59	+13:11:30.21	-1:21:18.09	19.40 ± 0.01	3.3 ± 0.1	0.9 ± 0.1	0.27 ± 0.01	171 ± 1	135 (170/107)
60	+13:11:31.27	-1:21:27.71	18.25 ± 0.01	3.5 ± 0.1	1.7 ± 0.1	0.25 ± 0.03	61 ± 2	175 (220/139)
61	+13:11:31.26	-1:20:52.44	18.52 ± 0.16	5.5 ± 0.1	1.8 ± 0.3	0.07 ± 0.01	41 ± 8	156 (196/124)
62	+13:11:31.32	-1:20:44.07	19.58 ± 0.02	5.7 ± 0.2	0.9 ± 0.1	0.04 ± 0.07	18 ± 2	121 (149/97)
63	+13:11:31.17	-1:21:27.72	19.16 ± 0.01	3.2 ± 0.1	1.6 ± 0.1	0.17 ± 0.02	138 ± 1	102 (130/82)
64	+13:11:30.22	-1:21:42.98	18.65 ± 0.15	5.3 ± 0.1	1.4 ± 0.2	0.51 ± 0.02	24 ± 1	165 (207/131)
65	+13:11:34.93	-1:19:24.36	18.69 ± 0.15	5.1 ± 0.1	2.6 ± 0.2	0.13 ± 0.01	2 ± 1	117 (148/93)
66	+13:11:31.97	-1:20:58.57	18.54 ± 0.01	5.8 ± 0.1	5.1 ± 0.2	0.06 ± 0.01	24 ± 2	86 (109/68)
67	+13:11:34.23	-1:21:01.72	18.01 ± 0.07	2.3 ± 0.2	3.1 ± 0.3	0.61 ± 0.02	177 ± 2	164 (207/130)
68	+13:11:35.76	-1:20:12.09	18.16 ± 0.02	1.9 ± 0.1	5.1 ± 0.2	0.13 ± 0.01	15 ± 2	111 (140/88)
69	+13:11:35.03	-1:20:04.29	18.75 ± 0.03	4.6 ± 0.1	2.9 ± 0.2	0.31 ± 0.05	11 ± 3	100 (127/79)
70	+13:11:32.28	-1:21:37.97	18.26 ± 0.02	4.4 ± 0.1	3.4 ± 0.1	0.27 ± 0.01	120 ± 1	146 (183/116)
71	+13:11:32.38	-1:22:10.64	18.11 ± 0.01	5.5 ± 0.1	4.1 ± 0.1	0.20 ± 0.01	63 ± 3	146 (180/115)
72	+13:11:34.26	-1:21:18.50	19.03 ± 0.12	3.1 ± 0.1	1.8 ± 0.1	0.53 ± 0.02	90 ± 1	113 (143/90)
73	+13:11:35.37	-1:21:18.87	18.85 ± 0.14	3.9 ± 0.1	1.7 ± 0.1	0.24 ± 0.01	66 ± 1	129 (163/103)
74	+13:11:35.72	-1:21:09.01	19.00 ± 0.15	6.1 ± 0.3	2.8 ± 0.3	0.19 ± 0.01	167 ± 2	95 (119/75)
75	+13:11:34.94	-1:20:58.99	18.29 ± 0.13	3.8 ± 0.2	2.5 ± 0.1	0.31 ± 0.01	117 ± 1	152 (192/121)
76	+13:11:36.79	-1:19:42.49	19.17 ± 0.13	2.8 ± 0.1	3.0 ± 0.1	0.15 ± 0.05	43 ± 6	82 (104/65)
77	+13:11:36.01	-1:19:57.25	19.72 ± 0.11	3.1 ± 0.3	1.3 ± 0.1	0.38 ± 0.01	170 ± 1	86 (109/69)
78	+13:11:35.55	-1:20:42.52	18.58 ± 0.16	5.0 ± 0.2	2.2 ± 0.2	0.05 ± 0.01	90 ± 1	137 (173/109)
79	+13:11:33.45	-1:21:53.28	18.12 ± 0.01	2.8 ± 0.1	1.4 ± 0.1	0.32 ± 0.01	15 ± 1	73 (92/58)
80	+13:11:35.34	-1:21:12.50	19.33 ± 0.14	2.9 ± 0.2	1.8 ± 0.1	0.25 ± 0.01	24 ± 1	94 (118/75)

[1] Total F775W AB magnitude obtained from the surface brightness profile fitting
[2] Circularized physical half light radius in units of kpc
[3] Estimated galaxy velocity dispersion, see text for details, and the corresponding 1σ range

3.7.3 List of Images

Table 3.8: A summary of image systems used in this study. For the columns with redshifts and rms from lensing the values are mean values from Models I and II optimised in the image plane, in brackets the mean of simulations (optimised in the source plane) is given.

Image system	No. of images	z_{sys}^1	$z_{min} - z_{max}^2$	z_s^3	z_{nsie}^6		z_{enfw}^7		rms_{nsie}^8	rms_{enfw}^9
1	7	3.04	3.04	3.04[4]	3.04	(3.04)	3.04	(3.04)	1.72	2.54
2	5	2.46	1.88 - 3.03	-	2.27	(2.28)	2.12	(2.23)	1.59	2.04
3	3	5.47	4.62 - 6.32	-	5.74	(5.88)	5.88	(5.92)	0.70	1.01
4	5	1.21	0.98 - 1.43	-	1.07	(1.06)	1.29	(1.29)	1.64	1.80
5	3	2.87	2.34 - 3.39	-	2.35	(2.37)	2.52	(2.56)	1.31	2.48
6	4	1.08	0.77 - 1.39	-	0.98	(0.97)	1.36	(1.33)	0.77	1.24
7	3	4.87	4.87	4.87[5]	4.87	(4.87)	4.87	(4.87)	10.38	6.40
8	5	2.84	1.31 - 3.35	-	2.26	(2.25)	2.30	(2.36)	2.90[10]	3.51[10]
9	4	3.98	3.50 - 4.46	-	3.52	(3.55)	4.46	(4.41)	1.83	2.77
10	3	1.37	1.37	1.37[5,11]	1.37	(1.37)	1.37	(1.37)	2.50	2.79
11	3	2.44	1.78 - 3.11	-	2.48	(2.56)	2.47	(2.53)	1.23	2.15
12	2	1.83	1.83	1.83[4,5]	1.83	(1.83)	1.83	(1.83)	0.60[10]	0.35[10]
13	4	1.83	1.83	1.83[4,5]	1.83	(1.83)	1.83	(1.83)	2.01	2.88
14	3	0.99	0.77 - 1.21	-	1.21	(1.20)	1.21	(1.18)	0.89[10]	1.74[10]
15	2	3.54	3.04 - 4.04	-	3.04	(3.50)	3.04	(3.47)	1.16[10]	1.46[10]
16	3	1.99	1.59 - 2.38	-	1.66	(1.66)	1.78	(1.83)	2.28	1.48
17	3	2.04	1.65 - 2.42	-	1.71	(1.65)	1.76	(1.89)	2.79	1.35
18	3	2.40	2.03 - 2.77	-	2.77	(2.76)	2.77	(2.77)	1.18	2.42
19	3	2.13	1.84 - 2.41	-	1.84	(1.84)	1.86	(1.86)	1.90	1.56
20	5	2.70	2.15 - 3.25	-	3.25	(3.25)	3.25	(3.25)	4.54	4.31
21	3	1.74	1.36 - 2.13	-	1.50	(1.51)	1.56	(1.63)	1.48	1.64
22	3	2.04	1.68 - 2.41	-	1.98	(1.84)	1.92	(1.86)	1.52	1.28
23	3	2.01	1.62 - 2.40	-	2.02	(1.90)	1.90	(1.86)	1.32	1.40
24	5	3.09	2.47 - 3.71	-	2.47	(2.47)	2.47	(2.53)	5.36	2.22
25	2	4.25	3.41 - 5.08	-	3.41	(3.41)	3.41	(3.41)	6.90	4.81
26	3	1.02	0.33 - 1.71	-	1.71	(1.71)	1.71	(1.71)	3.89	4.98
27	3	2.58	1.91 - 3.25	-	1.91	(2.11)	1.93	(2.53)	4.38	5.37
28	2	1.58	0.02 - 3.15	-	3.15	(3.15)	3.15	(3.14)	2.15	1.64
29	5	3.26	2.60 - 3.93	-	2.60	(2.60)	2.60	(2.71)	6.85	4.34
30	3	3.51	3.08 - 3.94	-	3.94	(3.89)	3.08	(3.56)	1.57[10]	3.63[10]
31	2	2.07	1.58 - 2.57	-	1.92	(1.98)	2.57	(2.45)	0.35[10]	0.72[10]
32	19	1.50	0.50 - 8.00	-	1.29	(1.32)	1.20	(1.26)	0.16[10]	0.13[10]

[1] Redshift of the image system
[2] Redshift range allowed in modelling
[3] Spectroscopic redshift
[4] Spectroscopic redshift Golse 2002
[5] Spectroscopic redshift Frye et al. 2002

[6] Mean redshift for the NSIE-profile from Models I and II
[7] Mean redshift for the ENFW-profile from Models I and II
[8] Mean image rms for the NSIE-profile from Models I and II
[9] Mean image rms for the ENFW-profile from Models I and II
[10] Source plane χ^2

[11] This redshift is taken from Broadhurst et al. (2005a) who quote Fort et al. (1997) as the source of the redshift. We have not been able to confirm this redshift and its use is hence questionable.

Table 3.9: Images used in this study, 1–9.

ID		ID B05	RA	Dec	z_p^1	z_{br}^2	z_s^3
1	a	1.1	+13:11:26.60	-1:19:56.73	-	$3.03^{+0.53}_{-0.53}$	3.04^4
	b	1.2	+13:11:26.43	-1:20:00.29	3.41±0.22	$3.04^{+0.53}_{-0.53}$	-
	c	1.3	+13:11:29.92	-1:21:07.49	3.40±0.30	$3.27^{+0.56}_{-0.56}$	-
	d	1.4	+13:11:33.21	-1:20:27.42	3.34±0.20	$2.94^{+0.52}_{-0.52}$	-
	e	1.5	+13:11:32.08	-1:20:06.01	3.48±0.11	$3.35^{+0.57}_{-0.57}$	-
	f	1.6	+13:11:30.00	-1:20:38.43	3.32±1.26	$1.06^{+0.27}_{-1.91}$	-
	g	-	+13:11:26.58	-1:19:57.35	-	-	-
2	a	2.1	+13:11:26.67	-1:19:55.47	3.02±1.94	$2.62^{+0.48}_{-0.47}$	-
	b	2.2	+13:11:33.11	-1:20:25.51	2.92±0.73	$2.57^{+0.47}_{-0.47}$	-
	c	2.3	+13:11:32.12	-1:20:07.17	2.90±0.63	$2.64^{+0.48}_{-0.48}$	-
	d	2.4	+13:11:29.96	-1:21:06.03	-	$2.36^{+0.44}_{-0.44}$	-
	e	2.5	+13:11:30.03	-1:20:39.38	-	$1.59^{+0.34}_{-0.86}$	-
3	a	3.1	+13:11:32.19	-1:20:27.54	-	$5.48^{+0.85}_{-0.85}$	-
	b	3.2	+13:11:32.32	-1:20:33.30	-	$5.45^{+0.85}_{-0.85}$	-
	c	3.3	+13:11:31.83	-1:20:56.06	-	-	-
4	a	4.1	+13:11:32.32	-1:20:57.37	1.20±0.40	$1.06^{+0.27}_{-0.27}$	-
	b	4.2	+13:11:30.67	-1:21:12.05	1.12±0.34	$1.32^{+0.31}_{-0.30}$	-
	c	4.3	+13:11:30.90	-1:20:08.34	1.14±0.14	$1.47^{+0.33}_{-0.32}$	-
	d	4.4	+13:11:26.43	-1:20:35.45	1.00±0.35	$1.33^{+0.31}_{-0.31}$	-
	e	4.5	+13:11:29.99	-1:20:29.38	-	-	-
5	a	5.1	+13:11:29.21	-1:20:48.79	3.28±0.80	$3.29^{+0.56}_{-0.56}$	-
	b	5.2	+13:11:29.37	-1:20:44.17	-	$3.16^{+0.55}_{-0.55}$	-
	c	5.3	+13:11:34.27	-1:20:20.93	-	$2.15^{+0.41}_{-0.67}$	-
6	a	6.1	+13:11:30.90	-1:19:38.01	1.08±0.33	$1.22^{+0.29}_{-0.29}$	-
	b	6.2	+13:11:33.50	-1:20:12.19	0.96±0.94	$1.31^{+0.30}_{-0.30}$	-
	c	6.3	+13:11:32.90	-1:19:54.52	-	$0.94^{+0.25}_{-0.26}$	-
	d	6.4	+13:11:32.63	-1:19:58.88	-	$1.09^{+0.27}_{-0.27}$	-
7	a	7.1	+13:11:25.60	-1:20:51.86	4.28±0.41	$4.92^{+0.78}_{-0.78}$	4.87^5
	b	7.2	+13:11:30.82	-1:20:13.92	4.42±0.14	$5.20^{+0.81}_{-0.81}$	-
	c	7.3	+13:11:29.97	-1:20:24.89	-	$0.77^{+0.23}_{-4.01}$	-
8	a	8.1	+13:11:32.44	-1:20:50.93	3.10±0.89	$2.63^{+0.48}_{-0.48}$	-
	b	8.2	+13:11:31.55	-1:21:05.56	2.94±1.13	$2.77^{+0.50}_{-0.50}$	-
	c	8.3	+13:11:31.65	-1:20:14.10	-	$2.75^{+0.89}_{-0.49}$	-
	d	8.4	+13:11:25.68	-1:20:20.18	-	$0.70^{+0.22}_{-0.22}$	-
	e	8.5	+13:11:30.48	-1:20:30.51	-	$0.77^{+0.23}_{-2.53}$	-
9	a	9.1	+13:11:30.45	-1:19:48.67	4.30±0.18	$4.97^{+0.78}_{-0.78}$	-
	b	9.2	+13:11:33.67	-1:20:50.35	-	$1.06^{+0.27}_{-0.27}$	-
	c	9.3	+13:11:28.90	-1:21:15.83	-	$5.16^{+0.81}_{-0.81}$	-
	d	9.4	+13:11:26.42	-1:20:26.95	4.98±0.30	$5.17^{+0.81}_{-0.81}$	-

[1] Photometric redshift, this work

[2] Photometric redshift, Broadhurst et al. 2005a

[3] Spectroscopic redshift

[4] Spectroscopic redshift, Golse 2002

[5] Spectroscopic redshift, Frye et al. 2002

Table 3.9: Images used in this study 10–21.

ID		ID B05	RA	Dec	z_p^1	z_{br}^2	z_s^3
10	a	10.1	+13:11:34.13	-1:20:50.87	2.16±0.98	$1.75^{+0.36}_{-0.74}$	1.37^6
	b	10.2	+13:11:28.20	-1:20:12.50	-	$1.54^{+0.33}_{-0.33}$	-
	c	10.3	+13:11:29.46	-1:20:27.76	-	$2.57^{+0.63}_{-0.47}$	-
11	a	11.1	+13:11:33.49	-1:21:06.77	2.96±0.92	$2.91^{+0.51}_{-0.51}$	-
	b	11.2	+13:11:29.20	-1:20:01.31	2.76±2.18	$2.87^{+0.51}_{-0.51}$	-
	c	11.3	+13:11:29.64	-1:20:26.40	-	$1.58^{+0.52}_{-0.73}$	-
12	a	12.2	+13:11:27.51	-1:20:54.90	1.45±0.33	$1.99^{+0.39}_{-0.39}$	$1.834^{4,5}$
	b	-	+13:11:27.36	-1:20:51.85	2.13±0.39	-	-
13	a	-	+13:11:33.42	-1:20:44.40	2.40±0.66	-	-
	b	-	+13:11:26.65	-1:20:22.12	0.52±1.27	-	-
	c	12.1	+13:11:30.50	-1:19:51.45	-	$1.87^{+0.38}_{-0.38}$	$1.834^{4,5}$
	d	12.4	+13:11:29.11	-1:21:10.31	1.98±0.51	$1.92^{+0.38}_{-0.38}$	-
14	a	13.1	+13:11:32.97	-1:19:24.39	-	$1.02^{+0.27}_{-0.28}$	-
	b	13.2	+13:11:33.13	-1:19:25.85	-	$0.72^{+0.23}_{-0.23}$	-
	c	13.3	+13:11:33.54	-1:19:31.15	1.36±0.18	$1.10^{+0.28}_{-0.28}$	-
15	a	14.1	+13:11:29.18	-1:21:41.82	3.50±0.35	$3.37^{+0.82}_{-0.57}$	-
	b	14.2	+13:11:29.60	-1:21:42.65	-	$3.64^{+0.61}_{-0.61}$	-
16	a	15.1	+13:11:28.22	-1:20:15.21	-	$1.99^{+0.39}_{-0.39}$	-
	b	15.2	+13:11:34.22	-1:20:51.33	-	$2.00^{+0.39}_{-0.39}$	-
	c	15.3	+13:11:29.38	-1:20:27.59	-	$1.97^{+0.43}_{-0.39}$	-
17	a	16.1	+13:11:28.13	-1:20:25.34	2.28±0.48	$1.81^{+0.37}_{-0.37}$	-
	b	16.2	+13:11:29.06	-1:20:28.57	-	$2.26^{+0.43}_{-0.43}$	-
	c	16.3	+13:11:34.54	-1:20:46.42	-	$1.80^{+0.37}_{-0.71}$	-
18	a	17.1	+13:11:30.80	-1:20:24.91	-	$2.74^{+0.49}_{-0.49}$	-
	b	17.2	+13:11:30.54	-1:20:27.79	-	$2.02^{+0.40}_{-0.40}$	-
	c	17.3	+13:11:25.13	-1:20:41.89	2.64±0.67	$2.25^{+0.43}_{-0.43}$	-
19	a	18.1	+13:11:28.39	-1:20:09.56	2.44±0.55	$2.56^{+0.47}_{-0.47}$	-
	b	18.2	+13:11:33.97	-1:20:54.56	2.30±0.48	-	-
	c	18.3	+13:11:29.51	-1:20:27.41	-	$1.58^{+0.52}_{-0.73}$	-
20	a	19.1	+13:11:31.78	-1:20:22.61	-	$1.72^{+0.36}_{-0.36}$	-
	b	19.2	+13:11:25.39	-1:20:20.03	-	$2.74^{+0.49}_{-0.49}$	-
	c	19.3	+13:11:32.10	-1:20:59.33	-	$1.57^{+0.34}_{-0.34}$	-
	d	19.4	+13:11:32.20	-1:20:57.15	3.28±0.52	$2.58^{+0.47}_{-0.47}$	-
	e	19.5	+13:11:30.36	-1:20:33.98	-	$4.54^{+0.73}_{-1.66}$	-
21	a	21.1	+13:11:31.17	-1:20:45.80	1.94±0.37	$1.79^{+0.37}_{-0.37}$	-
	b	21.2	+13:11:30.95	-1:20:44.76	-	$1.59^{+0.34}_{-0.34}$	-
	c	21.3	+13:11:25.40	-1:20:11.23	1.78±1.04	$1.78^{+0.36}_{-0.36}$	-

[1] Photometric redshift, this work

[2] Photometric redshift, Broadhurst et al. 2005a

[3] Spectroscopic redshift

[4] Spectroscopic redshift, Golse 2002

[5] Spectroscopic redshift, Frye et al. 2002

[6] This redshift is taken from Broadhurst et al. (2005a) who quote Fort et al. (1997)
as the source of the redshift. We have not been able to confirm this redshift.
The use of the redshift is hence questionable.

Table 3.9: Images used in this study, 22–31.

ID	ID B05	RA	Dec	z_p^1	z_{br}^2	z_s^3
22	a	22.1	+13:11:29.83	-1:20:08.81	1.97±0.44	$1.99^{+0.39}_{-0.39}$	-
	b	22.2	+13:11:29.76	-1:20:23.78	-	$1.99^{+0.39}_{-0.59}$	-
	c	22.3	+13:11:32.56	-1:21:15.93	2.37±0.49	$1.96^{+0.39}_{-0.39}$	-
23	a	23.1	+13:11:29.68	-1:20:10.04	2.03±0.37	$2.03^{+0.40}_{-0.40}$	-
	b	23.2	+13:11:29.70	-1:20:22.91	-	$1.99^{+0.39}_{-0.62}$	-
	c	23.3	+13:11:32.80	-1:21:15.22	-	$2.00^{+0.39}_{-0.39}$	-
24	a	24.1	+13:11:29.34	-1:20:56.20	3.04±1.18	$2.63^{+0.48}_{-0.48}$	-
	b	24.2	+13:11:32.21	-1:19:50.58	-	$2.50^{+0.46}_{-0.46}$	-
	c	24.3	+13:11:30.44	-1:19:34.16	3.04±0.89	$2.43^{+0.45}_{-0.45}$	-
	d	24.4	+13:11:33.87	-1:20:19.88	2.84±1.35	$2.81^{+0.69}_{-0.50}$	-
	e	24.5	+13:11:29.78	-1:20:37.02	-	$4.55^{+0.73}_{-0.80}$	-
25	a	25.1	+13:11:28.64	-1:20:35.01	-	$4.59^{+0.73}_{-0.73}$	-
	b	25.2	+13:11:34.80	-1:20:33.59	3.38±1.73	$4.42^{+0.71}_{-0.71}$	-
26	a	26.1	+13:11:25.30	-1:20:32.78	1.42±0.75	$1.08^{+0.27}_{-0.39}$	-
	b	26.2	+13:11:31.47	-1:20:25.26	-	$1.04^{+0.27}_{-0.27}$	-
	c	26.3	+13:11:30.39	-1:20:32.61	-	$0.77^{+0.23}_{-2.53}$	-
27	a	27.1	+13:11:25.32	-1:20:33.13	1.42±0.75	$1.81^{+0.37}_{-0.37}$	-
	b	27.2	+13:11:31.51	-1:20:24.66	-	$1.58^{+0.34}_{-0.48}$	-
	c	27.3	+13:11:30.34	-1:20:32.92	-	$4.55^{+0.73}_{-1.63}$	-
28	a	28.1	+13:11:28.45	-1:20:10.93	-	$1.17^{+0.29}_{-4.29}$	-
	b	28.2	+13:11:34.41	-1:21:00.02	-	$2.00^{+1.23}_{-0.43}$	-
29	a	29.1	+13:11:29.37	-1:20:57.93	-	$2.47^{+0.46}_{-0.57}$	-
	b	29.2	+13:11:30.18	-1:19:34.23	-	$3.40^{+0.58}_{-0.58}$	-
	c	29.3	+13:11:32.29	-1:19:52.58	-	$2.50^{+0.46}_{-0.46}$	-
	d	29.4	+13:11:33.77	-1:20:20.83	-	$3.35^{+0.57}_{-0.57}$	-
	e	29.5	+13:11:29.88	-1:20:36.62	-	$4.59^{+0.73}_{-1.66}$	-
30	a	30.1	+13:11:32.57	-1:19:19.84	3.39±0.13	$4.49^{+0.72}_{-0.72}$	-
	b	30.2	+13:11:33.33	-1:19:26.08	3.16±1.05	$3.23^{+0.76}_{-0.56}$	-
	c	30.3	+13:11:33.80	-1:19:32.71	3.50±0.21	$3.30^{+0.56}_{-0.56}$	-
31	a	-	+13:11:31.82	-1:19:47.34	2.62±0.63	-	-
	b	-	+13:11:31.71	-1:19:45.97	1.52±0.36	-	-

[1] Photometric redshift, this work
[2] Photometric redshift, Broadhurst et al. 2005a
[3] Spectroscopic redshift

Table 3.9: Images used in this study, 32

ID		ID B05	RA	Dec	z_p^1	z_{br}^2	z_s^3
32	a	-	+13:11:33.59	-1:20:05.99	-	-	-
	b	-	+13:11:33.58	-1:20:05.49	-	-	-
	c	-	+13:11:33.56	-1:20:04.93	-	-	-
	d	-	+13:11:33.55	-1:20:04.40	-	-	-
	e	-	+13:11:33.53	-1:20:03.64	-	-	-
	f	-	+13:11:33.54	-1:20:04.00	-	-	-
	g	-	+13:11:33.52	-1:20:03.16	-	-	-
	h	-	+13:11:33.51	-1:20:02.72	-	-	-
	i	-	+13:11:33.51	-1:20:02.29	-	-	-
	j	-	+13:11:33.50	-1:20:01.80	-	-	-
	k	-	+13:11:33.48	-1:20:00.80	-	-	-
	l	-	+13:11:33.47	-1:20:00.31	-	-	-
	m	-	+13:11:33.41	-1:19:57.01	-	-	-
	n	-	+13:11:33.42	-1:19:57.44	-	-	-
	o	-	+13:11:33.43	-1:19:57.88	-	-	-
	p	-	+13:11:33.44	-1:19:58.37	-	-	-
	q	-	+13:11:33.45	-1:19:58.75	-	-	-
	r	-	+13:11:33.45	-1:19:59.25	-	-	-
	s	-	+13:11:33.47	-1:19:59.81	-	-	-

[1] Photometric redshift, this work
[2] Photometric redshift, Broadhurst et al. 2005a
[3] Spectroscopic redshift

3.7.4   multiple images

In this section of the appendix we show image stamps for all multiple images in the different image systems. Observed images are shown on the top row of each figure. Model predictions are shown in the second and third rows for NSIE and ENFW Models II respectively except for the source image for which we show the unlensed image instead. The images used as sources are indicated with a # on the observed image. The thumbnails for the galaxies in the image plane have a box width of 2", those in the source plane have a box width of 1". The scale of the images are also marked on the bottom right corner of the images used as sources. To make the model predictions of the images we have found a mapping from one region of the image plane (i) to another (s) via the source plane, $\theta_s(\beta(\theta_i, z), z)$. Region i is where we expect to see an image from region s. In general a pixel from region i is mapped to a quadrilateral in region s which will overlap several pixels. We have redistributed the flux from pixels in region s to the pixel mapped from region i in a way which preserves surface brightness. This allows us to create an image of region s in region i which has mesh of square pixels in region i. We have used a three colour image composed of F850LP (red), F625W (green) and F475W (blue) for the mapping. For all images the colour cuts are the same expect for images near bright sources for which we have used only a single filter (F775W) with the bright source subtracted in order to show the multiple image more clearly. Image systems 3, 9 and 28 that have very red colours we show as a grey scale images in filter F850LP.

Figure 3.23: Image system 1:
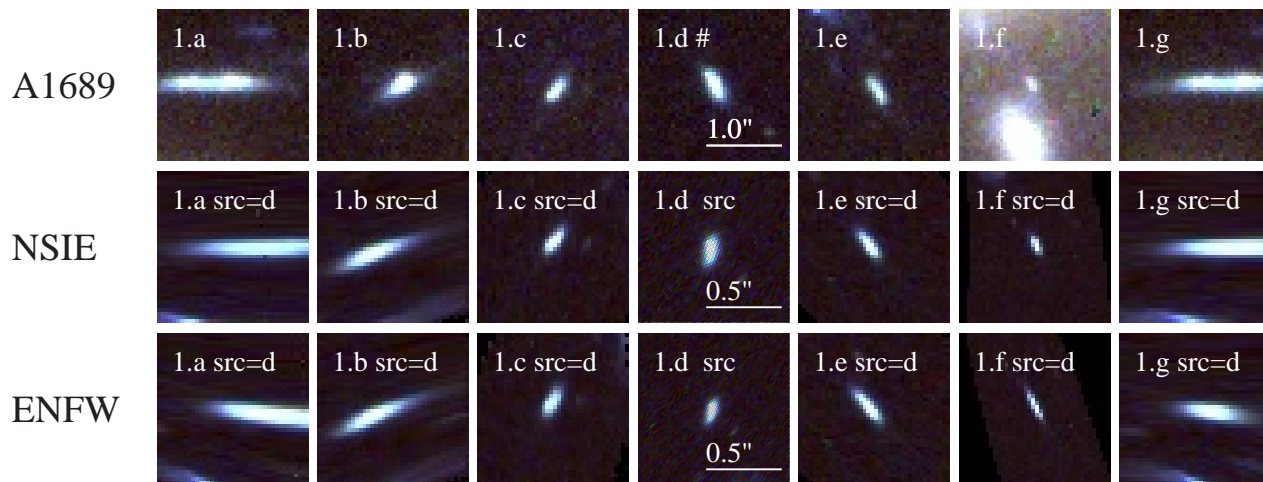
Figure 3.24: Image system 2:
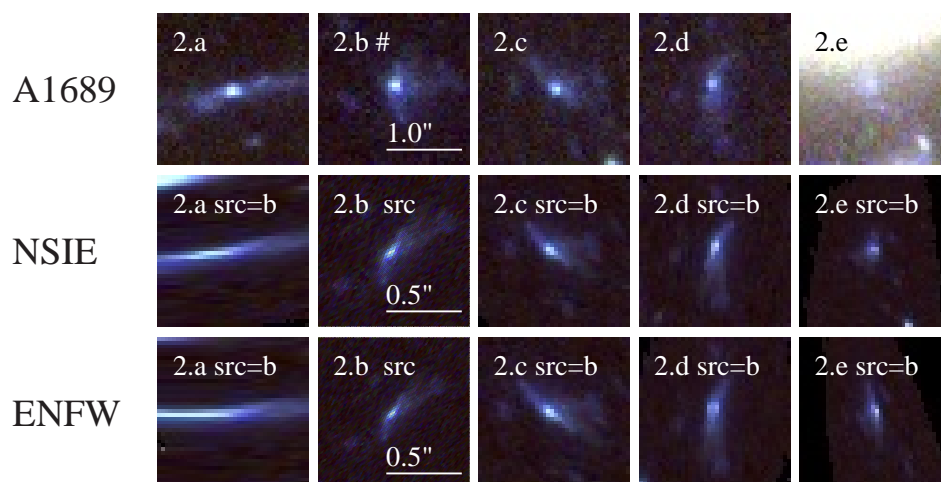
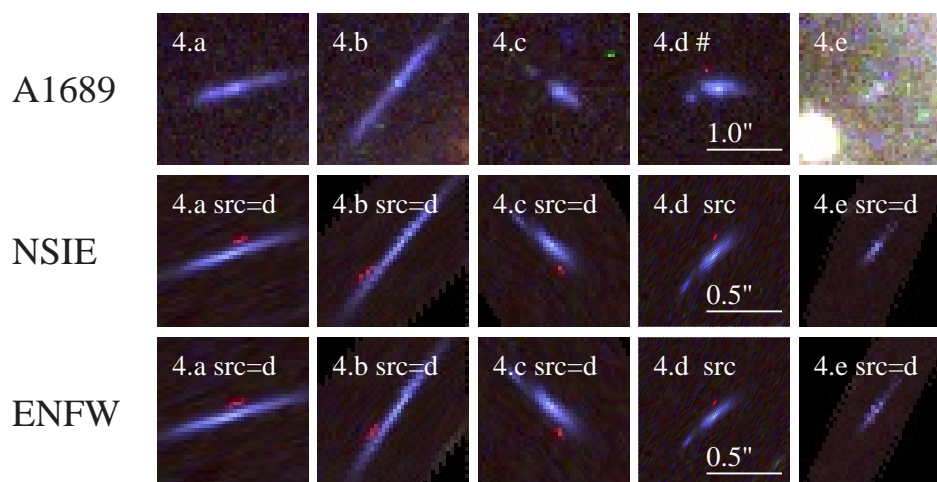Figure 3.25: Image system 3:
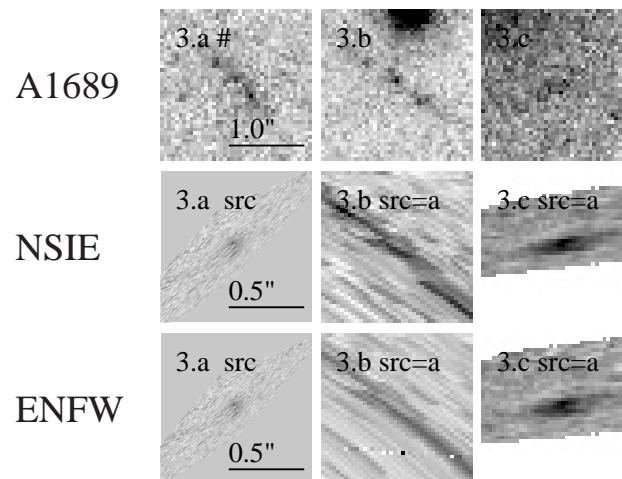
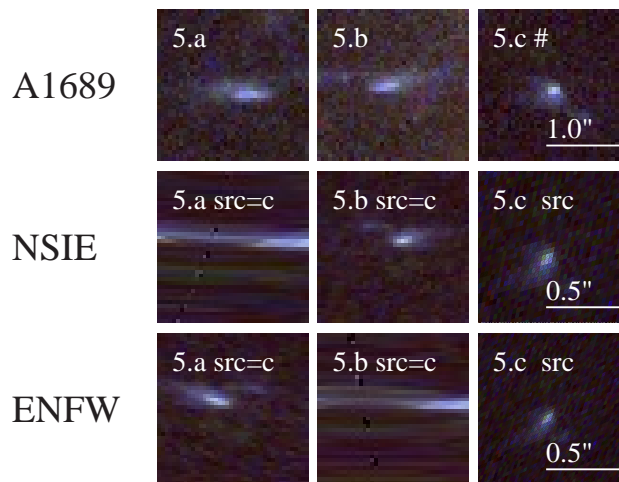Figure 3.26: Image system 4:

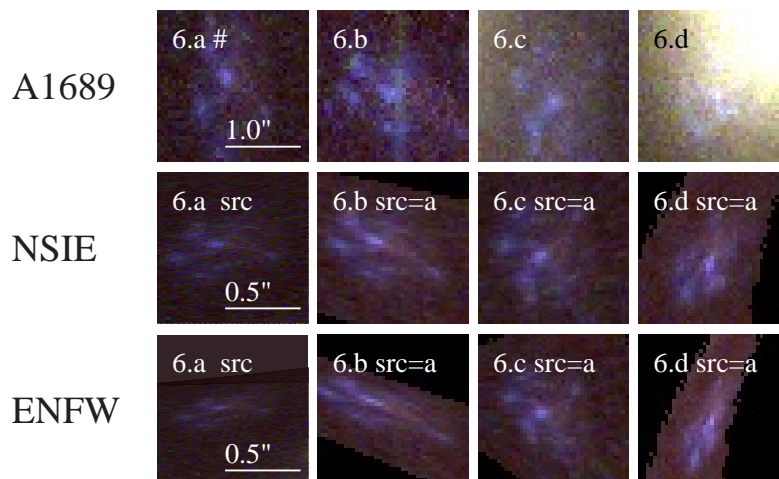Figure 3.27: Image system 5:

Figure 3.28: Image system 6:

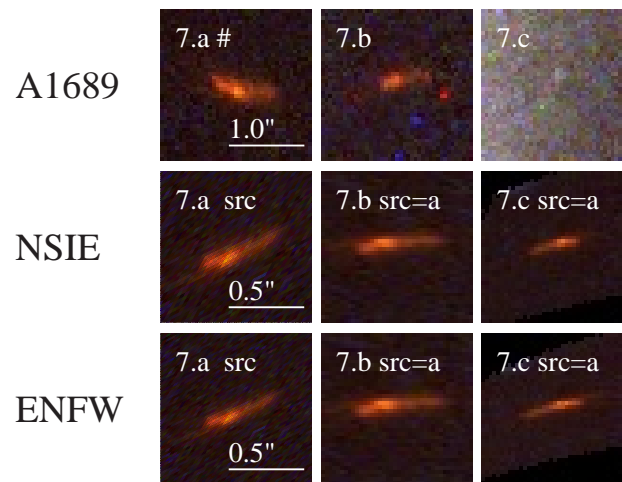Figure 3.29: Image system 7:

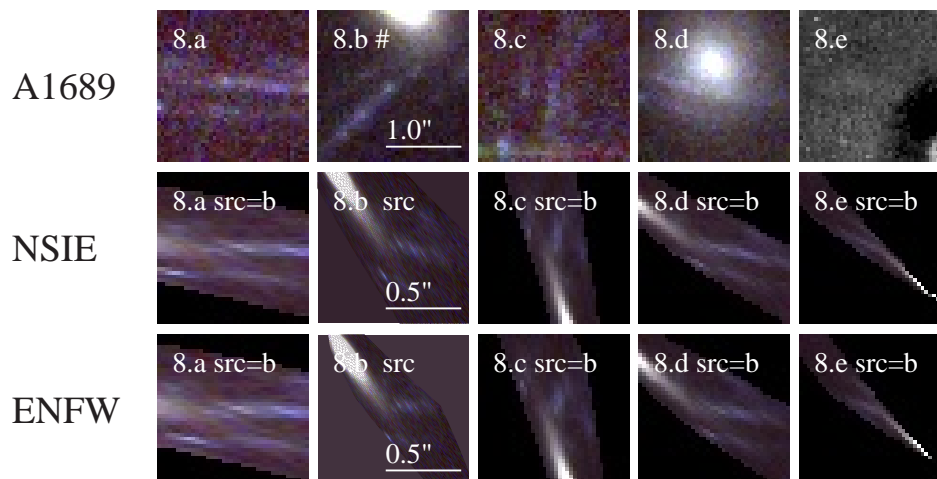Figure 3.30: Image system 8:

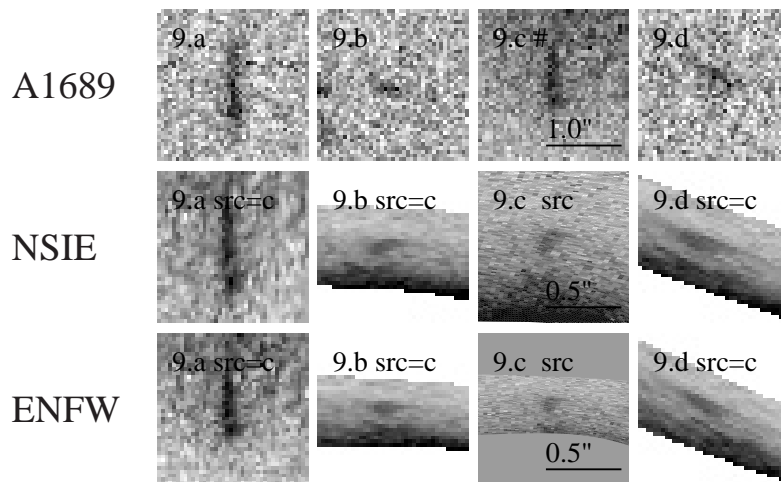Figure 3.31: Image system 9:

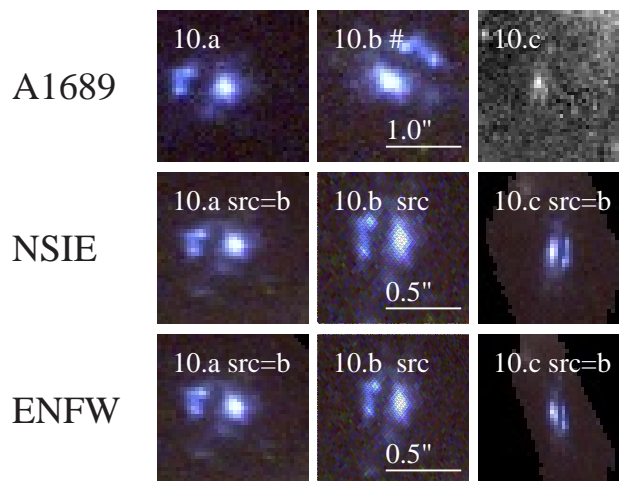Figure 3.32: Image system 10:

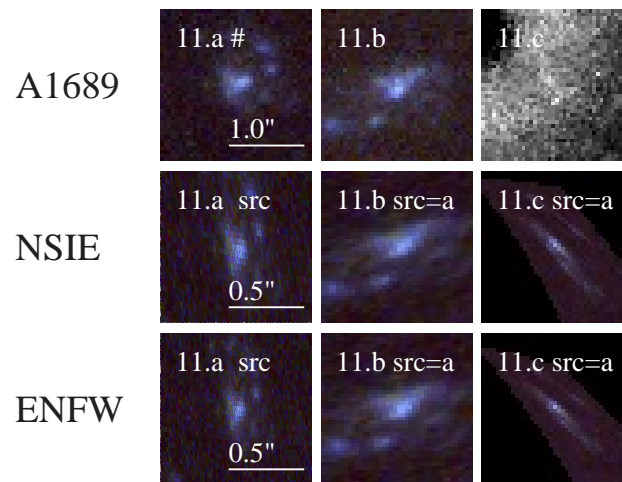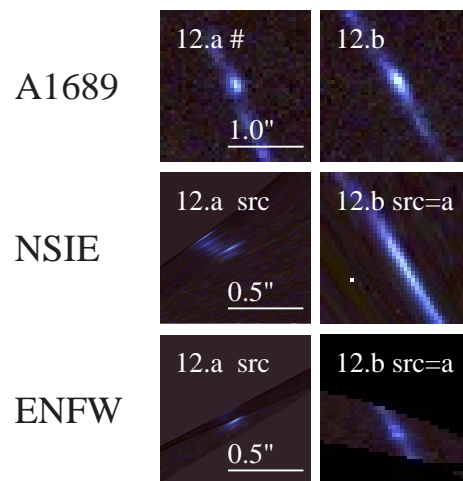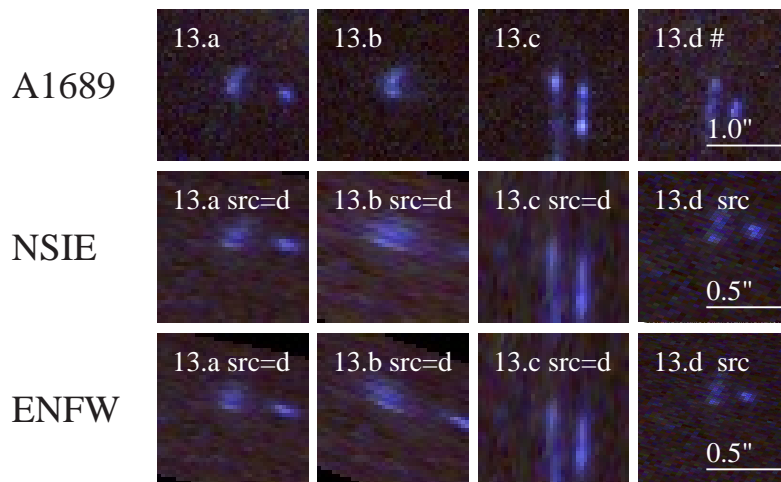Figure 3.33: Image system 11:
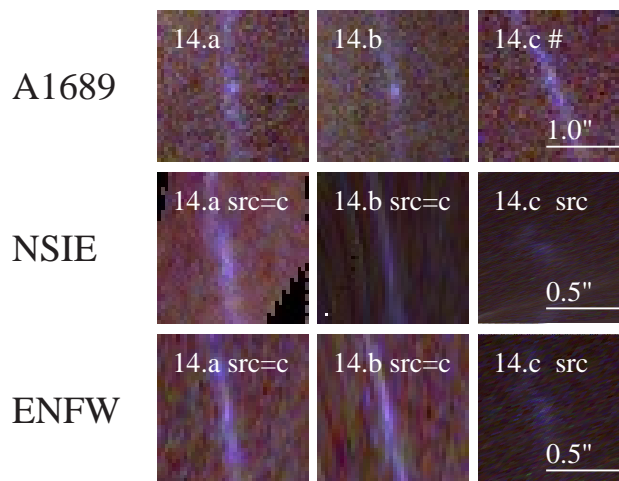

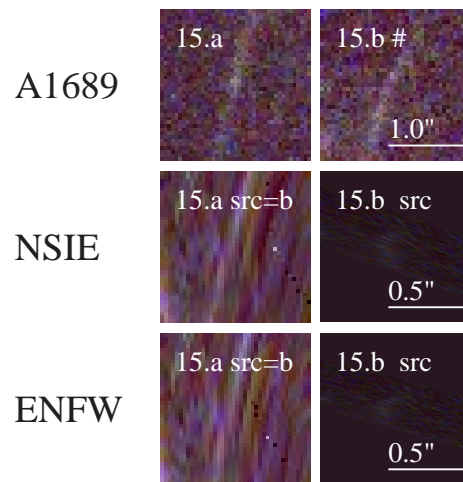Figure 3.34: Image system 12:

Figure 3.35: Image system 13:

Figure 3.36: Image system 14:

Figure 3.37: Image system 15:

A1689

NSIE

ENFW

Figure 3.38: Image system 16:
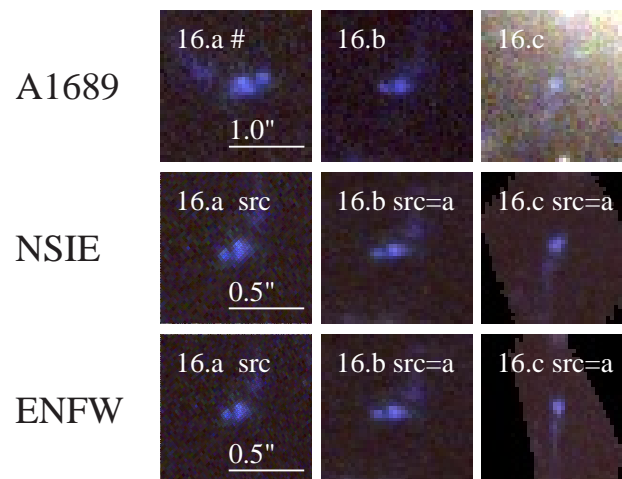

A1689

NSIE

ENFW

Figure 3.39: Image system 17:

Figure 3.40: Image system 18:

Figure 3.41: Image system 19:

A1689

19.a #   19.b   19.c
1.0"

NSIE

19.a src   19.b src=a   19.c src=a
0.5"

ENFW

19.a src   19.b src=a   19.c src=a
0.5"

Figure 3.42: Image system 20:

A1689

20.a   20.b   20.c #   20.d   20.e
1.0"

NSIE

20.a src=c   20.b src=c   20.c src   20.d src=c   20.e src=c
0.5"

ENFW

20.a src=c   20.b src=c   20.c src   20.d src=c   20.e src=c
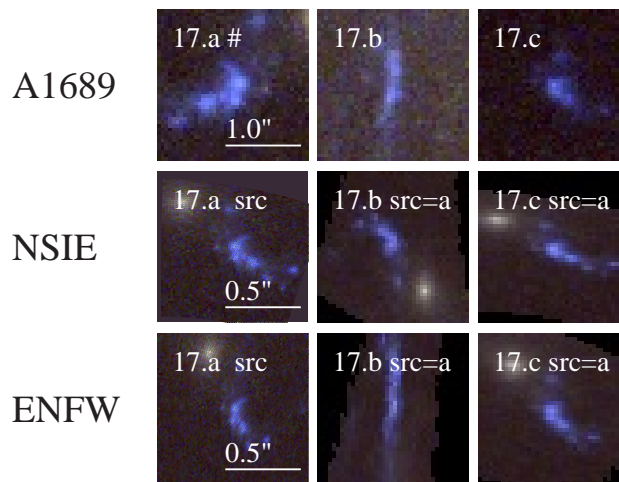0.5"

Figure 3.43: Image system 21:

Figure 3.44: Image system 22:

Figure 3.45: Image system 23:

Figure 3.46: Image system 24:

Figure 3.47: Image system 25:

Figure 3.48: Image system 26:

Figure 3.49: Image system 27:
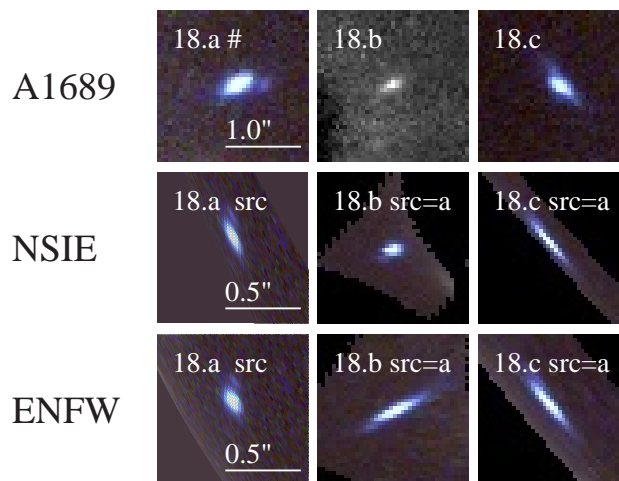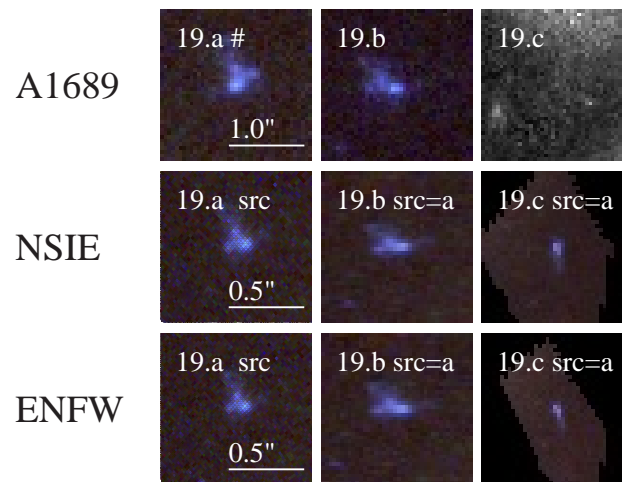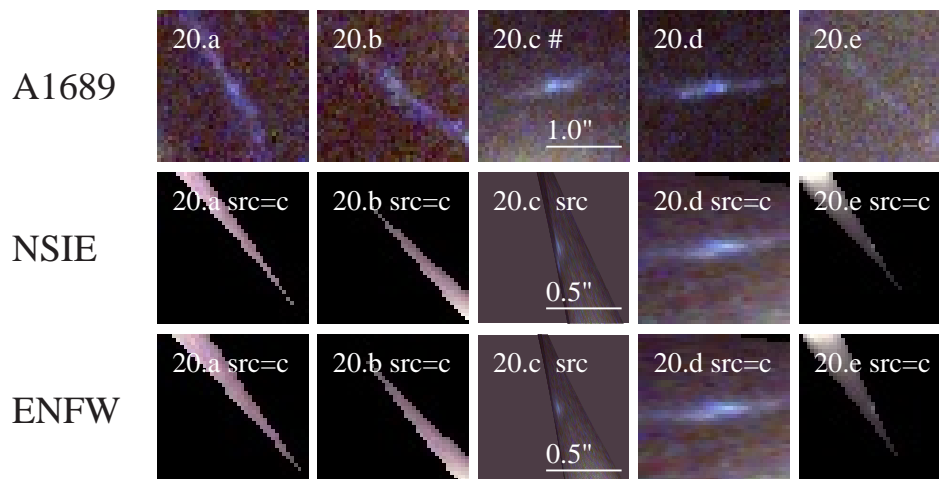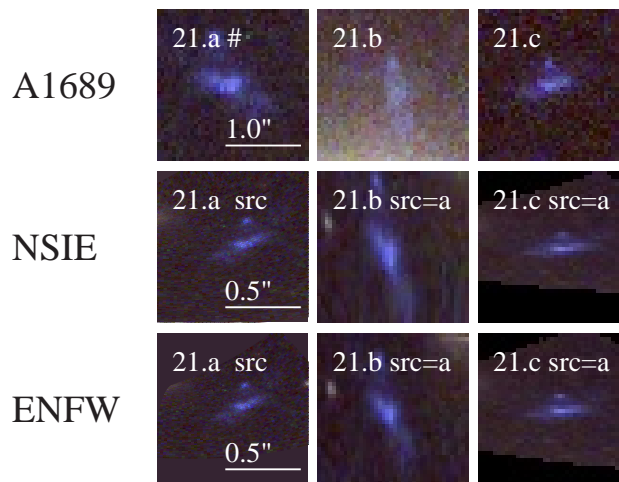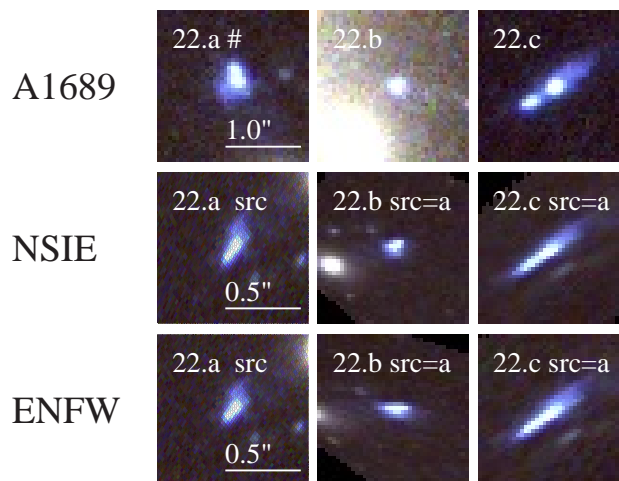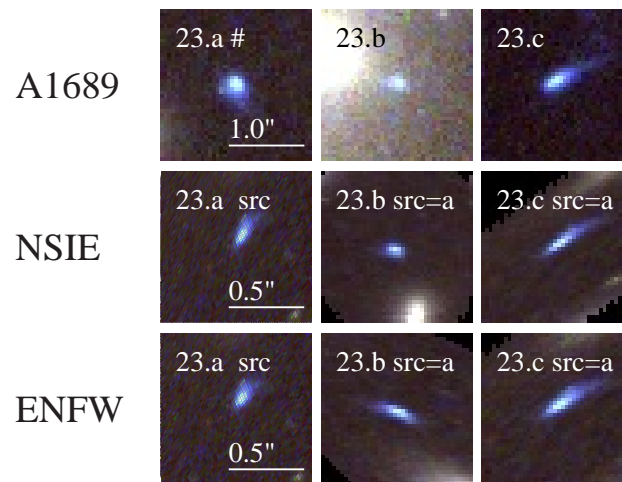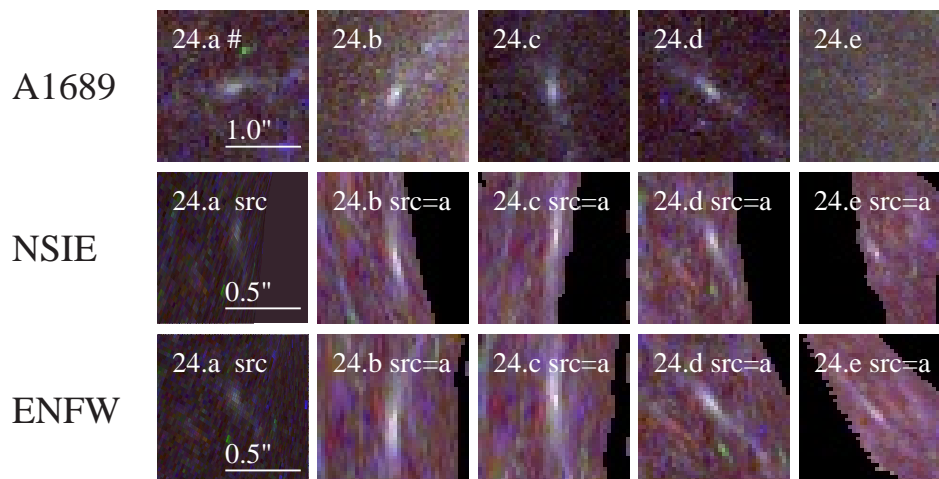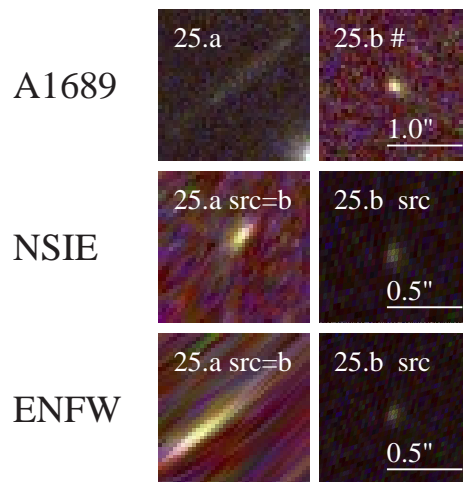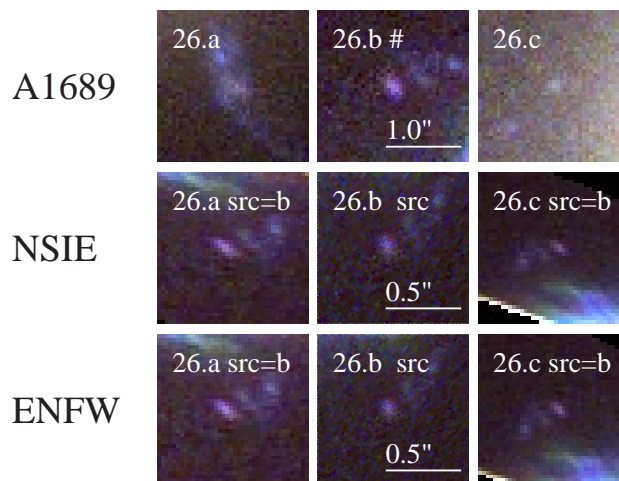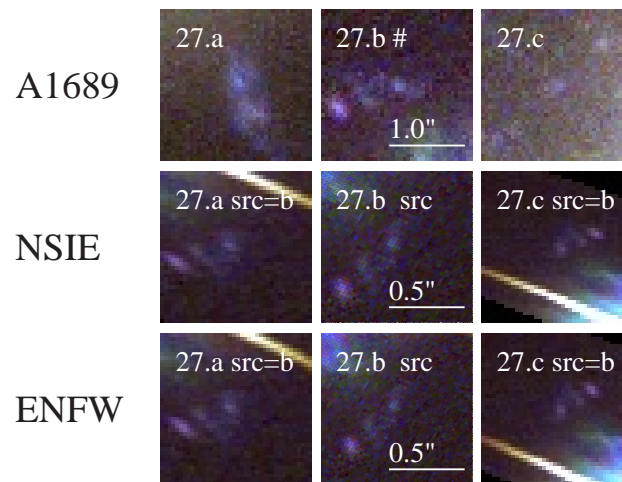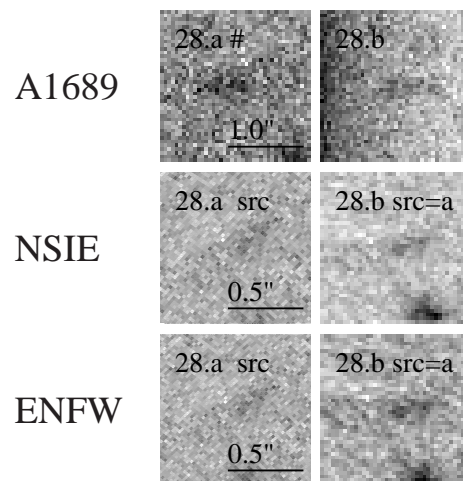

Figure 3.50: Image system 28:

Figure 3.51: Image system 29:
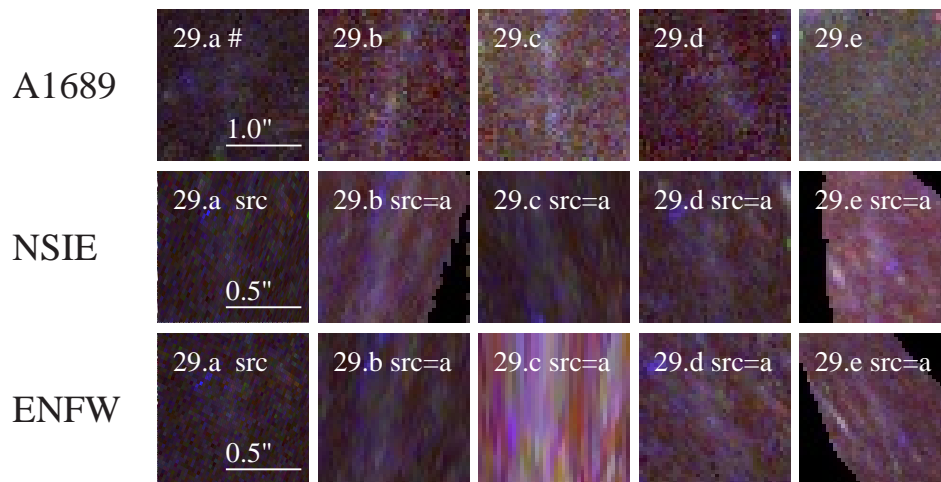
Figure 3.52: Image system 30:
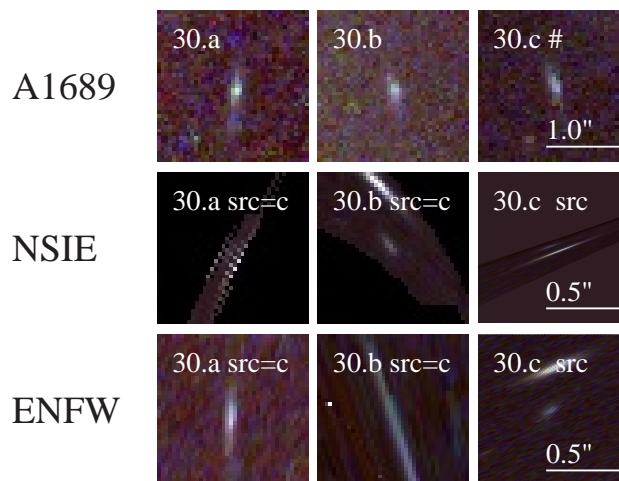
Figure 3.53: Image system 31:

A1689

NSIE

ENFW
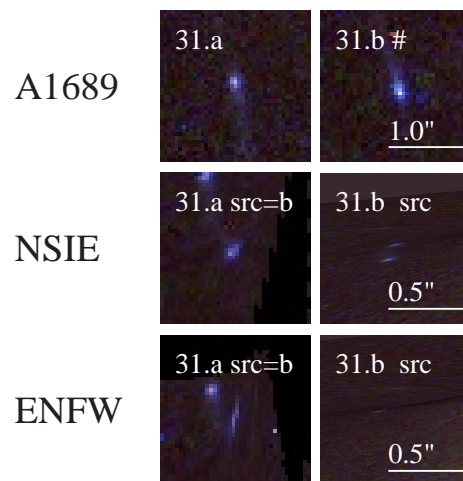
Chapter 4

The sizes of galaxy halos in galaxy cluster Abell 1689[1]

4.1 Abstract

The multiple images observed in galaxy cluster Abell 1689 provide strong constraints not only on the mass distribution of the cluster but also on the ensemble properties of the cluster galaxies. Using parametric strong lensing models for the cluster, and by assuming well motivated scaling laws between the truncation radius s and the velocity dispersion σ of a cluster galaxy we are able to derive sizes of the dark matter halos of cluster galaxies.

For the scaling law expected for galaxies in the cluster environment ($s \propto \sigma$), we obtain $s = 64^{+15}_{-14} \times (\sigma / 220 \text{ km/s})$ kpc. For the scaling law used for galaxies in the field with $s \propto \sigma^2$ we find $s = 66^{+18}_{-16} \times (\sigma / 220 \text{ km/s})^2$ kpc. Compared to halos of field galaxies, the cluster galaxy halos in Abell 1689 are strongly truncated.

4.2 Introduction

Although galaxies are the units of objects seen on cosmological distances, very little is known observationally about the extent of dark matter halos surrounding the galaxies beyond the light emitted by the gas and stars in them. Based on numerical simulations these dark matter halos are expected to extend out to several hundred kpc (e.g. Tormen et al., 1998). Rotation curves of spiral galaxies and the line of sight velocity dispersions of the stars in elliptical galaxies can be measured only out to some tens of kiloparsecs (see e.g. Sofue & Rubin 2001; Bender et al. 1994 and references therein).

---

[1]This chapter is a reproduction of a manuscript that has been accepted for publication in the Astrophysical Journal. The other authors of the manuscript are Stella Seitz and Maurilio Pannella.

The results from these two methods indicate that the masses of galaxies continue to grow roughly linearly with the radius, i.e. the matter in galaxies is closely isothermal. The radial velocities of satellites of galaxies can also be used to estimate the masses of their host galaxies (e.g. Hartwick & Sargent, 1978; Zaritsky et al., 1989; Prada et al., 2003). This has recently been done for the Milky Way by Battaglia et al. (2005) who were able to measure the radial velocity dispersion profile of the Galaxy out to 120 kpc. The method works only for field galaxies since it is sensitive to other nearby massive galaxies and hence the galaxies studied need to be isolated (Brainerd, 2004).

Gravitational lensing is an ideal tool to measure the extents of dark matter halos around galaxies since no optical tracers within the halo are needed. Instead, the halo mass can be inferred from the gravitational lensing of background sources.

Weak lensing can be used to study galactic dark matter halos statistically. The field started from the pioneering work of Tyson et al. (1984), and galaxy-galaxy lensing has now been successfully used both in the field (Brainerd et al., 1996; dell'Antonio & Tyson, 1996; Hudson et al., 1998; Fischer et al., 2000; Smith et al., 2001; Wilson et al., 2001; McKay et al., 2001; Hoekstra, 2003; Hoekstra et al., 2004) and in clusters (Natarajan et al., 1998; Geiger & Schneider, 1999; Natarajan et al., 2002; Gavazzi et al., 2004; Limousin et al., 2006) to measure the masses and extents of galaxy halos. The signal is very weak for individual galaxies and needs to be collected from many galaxies, possibly adopting various scaling laws to compare measurements from lensing galaxies with different luminosities. The different works generally find a tangential shear γ that decreases like $\gamma \propto 1/\theta$ with the radius θ, i.e. the halos stay roughly isothermal beyond the luminous component. In the field the signal from galaxies has been measured out to ~200 kpc (e.g. Wilson et al., 2001; Hoekstra et al., 2004).

The galaxy truncation in clusters has been studied both theoretically and observationally in Natarajan & Kneib (1997); Natarajan et al. (1998); Geiger & Schneider (1998, 1999); Natarajan et al. (2002); Gavazzi et al. (2004); Limousin et al. (2005, 2006). Strong truncation of galaxies is found in Natarajan et al. (1998), Natarajan et al. (2002) and Limousin et al. (2006) when compared to galaxies in the field (truncation radii s^* of L^* galaxies span 17-55 kpc in the 6 clusters vs. s^*=264±42 kpc/h_{70} in the field, Hoekstra et al. 2004). There is a general agreement that the halos of galaxies in dense environments are truncated relative to those in the field although the uncertainties are still large and the sample of clusters used is inhomogeneous. The inherently statistical nature of the methods and the need to assume certain scaling laws further complicate the case. The method used in Natarajan et al. (1998, 2002) also requires that the parameters of the smooth cluster component are known accurately (Natarajan & Kneib, 1997). This is achieved by incorporating also strong lensing constraints in the clusters enabling Natarajan et al. to accurately model the cluster profile.

The typical radius of an Einstein ring of a galaxy is at most a few arcseconds and

so in the strong lensing regime it is not possible to probe the extent of dark matter halos beyond a few arcseconds directly. This makes strong lensing unfeasible to study the dark halos of individual galaxies beyond a few arcseconds in the field. In clusters of galaxies however the combined potentials of the smooth dark matter halo of the cluster as a whole and those of the individual galaxy halos are responsible for the lensing of background sources. This enables us to statistically probe galaxy halos in dense environments using strong gravitational lensing. Since lensing constrains only the total potential of the cluster it is important to have a large number of multiple images with a large radial spread over the cluster in order to investigate the different mass components separately. Abell 1689 is ideally suited for this task with the large number of identified multiple images of many different background sources and well defined strong lensing models (Broadhurst et al., 2005a; Diego et al., 2005b; Zekser et al., 2006; Halkola et al., 2006). In this paper we use the strong lensing models developed in Halkola et al. (2006) to study the truncation of cluster galaxy dark matter halos in A1689. We demonstrate that the models are indeed sensitive to the total mass contained in the cluster galaxies and derive sizes for the galaxies in the cluster. This is the first time the sizes of galaxy halos have been measured in dense cluster environments with strong lensing only.

In section 4.3 we give a brief summary of the models used in Halkola et al. (2006) in particular the modeling of the galaxy component of the cluster, in section 4.4 we outline the methodology used to study the truncation of the cluster galaxies. The results are presented in section 4.5 and in section 4.6 we perform several checks to demonstrate that the results obtained are robust and reasonable. In section 4.7 we compare the results with earlier published studies of galaxy halo truncation before concluding in section 4.8.

The cosmology used throughout this paper is $\Omega_m=0.30$, $\Omega_\Lambda=0.70$ and $H_0=70$ km/s/Mpc.

4.3   Strong Gravitational Lensing Model for A1689

The strong lensing models in this work are based on the parametric models used in Halkola et al. (2006) to study the mass profile of A1689 in detail. Here we give a short summary of the strong lensing modeling but refer the reader to Halkola et al. (2006) for the details.

The multiple images in Halkola et al. (2006) were in most part those identified in Broadhurst et al. (2005a). In total a 107 multiple images in 31 multiple image systems and 1 arc were used. In 5 cases at least one of the images in a system had also a spectroscopic redshift and the redshifts were kept fixed for these systems. The redshifts

of another 26 multiple image systems were estimated using photometric redshifts. In these cases the redshift of an image system was allowed to find its best redshift within the estimated photometric redshift errors. The arc was too faint for good photometry and its reshift is left unconstrained.

The mass in the cluster is assumed to be in two smooth DM halos that are described by either non-singular isothermal ellipsoids (NSIE) or elliptical Navarro-Frenk-White profiles (ENFW). The small scale mass structures associated with the galaxies are modeled with BBS profiles (Brainerd et al., 1996). The BBS profile is a singular isothermal sphere with a truncation radius s. In the central regions ($r < s$) the density profile is isothermal ($\rho \propto r^{-2}$) but there is a truncation of the halo at radius s after which the density falls sharply with $\rho \propto r^{-4}$.

The velocity dispersions of the galaxies are estimated using the Fundamental Plane (FP). The FP ties kinematic (velocity dispersion), photometric (effective surface brightness) and morphological (half light radius) galaxy properties together (Dressler et al., 1987; Djorgovski & Davis, 1987; Bender et al., 1992). Measuring morphological and photometric properties of the galaxies allows us to estimate the galaxy kinematics. We assume that the central velocity dispersions of galaxies, as derived from the FP, are equal to the halo velocity dispersions, and that the masses in disks can be neglected. For some fainter galaxies we have also used the Faber-Jackson relation (Faber & Jackson, 1976, here after FJ relation) that relates the absolute magnitude of a galaxy to its velocity dispersion. The FJ relation has a large intrinsic scatter and the velocity dispersion obtained using FJ have a larger uncertainty than the ones obtained with the FP.

The truncation radii of the galaxies are assumed to follow a scaling law of the form $s_{gal} = s^0 \times (\sigma_{gal}/\sigma^0)^\alpha$. In this paper we discuss the same scaling laws as in Halkola et al. (2006), namely $\alpha = 1$ and $\alpha = 2$. $\alpha=1$ corresponds to tidal truncation of halos in dense cluster environment (Merritt, 1983) whereas galaxies with $\alpha=2$ have a constant mass-to-light ratio and is usually assumed in weak lensing analyses (e.g. Brainerd et al., 1996; Natarajan et al., 1998; Hoekstra et al., 2004). In this paper we explore further the radial extent of the galaxy halos for the scaling laws used in Halkola et al. (2006).

A1689 is an excellent candidate for this work since the large number of multiple images ensures not only that the global mass profile can be constrained very accurately but also the relative contributions of the smooth DM and galaxies can be determined as will be shown later.

4.4 Methodology

In this paper take advantage of the unique opportunity presented in A1689 to use strong lensing and the significant contribution of the cluster galaxies on the positions of the

impressive number of multiple images observed in the cluster.The effect is only observable in the total fit quality and is hence statistical in nature in that extension of individual galaxies cannot be determined.

Unlike the usual galaxy-galaxy lensing in which foreground galaxies weakly distort the shapes of background galaxies this method relies on the changes induced by galaxies on the *positions* of multiply imaged background galaxies. This strong galaxy-galaxy lensing is only applicable in the strong lensing regime where multiple images are observed over a large range of cluster centric radii so that they pose strong constraints both on the total cluster potential and also on the galaxies.

In this section we outline the method used to measure the extents of galaxy halos. The strong lensing models are constrained by the observed multiple images. The positions of the images can be measured to an accuracy of better than 1 pixel or 0.05" on the images from the Advanced Camera for Surveys. The only other measurables are the redshifts of the cluster and the multiple images. The redshift of the cluster is well established from spectroscopic surveys (Teague et al., 1990; Balogh et al., 2002; Duc et al., 2002) and the overall mass scale of the cluster is fixed by the 5 spectroscopic redshifts of multiple image systems. The major uncertainty in the models is the inclusion of the cluster galaxies. In the following we describe the Monte-Carlo simulations used to find the normalization of the scaling law, s^0, and how these simulations can also be used to estimate the error in s^0 due to the uncertainties in the observables.

4.4.1 Monte-Carlo Simulations

A Monte-Carlo run consists of reassigning a new velocity dispersion, σ_{MC}, to each cluster galaxy based on the value σ_{gal} and estimated error determined using the FP or the FJ relation. The new σ_{MC} of a galaxy was drawn from a Gaussian distribution centered on σ_{gal} with a width corresponding to the estimated error. The multiple image positions were similarly varied with assumed error of 1 pixel. In this way we have constructed a simulated galaxy that has properties similar to the one observed within our estimates of the errors.

This cluster can now be analyzed in the same way as the 'original' cluster. This means that we find the optimal parameters for the two smooth DM halos (positions, ellipticities, position angles and the two free parameters of the halos: velocity dispersion and core radius for the NSIE profile and concentration and virial radius for the ENFW profile) and redshifts for the image systems with photometric redshifts.

The simulated clusters used in this work are the same that were used in Halkola et al. (2006) to derive errors for the total mass profile and the parameters of smooth DM halo.

In this work we concentrate on the normalization of the truncation radius s^0 for two scaling laws, $\alpha = 1$ and $\alpha = 2$, which was not done in Halkola et al. (2006). This means

that in addition to optimizing the above mention parameters we also find the optimal value of s^0 for each simulated cluster. This is explained below.

4.4.2 Determining s^0 for a Monte-Carlo Run

The optimal s^0 for each Monte-Carlo run was taken as the one with the minimum $\langle \chi^2 \rangle^{1/2}$ when s^0 was progressively increased from 20 kpc to 200 kpc. The parameter optimization was performed by a source plane minimization for computational reasons. In all subsequent analysis we have used an image plane χ^2 defined as the sum of the squared distances between the observed images and ones predicted by our models. $\langle \chi^2 \rangle^{1/2}$ is hence the rms distance between the observed images and the corresponding model image positions.

We use the shapes of these $\langle \chi^2 \rangle^{1/2}$ vs. s^0 curves to convince the reader that there is clear signal and that s^0 can be constrained in clusters using strong lensing once sufficiently many multiple images can be used to constrain the models.

4.4.3 Determining s^0 for the Cluster

The shape and spread of the $\langle \chi^2 \rangle^{1/2}$ vs. s^0 curves could in principle also be used to derive confidence limits on s^0. This, however, would require us to perform more simulations to derive appropriate $\Delta\chi^2$ levels for the confidence limits. The $\langle \chi^2 \rangle^{1/2}$ vs. s^0 curves do however demonstrate that there is a strong and clean signal that can be used to derive s^0 and the errors for a given scaling law.

The best fitting s^0 and the errors for the cluster are derived from the distribution of the s^0 values obtained in the Monte-Carlo runs instead.

4.5 Results

For the scaling law we need to choose a reference σ^0. The derived s^0 is then the truncation radius of a galaxy with a velocity dispersion equal to this σ. The truncation radii of galaxies with different σs can then be obtained using the appropriate scaling law. In this work we simply assume a fiducial value of σ^0=220 km/s. To compare the s^0 obtained in this work with literature one should scale our s^0 by $(\sigma_{lit}^0 / 220 \text{ km/s})^{\alpha}$.

In creating the simulated clusters the velocity dispersions for the galaxies are drawn from a Gaussian distribution and hence we do not expect to see significant differences in the shapes of the individual $\langle \chi^2 \rangle^{1/2}$ vs. s^0 curves between the different Monte-Carlo runs that would arise from a systematic change in the galaxy component. The curves do vary in their absolute $\langle \chi^2 \rangle^{1/2}$ level however. For this reason we have normalized the individual curves to their respective median $\langle \chi^2 \rangle^{1/2}$ in order to bring all the curves to a similar $\langle \chi^2 \rangle^{1/2}$ level. After this the curves have been renormalized

to the level of the mean median $\langle \chi^2 \rangle^{1/2}$ of all the curves. The scaling of the individual curves is necessary in order to combine the information on s^0 from the different curves.

In Fig. 4.1 the mean curves for 1000 simulated clusters for each of the smooth DM profiles used are shown. NSIE is shown as a dotted line and squares, ENFW as a dashed line and triangles. The left panel shows the curves for $\alpha = 1$ ($s \propto \sigma$) and the right for $\alpha = 2$ ($s \propto \sigma^2$). Combining the two smooth DM profiles yields the solid line and points shown as circles. The points show the 2-sigma clipped mean for each s^0. The error bars show the dispersions of the final clipped points for a given s^0.

The smaller scatter in the points for NSIE models is an indication that the renormalized curves are very similar while the considerable scatter for the ENFW models shows that the curves differ not only in the absolute χ^2 level but also in their shape. The combined curve has been calculated from the NSIE and ENFW curves and not from the curves of each individual Monte-Carlo run for the two models. ENFW smooth DM profiles generally favor slightly larger values for s^0 than the NSIE models ($\Delta s^0 \sim 10$ kpc).

The $\langle \chi^2 \rangle^{1/2}$ vs. s^0 curves are flatter at large (>50 kpc) s^0 than at smaller s^0, this is especially apparent for the cases where the smooth DM is described by an NSIE profile. A possible reason for the shallower slope on the logarithmic horizontal scale (linear in fractional change in mass) in Fig. 4.1 is that the larger extent of the halos, and hence a smoother combined mass profile of the galaxies, makes it easier for the smooth DM component to compensate for the change in the mass in the galaxies. In the small s^0 regime the galaxies have significant local contribution to the image positions which cannot be easily compensated by the smooth DM component.

The curves for the two scaling laws are very similar and we are not able to differentiate between them in terms of quality of fit. This is also seen in weak lensing determinations of the extensions of the dark matter halos of galaxies (Limousin 2006, private communication). A possible explanation is that instead of measuring the extension directly we are in fact measuring the mass of the galaxies. This then creates a degeneracy between the two parameters in the scaling law, namely α and s^0. For a different value of α the same total mass in the galaxies can be obtained by appropriately adjusting s^0.

We would like to stress at this point that the two panels in Fig. 4.1 are only shown to illustrate that the s^0 is indeed constrained and to provide an idea how the fit quality changes when s^0 deviates from the best fit s^0. The $\langle \chi^2 \rangle^{1/2}$ vs. s^0 curves are not used to derive the s^0 of the cluster nor the errors. The estimation of s^0 and errors is done using the histograms of the S^0s obtained using the Monte-Carlo simulations shown in
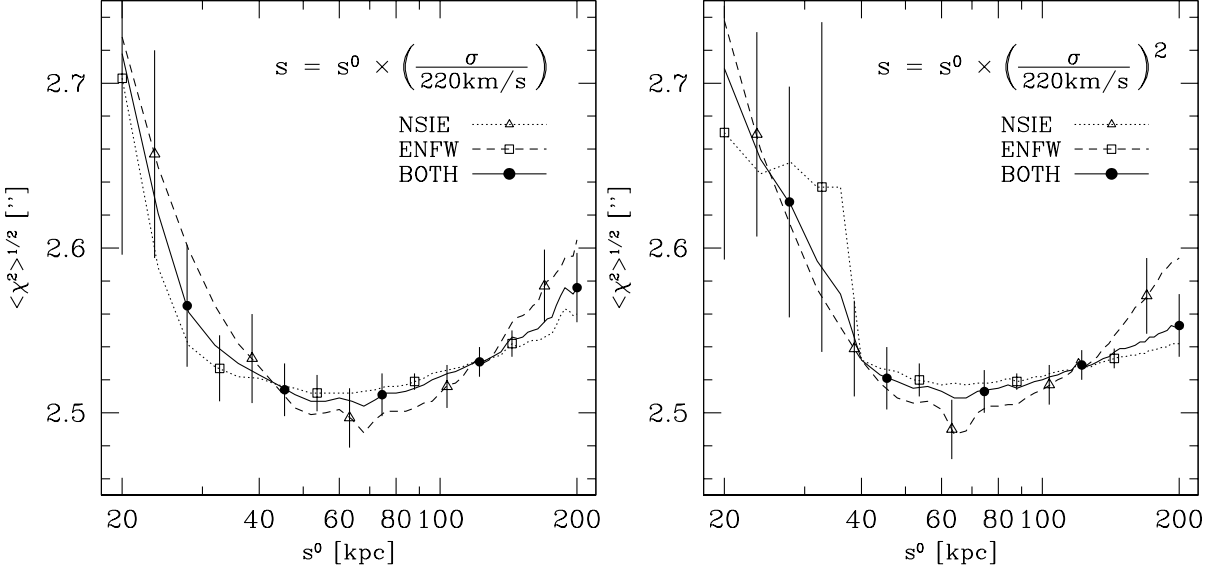
Figure 4.1: The mean $\langle \chi^2 \rangle^{1/2}$ vs. s^0 curve for 1000 simulated clusters for the smooth DM described by both NSIE (dotted line, squares) and ENFW (dashed line, triangles), and the combined data from the two smooth profiles (solid line, circles). The left panels are calculated for the scaling of the truncation radius with $s \propto \sigma$ and the right panels for $s \propto \sigma^2$. The points show the 2-sigma clipped mean for each s^0, and the error bars show the final sigma of the clipped points. Before clipping, the individual curves were normalized to their median $\langle \chi^2 \rangle^{1/2}$ in order to bring all the curves to a similar $\langle \chi^2 \rangle^{1/2}$ level for comparison. The median curve has been brought back to the level of the mean median $\langle \chi^2 \rangle^{1/2}$. The combined curve has been calculated from the NSIE and ENFW curves and not from the individual curves for the two models. The minimum $\langle \chi^2 \rangle^{1/2}$ is obtained at ~60-70 kpc.
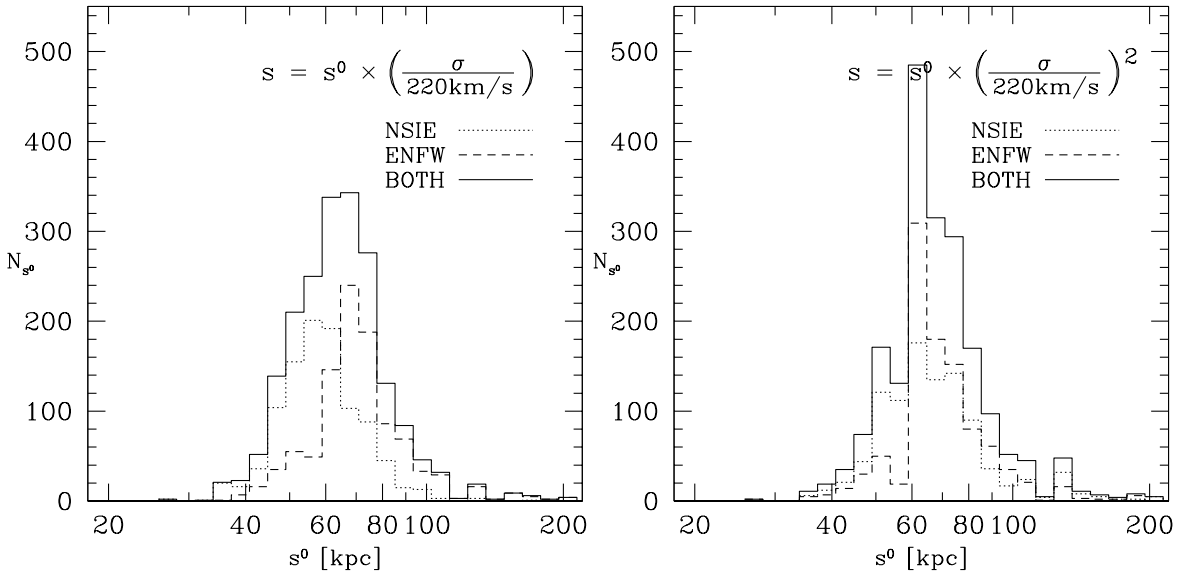
Figure 4.2: The histograms of the s^0 values at which each simulated cluster attains its minimum. The line types used are as above. As is expected, the histograms peak nicely at the positions where the mean curves on the top row also have their minima. The strong clustering of the histogram between $s^0 = 40$ kpc and $s^0 = 90$ kpc with only a few outliers demonstrates that s^0 is strongly constrained. The best fit s^0 and its error has been derived from these histograms.

Fig. 4.2 and explained below.

We finally use the best fitting s^0 of each Monte-Carlo run to derive s^0 for A1689 and estimate the errors. In Fig. 4.2 we show the histograms of s^0 values at which each simulated cluster attains its minimum $\langle \chi^2 \rangle^{1/2}$, i.e. the best fitting s^0 for a given Monte-Carlo run.

As is expected the histograms peak nicely at the positions where the mean curves in Fig. 4.1 also have their minima. The strong clustering of the histograms between $s^0 = 40$ kpc and $s^0 = 90$ kpc with only a few outliers demonstrates that s^0 is well constrained. The flatter $\langle \chi^2 \rangle^{1/2}$ vs. s^0 curves at $s^0 > 50$ kpc for the NSIE models lead to less well defined minima and correspondingly wider distribution of s^0 at large s^0 in the histograms.

The best fit values of s^0 for the different descriptions of the smooth DM component of the cluster are shown in Table 4.1. The values given are the geometric means of the best fit s^0 of all the simulated clusters. We have used the geometric mean to estimate the truncation radius since this corresponds to fractional change in mass and the $\langle \chi^2 \rangle^{1/2}$ vs. s^0 curves in Fig. 4.1 are relatively symmetric in $\log(s^0)$ (although not exactly as discussed earlier). We also give in Table 4.1 the estimated 1- and 2-σ errors of s^0. The errors have been derived from the distribution of the best fit s^0 of the simulated clusters shown in Fig. 4.2. For this the histograms were interpreted as probability distributions of s^0 and 1- and 2-σ confidence intervals were estimated by the regions around the mean that contain 68.3 per cent and 95.4 per cent of the best fit s^0 values from the simulation for the 1- and 2-σ errors respectively. The asymmetry of the distribution becomes evident at higher confidence limits as can be seen in the 2-σ errors.

For the scaling law expected theoretically for galaxies in clusters (Merritt, 1983), $s = s^0 \times (\sigma/\sigma^0)$, we find $s^0 = 64^{+67}_{-28}$ kpc, where the errors given are 2-σ errors. For the scaling law used for galaxies in the field ($s = s^0 \times (\sigma/\sigma^0)^2$), we find $s^0 = 66^{+72}_{-26}$ kpc, the errors are again 2-σ errors.

4.6   Checks on the Robustness of the Results

We have performed the following checks to confirm that the results presented above are reasonable and robust.

4.6.1 σ^0, s^0, α and the Total Mass in Cluster Galaxies

The total mass of a galaxy with a BBS profile can be easily written in terms of its truncation radius s and velocity dispersion σ as is shown in Brainerd et al. (1996). The

Table 4.1: Derived s^0 values and 1- and 2-σ errors for s^0 for the different descriptions of the smooth DM component of cluster. The truncation radius s of a galaxy depends on its velocity dispersion σ and the scaling laws adopted are of the form $s = s^0 \times (\sigma/\sigma^0)^\alpha$. The s^0 values given are the geometric means of the individual minima of the simulated clusters. The errors are derived from the distribution of the minima. We give both 1- and 2-σ errors since the asymmetries of the distributions become more apparent at higher confidence limits. The histograms of the minima for the different descriptions of smooth DM are shown in Fig. 4.2.

Smooth DM profile	ff	s^0 (kpc)	1-σ errors (kpc)	2-σ errors (kpc)
NSIE	1	58	+12 / −11	+32 / −23
ENFW	1	69	+19 / −12	+88 / −30
NSIE & ENFW	1	64	+15 / −14	+67 / −28
NSIE	2	64	+18 / −15	+76 / −25
ENFW	2	66	+18 / −16	+70 / −26
NSIE & ENFW	2	66	+18 / −16	+72 / −26

total mass of the cluster galaxies in A1689 with a scaling law for the truncation of the halos of the from $s = s^0 \times (\sigma/\sigma^0)^\alpha$ can be written simply as,

$$M_{tot} = 7.3 \times 10^5 \left(\frac{s^0}{\text{kpc}}\right) \sum_i \left(\frac{\sigma_i}{\text{km/s}}\right)^2 \left(\frac{\sigma_i}{\sigma^0}\right)^\alpha \text{ M}_\odot, \qquad (4.1)$$

where s_0 is the normalization of the scaling law, σ^0 a reference velocity dispersion and σ_i is the velocity dispersion of galaxy i.

In our study we have taken $\sigma^0 = 220$ km/s. Note that this σ^0 is only a fiducial value and is not related to the L^* of the galaxies in the cluster. With this σ^0 and our set of galaxies in the cluster, the galaxies have the same total mass with the two scaling laws (α=1 and α=2) if $s^0_{\alpha=2} = 0.93 \times s^0_{\alpha=1}$. Note that this relation between $s^0_{\alpha=1}$ and $s^0_{\alpha=2}$ is the same for all $s^0_{\alpha=1}$ and $s^0_{\alpha=2}$.

The fact that the normalizations s^0 obtained for the two scaling laws are very similar ($s^0_{\alpha=1} = 64^{+15}_{-14}$ kpc and $s^0_{\alpha=w} = 66^{+18}_{-16}$ kpc) for σ^0=220 km/s provides strong support for the results and our analysis.

4.6.2   Sensitivity of Cluster Lensing to Extensions of Galaxy Halos

To demonstrate that we are indeed able to measure the extension of galaxy DM halos with strong lensing we have created clusters with an s^0 in the range [20,80] kpc. For each of these clusters we have created a mock set of multiple images that are exactly

reproduced by the cluster. The mock multiple image set is based on the observed multiple images so that the cluster setup is as close to reality as possible. These clusters with known galaxy truncation laws are then analyzed in the same way as is done for A1689.

We find that we are able to recover the input s^0 within a few kpc in all cases. Additionally, both the change in the fit quality ($\Delta \langle \chi^2 \rangle^{1/2} \sim 0.2$") of these new simulated clusters and the distribution of the best fit s^0 is similar to what is observed and shown in Figures 4.1 and 4.2.

4.6.3 Effect of the Choice of Multiple Image Systems

We have in addition checked the sensitivity of the results to our choice of multiple images. This was done by running another 100 Monte-Carlo runs with $\alpha=1$ and the smooth DM described by NSIE profiles. This time for each Monte-Carlo run we selected randomly 20 of the 32 image systems to use as constraints for the modeling. The multiple images with spectroscopic redshifts were always included since they are needed to fix the overall mass scale of the cluster. With fewer constraints we obtained essentially the same s^0 with larger spread in the distribution of s^0 from the different runs. The best fit s^0 obtained with 20 image systems is $s^0 = 59^{+27}_{-19}$ kpc compared to $s^0 = 58^{+12}_{-11}$ kpc with all the image systems, the errors are 1-σ.

When only 20 multiple image systems were used the absolute $\langle \chi^2 \rangle^{1/2}$ stayed at the same level as with all the 32 image systems. This shows that the $\langle \chi^2 \rangle^{1/2}$ level is not driven by only a few image systems but all image systems contribute similarly to the $\langle \chi^2 \rangle^{1/2}$ level. The change in fit quality between best fit s^0 and extrema at $s^0=20$ kpc and $s^0=200$ kpc with fewer image systems is $\Delta \langle \chi^2 \rangle^{1/2} \sim 0.1$" showing that also the individual s^0 are less well constrained with fewer image systems. That no change in s^0 is obtained demonstrates that our results for s^0 are robust.

4.7 Comparison with literature

The extensions of dark matter halos have been measured previously in cluster environment by Natarajan et al. (1998), Natarajan et al. (2002), Gavazzi et al. (2004), and Limousin et al. (2006).

Strong truncation of galaxies is found in Natarajan et al. (1998), Natarajan et al. (2002), and Limousin et al. (2006) when compared to galaxies in the field; the truncation radii of an L_* galaxy span the range 17-55 kpc for the 6 clusters studied in Natarajan et al. (2002). The halos in Limousin et al. (2006) are truncated more with a typical truncation radius below 20 kpc.

An important difference in the analysis of Natarajan et al. (1998, 2002) to that of Limousin et al. (2006) is that Natarajan et al. also include strong lensing features in the

central parts of the clusters to further constrain the mass profile of the selected cluster sample and hence also constrain the galaxy halo parameters stronger. This helps to better define the shear contribution from the cluster galaxies and hence the truncation radius. Another major difference is that Limousin et al. (2006) work exclusively with ground based data where as Hubble Space Telescope data are used in Natarajan et al. (1998, 2002).

The large errors in the work of Gavazzi et al. are caused by the smoothing scale of θ_s=220 kpc/h_{70} employed in their analysis which restricts the achievable resolution. Although they are not able to derive strong limits on the sizes of cluster galaxies, they do find that halos on the periphery of the cluster MS0302+17 are more strongly truncated than the halos on the central regions of the cluster providing thus further confirmation for the tidal stripping scenario.

For the range of σ^0s for the clusters in Natarajan et al. (2002) our s^0 is in the range [32,66] kpc for $\alpha = 1$ and [16,72] kpc for $\alpha = 2$ (their s^0 span 17-55 kpc). In Fig. 4.3 we show a comparison between our results and those of Natarajan et al. (2002) and Limousin et al. (2006). For our points we also show the scaling of s^0 with σ^0 as dotted and dashed lines ($\alpha = 1$ and $\alpha = 2$ respectively). The lines can be used to convert the s^0 and errors to a σ^0 different from 220 km/s, making the comparison between other works easier. The solid line shows the $s - \sigma$ pairs for a galaxy with a total mass of $5\times10^{11}M_\odot$. The scatter of the points is large, though mostly consistent within the large error bars. There is some indication that the galaxy halos in A1689 are more extended than those in most of the other cluster studied.

Natarajan et al. (2002) compared their results for the density of the cluster at the core radius, $\rho(r_c)$, and the truncation radius of galaxies obtained in their analysis and found results in good agreement with Merritt (1983),

$$s^0 \;=\; 40 \; \frac{\sigma^0}{180\mathrm{km/s}} \left(\frac{\rho(r_c)}{3.95 \times 10^6 \mathrm{M_\odot kpc^{-3}}} \right)^{-0.5} \mathrm{kpc}. \qquad (4.2)$$

Using the results for A1689 ($\sigma_{cluster}$=1450 km/s and r_c=77 kpc, Halkola et al., 2006) we get an expected truncation radius of 54 kpc, a little smaller than the ~65 kpc obtained in this work. This (small) difference is in fact also expected since in our analysis we measure the truncation radii of the galaxies along the line of sight. Some of the galaxies will have large cluster-centric distances despite their small projected distances from the center. This supports the idea that the galaxy clusters are mainly truncated by the tidal field of the global potential as assumed by Merritt (1983) and also shown in numerical simulations by Moore et al. (1998); Ghigna et al. (2000).

When comparing the results from different works it should be noted that weak lensing works generally include all the galaxies from the center to the periphery of

the cluster (although Gavazzi et al. 2004 do separate the galaxies in radius). This means that the results are averaged over the cluster galaxy population out to several Mpc (Limousin et al., 2006). With our strong lensing method we include galaxies only out to a projected cluster-centric radius of $r \sim 300$ kpc. The clusters also vary in their central densities complicating direct comparison between clusters. According to Limousin et al. (2006) their cluster sample (Abell clusters A1763, A1835, A2218, A383 and A2390) form a homogeneous set of clusters and hence the results for these clusters should be comparable.

Comparison to field galaxies is shown in Fig. 4.4. In the figure we show points from Brainerd et al. (1996), Fischer et al. (2000), Smith et al. (2001), Hoekstra (2003) and Hoekstra et al. (2004). Adopting σ_{136}^0=136 km/s used by Hoekstra et al. (2004) we obtain $s_{136}^0 = 39_{-17}^{+41}$ kpc for α=1 and $s_{136}^0 = 25_{-10}^{+25}$ kpc for α=2. Similarly to previous studies of cluster galaxies we report a strong truncation of galaxy halos in dense cluster environments compared to galaxy halos in the field.
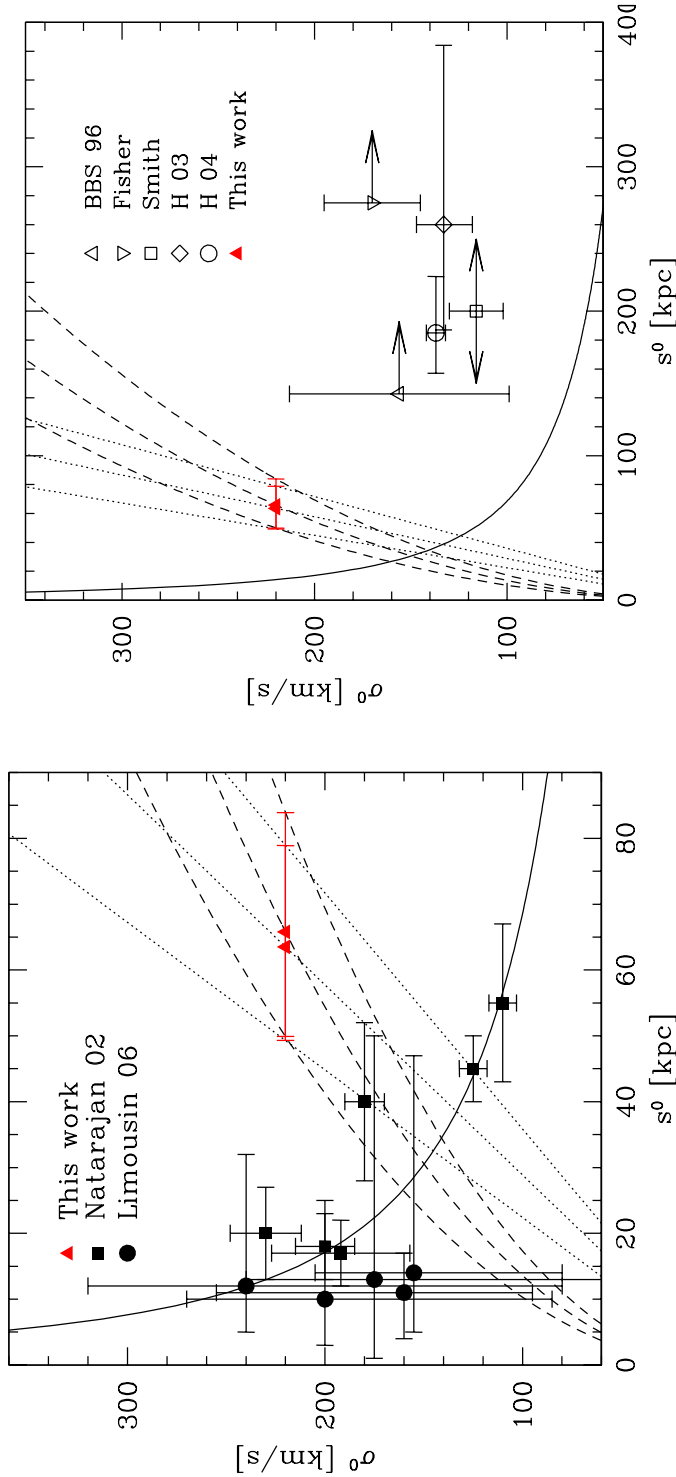
Figure 4.3: A comparison of three studies of galaxy truncation in the dense cluster environments. The red triangles are from this work, squares from Natarajan et al. (2002) and the circles from Limousin et al. (2006). The error bars shown are all 1-σ. The dotted lines show the scaling of the best fit values and errors for $\alpha = 1$, the dashed lines for $\alpha = 2$. With the solid line we show the $s - \sigma$ pairs for a galaxy with a total mass of $5 \times 10^{11} M_\odot$.

Figure 4.4: A comparison of studies of galaxy truncation in the field. The red triangles are from this work. The dotted lines show the scaling of the best fit values and errors for $\alpha = 1$, the dashed lines for $\alpha = 2$. The discrepancy is clear between the results obtained for galaxies in clusters and those in the field. Notice the difference in the horizontal scale between this figure and Fig. 4.3. The solid line shows the $s - \sigma$ pairs for a galaxy with a total mass of $5 \times 10^{11} M_\odot$.

4.8 Summary and Conclusions

In this paper we report the determination of the sizes of galaxy dark matter halos in galaxy cluster A1689. The strong lensing models for the cluster are constrained by 107 multiple images and an arc in 32 image systems. The strong constraints from these images enable us to study not only the global mass profile of the clusters but also the ones of the cluster galaxies. Assuming well motivated scaling laws between the truncation radius of a galaxy halo and its central velocity dispersion (as obtained with the fundamental plane and Faber-Jackson relations) we can study the combined effect of the cluster galaxies on the multiple images and the ensemble properties of the galaxies. This is the first time the sizes of galaxy halos have been measured using strong lensing only.

For a scaling law of the form $s_{gal} = s^0 \times (\sigma_{gal}/\sigma^0)^\alpha$ we find $s^0 = 64^{+67}_{-28}$ kpc for $\alpha = 1$ and $s^0 = 66^{+72}_{-26}$ kpc for $\alpha = 2$. Both values are given for a fiducial galaxy velocity dispersion of σ^0=220 km/s. The errors are 2-σ errors to show the clear asymmetry of the errors. The s^0s are in good agreement with previously determined values in several other clusters using weak lensing (Natarajan et al., 1998, 2002; Limousin et al., 2006).

Galaxy halos in a cluster can be truncated either by the tidal field of the global cluster potential or harassment (Moore et al., 1996, 1998) by other cluster galaxies that strip the halos of galaxies in the central regions of cluster. Mergers of cluster galaxies on the other hand are extremely rare (Ghigna et al., 1998). Once the cluster has been formed the principal mechanism for truncation is the tidal stripping of galaxy halos by the global cluster potential (Ghigna et al., 2000). This is supported by the correlation between the density of the cluster at the core radius and the truncation radii of galaxies shown in Natarajan et al. (2002). The results presented here also support the tidal stripping scenario.

Acknowledgments

Chapter 5

Abell 1689 - Substructuring of the 'smooth' cluster halo

5.1 Introduction

The previous two chapters have dealt with quantities directly measurable with the strong lensing features observable in Abell 1689. In chapter 3 we used the multiple images to constrain the total mass profile of the cluster, as well as the parameters of both NSIE and ENFW profiles. In chapter 4 we used the significant contribution of the cluster galaxies on the positions of the multiple images to constrain the sizes of cluster galaxies in A1689. In this chapter we want to address a topic that so far has received very little attention not only in this thesis but also in the literature. Namely the poor $\langle \chi^2 \rangle^{1/2}$ obtained by strong lensing models in A1689.

Broadhurst et al. (2005a) used a flexible surface mass to model the smooth dark matter distribution of the cluster and the small scale mass structure associated with the galaxies was modelled with a constant mass to light ratio (M/L). The M/L was used to convert the observed light directly to a surface mass density map. The M/L was a free parameter of the models.

In our work we have modelled the smooth cluster mass with 2 parametric halo profiles and the galaxies were modelled with truncated isothermal spheres whose velocity dispersions were measured with the Fundamental Plane. The truncation radii, s, of the cluster galaxy haloes were modelled with a scaling law of the form $s = s^0 \times (\sigma/\sigma^0)^\alpha$, which allows for significant mass contribution from galaxies also outside their visible haloes. By varying α the galaxies can also have a M/L that depends on the luminosity of the galaxy (α=2 corresponds to a constant M/L).

In light of the significant differences in the two modellings, it is hence rather surprising that all the models, that of Broadhurst et al. (2005a) and those in this thesis, obtain $\langle \chi^2 \rangle^{1/2} \sim 3''$. This means that on average the models predict images $\sim 3''$ (> 60

ACS pixels) from the observed one! In absolute terms this is of course quite appalling and something we should work on to improve. A1689 is the first cluster with such a large number of multiple images from many different background sources. That the two approaches to cluster strong lensing modelling fail similarly in reproducing the multiple images can be potentially useful. The parametric models can only account for mass by explicitly including each mass component that is considered to be significant. The flexible surface mass models on the other hand are free to take any shape allowed within the regularisation[1]. The limitations of the two approaches are in the small scale structure of the mass distribution. In particular, the small scale structure not associated with galaxies, since these are modelled in both models.

Cosmological numerical simulations predict an abundance of small scale structure in clusters. Only the more massive substructure haloes are taken into account in the strong lensing models as galaxies. The number of substructure of a given mass is inversely proportional to the square of the mass, i.e. $N(m) \propto m^{-2}$ (e.g. Moore et al., 1999). This means that cluster have prominent substructure beyond the one in galaxies. In the models the mass in addition to the galaxies is assumed to be completely smooth.

Substructure in galactic haloes can be detected in multiply lensed quasars where the magnification ratios between the separate images are usually poorly modelled by smooth mass models. This gives important information on substructure on galactic scales. On larger scales of clusters the effect of substructure on the derived parameters of smooth profiles has been investigated with weak lensing of cluster haloes by King et al. (2001). They find that a realistic substructure model induces changes of ~3 per cent on the input parameters. Natarajan & Springel (2004) have used galaxy-galaxy lensing to derive the total mass function of bright cluster galaxies including their dark matter haloes in several galaxy clusters. The agreement between their mass functions and those of N-body simulations is good in the mass range $[10^{11}, 10^{12.5}]$ M$_\odot$ that was probed by the observations. This means that the substructure above 10^{11} M$_\odot$ is well traced by the galaxies in the cluster. The amount of substructure (number of bodies of given mass) in N-body simulations continues to grow when substructures less massive than those probed by Natarajan & Springel (2004) are considered.

In this chapter we aim to establish whether or not this small scale granularity beyond the mass resolution of current strong lensing models for A1689 can be used to explain the poor $\langle \chi^2 \rangle^{1/2}$ seen in strong lensing models of A1689, and maybe set some upper limits on the fraction of the total halo mass that is associated with this small scale structure.

---

[1]The regularisation is required so that the surface mass density doesn't have freedom that far exceeds the constraints from the multiple images. The regularisation is also done in order to avoid fitting the noise in the data.

5.2   Methodology

In order to see how big an effect unmodelled substructure can have on the $\langle \chi^2 \rangle^{1/2}$ obtainable with strong cluster lensing models, we use Monte-Carlo simulations similar to those used in chapters 3 and 4. In those simulations we only considered the errors that arise from the scatter in the fundamental plane in the derived velocity dispersions of cluster galaxies. In this chapter we add substructure to the simulated clusters, in addition to the uncertainty on the cluster galaxy velocity dispersions from the scatter in the fundamental plane.

This is done by creating a set of simulated mock galaxy clusters with prominent substructure. For the masses of the subhaloes we have tried several possibilities. First we assume that all subhaloes have the same mass, either 10^{10} M$_\odot$ or 10^{12} M$_\odot$. Alternatively, we have tried a mass spectrum of the form $N \propto m^{-2}$ for the subhaloes. For the mass spectrum we have tried masses in the range $[10^{10}, 10^{12}]$ M$_\odot$ and another with masses in the range $[10^9, 10^{12}]$ M$_\odot$.

To make a realistic model of A1689 we also add the galaxies in their observed positions, but vary their velocity dispersions within the scatter of the fundamental plane. Similarly to the galaxies, the substructure of the smooth dark matter component is assumed to be composed of truncated isothermal spheres. We use the same truncation law for the substructure and the cluster galaxies. The substructure haloes are distributed spatially in such a way that the total projected mass density follows the smooth profile obtained in our earlier strong lensing models for the cluster. In order to study the effect of the amount of substructure, we place a varying fraction of the smooth dark matter in the substructure haloes. The rest of the dark matter is assumed to be in two smooth DM haloes. The parameters of the two smooth haloes are optimised to reproduce the multiple images observed in A1689.

In the case where all of the dark matter is composed of subhaloes of mass 10^{10} M$_\odot$ we have in total more than 1.3×10^5 subhaloes in the cluster model. This is computationally challenging and restricts the number of trials possible in our simulations. For subhaloes of constant mass of 10^{10} M$_\odot$ and for a mass spectrum in the range $[10^9, 10^{12}]$ M$_\odot$ we have created 20 simulated clusters, for the other 2 cases 100 simulated clusters were created.

The final step in creating the simulated clusters is to find the multiple images they would produce. These are based on the observed ones. For each multiple image system we find a source position, that once lensed by the simulated cluster, produces images as close to the observed ones as possible. As we need to able to predict image positions for the models we are not able to use all of the multiple image systems. Due to the high magnification and greatly distorted shapes of images near critical curves it is very difficult to predict multiple images in these regions. Image systems 5, 12, 15, 30, 31 and 32 have not been used for this reason.

Having now established how we have created simulated clusters with substructure

that have mass profiles and multiple image configurations as close as possible to those observed in A1689 we can proceed to the analysis of the simulations and the results.

5.3   Analysis and Results

In the previous section we have explained in some detail how we have created simulated clusters with a varying fraction of the mass in the subhaloes of different masses. In this section we show how well we can reconstruct the multiple image systems of these clusters when we repeat the analysis done in chapter 3 on the simulated clusters.

The analysis in chapter 3 was based on the hopeful assumption that the mass in the cluster is accurately represented by a mass model with the mass in the 200 brightest cluster galaxies and two smooth dark matter profiles. We make the same assumption for the simulated clusters, and try reconstruct them without the substructure that was painstakingly included in the previous section. The galaxies are modelled with their measured velocity dispersions. Since the images were created with galaxies whose velocity dispersions had a scatter around the determined values, we do not expect to be able to reproduce the multiple images perfectly even if very little or no substructure is present in the simulated cluster we are trying to model.

This is basically what happens also in reality when a cluster is modelled with a parametric smooth halo and substructure associated with the galaxies only. All small scale mass structure in the cluster is ignored.

We use the image positions created with the simulated clusters as constraints for the cluster reconstructions. The parameters of the smooth haloes are optimised in the source plane.

The change in the χ^2 for different subhalo populations as the fraction of the mass in the subhaloes is increased is shown in Fig. 5.1. The expected level for the $\langle \chi^2 \rangle^{1/2}$ of 2.2" is shown as a horizontal line. The value is derived from the $\langle \chi^2 \rangle^{1/2}$ levels obtained in creating the simulated clusters. It is important to note that the $\langle \chi^2 \rangle^{1/2}$ is not expected to be around 1". It is a measure of how far images from the models are from the ones used as constraints. Ideally it should be within the error in measuring the image positions. This can be done to within 0.05". As can be seen from Fig. 5.1 the $\langle \chi^2 \rangle^{1/2}$ is already ~1" when only 2% of the mass is in the substructure. This is caused by the error in estimating the mass in the most massive galaxies alone.

As is expected, the more massive the subhaloes, the smaller the fraction of the total mass that can be contained in subhaloes of that mass. This is because the overall mass profile has more pronounced granularity when the subhaloes themselves have higher mass. Smaller subhalo masses result in a smoother total mass profile as the halo is composed of a larger number of small subhaloes and hence a larger fraction of the total mass can be contained in smaller subhaloes.
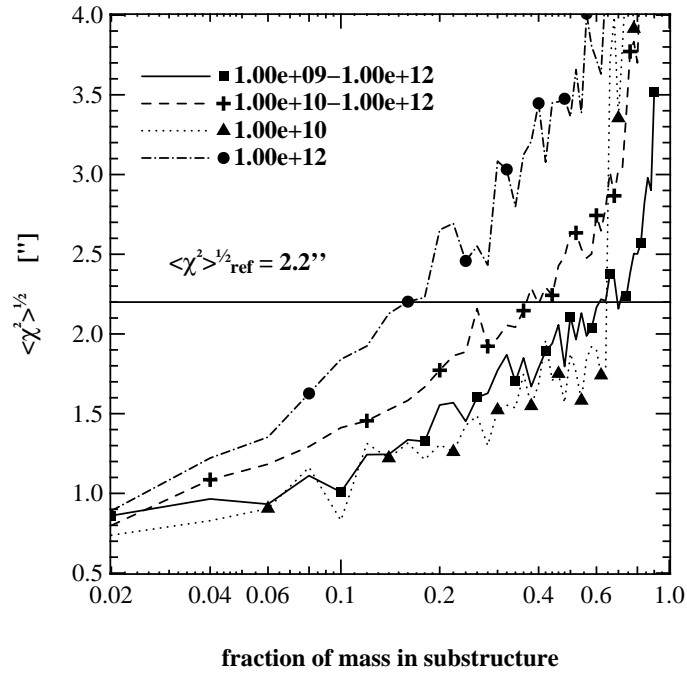
Figure 5.1: In this figure we show the mean $\langle \chi^2 \rangle^{1/2}$ of the clusters that were created with substructure and then later modelled without the substructure. We have created 20-100 clusters with a certain fraction of the DM halo in subhaloes of a given mass (10^{10} or 10^{12} $M_\odot$) or with two mass spectra of the form $N \propto m^{-2}$ in the mass range $[10^{10}, 10^{12}]$ $M_\odot$ and $[10^{10}, 10^{12}]$. For subhaloes of mass 10^{12} $M_\odot$ the observed $\langle \chi^2 \rangle^{1/2}$ is obtained when 16 per cent of the DM is in the the subhaloes. This fraction is higher for smaller mass subhaloes since the halo is composed of a larger number of subhaloes resulting in a smoother profile. The allowed mass fraction goes up to ~70 per cent for subhaloes of mass 10^{10} $M_\odot$

If all the subhaloes have the same mass of $[10, 1000] \times 10^9$ $M_\odot$ we obtain upper limits for the fraction of the total mass in the subhaloes of $[65, 16]$ per cent respectively. For a mass spectrum with masses in range $[10, 1000] \times 10^9$ $M_\odot$ we obtain an upper limit of 40 per cent, and where as for masses in range $[1.0, 1000.0] \times 10^9$ $M_\odot$ an upper limit of 70 per cent is obtained.

5.4 Summary and Conclusion

Natarajan & Springel (2004) have found that the high mass end of the galaxy mass function is accurately described by the cluster galaxies. To achieve a mass resolution better than the one in Natarajan & Springel (2004) (10^{11} M$_\odot$) in galaxy clusters is very difficult since the visible galaxies with masses lower than the limit in Natarajan & Springel (2004) have very small effect on the shapes of background galaxies. Therefore subhaloes of lower mass have to be found indirectly.

In this chapter we have shown that the poor χ^2 seen in the strong lensing analyses of A1689 can be used to obtain upper limits for the mass fraction of the assumed subhalo populations. The different approaches of the mass modelling in this work and in Broadhurst et al. (2005a) lends support for the idea of subhaloes. The χ^2 obtained using a flexible model-free mass distribution in Broadhurst et al. (2005a) is similar to what is seen in this work. If the reason for the high χ^2 in this work would be in the insufficient flexibility of a parametric model we would expect to see a higher χ^2 in our work compared to that of Broadhurst et al. (2005a). The flexible mass distribution of Broadhurst et al. (2005a) should in principle be able to model a perturbed parametric model and hence obtain a better χ^2 if that was indeed the case. The reason for the poor χ^2 is hence more likely in the insufficient mass resolution of both of the two methods. Based on numerical simulations of clusters, these small scale mass perturbations are expected to be in subhaloes that have a mass function closely following $N(M) \propto M^{-2}$.

We find in our simulations that the χ^2 obtained in strong lensing models of A1689 is easily explained by assuming that the smooth DM halo of the cluster is not entirely smooth but is itself composed of subhaloes. For subhalo masses of 10^{10} or 10^{12} M$_\odot$ we find upper limits of 65 and 16 per cent respectively.

We have alternatively assumed a mass spectrum of the form $N(M) \propto M^{-2}$. For masses between 10^{10} and 10^{12} M$_\odot$ we obtain a mass fraction limit of 40 per cent. For a lower mass limit of 10^9 M$_\odot$ (10^9 M$_\odot$ $<M<10^{12}$ M$_\odot$) 70 per cent of the smooth DM is allowed be in the subhaloes.

It should be noted that in reality galaxy cluster have also larger scale deviations from the completely smooth dark matter halo profile assumed in this work. Part of the χ^2 seen in chapter 3 will also be explained by these deviations from an idealised situation. The χ^2 might also suffer from other systematic effects in the modelling that increase its values. The acceptable levels of substructure mass should therefore serve as useful upper limits only.

Chapter 6

Summary of the Thesis

In the course of this thesis we have described the code developed to construct strong gravitational lensing models for astronomical applications and applied it to galaxy cluster A1689. The deep HST images of the cluster reveal an impressive number of multiple images in many image systems spread over the HST Advanced Camera for Surveys (ACS) field of the central region of the cluster.

A major part of the work is contained in Chapter 3 where we gave a detailed account of the identification of the multiple images. The work started with archived images in two bands obtained with WFPC2 camera on the HST. Later also images from ACS came available providing a additional filters and an improved resolution over a larger field-of-view. With the now 6 available filters we are able to select cluster galaxies using a colour-magnitude diagram and derive photometric redshifts for the identified multiple images. In total 107 multiple images have been identified in 31 different image systems. We also include one giant arc in the analysis. Five image systems have a spectroscopic redshift from literature. These are in good agreement with the photometric ones.

We have performed fundamental plane (FP) analysis of most of the central cluster galaxies in order to measure their central velocity dispersions. For a number of fainter galaxies we have estimated the velocity dispersions of the galaxies using the Faber-Jackson relation which connects a galaxy's luminosity and its velocity dispersion.

Our strong lensing model of the cluster is composed of the galaxies and a smooth halo of the cluster. The smooth halo of the cluster is modelled with two parametric halo profiles. We have chosen to use an NFW profile that is a result of numerical simulations with cold dark matter and a softened isothermal sphere often used in cluster lensing. The accurate determinations of the galaxy velocity dispersions and the tight constraints imposed by the multiple images in the cluster require us to include also truncation of the haloes in the modelling of the cluster galaxies. The cluster galaxies are modelled

with truncated isothermal spheres (BBS, Brainerd et al., 1996). The truncation radii, s, are assumed to correlate with the velocity dispersions σ of the galaxies according to $s = s^0 (\sigma / \sigma^0)^\alpha$. The power α is chosen to match those in the field ($\alpha=2$, e.g. Brainerd et al., 1996; Hoekstra et al., 2004) and a theoretical model for galaxy truncation in cluster ($\alpha=1$, Merritt, 1983). The normalisation s^0 is obtained from the data for a fiducial $\sigma^0=220$ km/s.

We find that both NSIE and ENFW profiles are able to describe the smooth DM halo of the cluster equally well. Also the total mass profile for the cluster is equally well fit by both NSIE and ENFW profiles. The total mass profile is in good agreement with the one derived in Broadhurst et al. (2005a) using a more flexible description for the smooth mass distribution. The total mass is higher than previous mass estimates using both weak lensing and X-ray measurements. The discrepancy is starting to be understood and can in part be explained by systematic effect in the weak lensing analyses, and the unrelaxed state of the cluster in the X-ray. For accurate weak lensing masses it is important to know the redshifts of the background sources and minimise the contamination from galaxies both in the foreground and in the cluster. This has been discussed in Clowe (2003); Broadhurst et al. (2005a). Andersson & Madejski (2004) discuss the discrepancy of the X-ray analysis and conclude that the mass could be underestimated by a factor of 2 if the cluster is composed of several substructures on the same line of sight. New weak lensing work Broadhurst et al. (2005b) and a better understanding of the cluster dynamics in the part of the X-ray measurements have therefore essentially solved the mass discrepancy.

Little attention was paid to the extensions of the haloes of the cluster galaxies in Chapter 3. This is rectified in Chapter 4 where we analyse in detail the extensions of galaxy haloes. Optical traces in the galaxy haloes indicate that the haloes of field galaxies stay roughly isothermal beyond several hundred kiloparsecs. Gravitational lensing enables us to probe the haloes out to larger radii. Galaxy-galaxy lensing in the field has shown that the haloes extend as far out as 1 Mpc but are strongly truncated in dense cluster environments.

In Chapter 4 we introduce strong galaxy-galaxy lensing, the lensing of multiple images of background galaxies by foreground galaxies. This extends the standard galaxy-galaxy lensing for the first time also to multiply imaged sources. This is made possible in A1689 by the unprecedented number of multiple images. We confirm the truncation of galaxy haloes in clusters when compared to field galaxies as discussed by Natarajan et al. (e.g. 2002); Limousin et al. (e.g. 2006). The obtained truncation radii are also consistent within the considerable errors. Combining results from several cluster, a good agreement to theoretical expectations (Merritt, 1983) is found in the relation between the truncation radii of galaxies and the density of the cluster. This supports the idea that the haloes are truncated mainly by the

dense intra cluster medium and harassment by other cluster galaxies plays a minor role.

Published strong lensing analyses have generally a poor absolute fit quality (in the cases where it is published). This is a point that is seldom discussed in the literature, presumably in an attempt not to damage the credibility in the results derived using strong lensing. The poor fit quality can be potentially useful, and tell us about the physics not included in the analysis. The very similar χ^2 obtained in the parametric approach in this work and in the more flexibly model of Broadhurst et al. (2005a) may indicate that the problem is at smaller scales than probed by either model. We propose in Chapter 5 that the smooth DM of the cluster as a whole is not so smooth after all but is composed of subhaloes of smaller mass that affect the multiple image positions and the χ^2.

We investigate this point by running simulations where we model clusters with known substructure (we create the cluster configuration and multiple images) without the substructure. We can create clusters with a varying fraction of the mass in the substructure and see at what stage the χ^2 of a substructure free model reaches the one observed in A1689. A limitation of our approach is that the substructure is assumed to follow either an NSIE or an NFW profile and hence any possible deviation from these profiles that occurs in nature is not included. This makes the results obtained here only upper limits for the mass in substructure. The χ^2 can be significantly affected by a smooth deviation from the assumed profiles.

If all the subhaloes have the same mass of $[10, 1000] \times 10^9$ M$_\odot$ we obtain upper limits for the fraction of the total mass in the subhaloes of $[65, 16]$ per cent respectively. For a mass spectrum with masses in range $[10, 1000] \times 10^9$ M$_\odot$ with a mass function N(M) $\propto$ M^{-2} we obtain an upper limit of 40 per cent, and for masses in range $[1, 1000] \times 10^9$ M$_\odot$ an upper limit of 70 per cent.

We are restricted to a lower mass limit of $\times 10^9$ M$_\odot$ in our analysis by the time taken by the calculations. The χ^2 observed in A1689 can be explained by any of the assumed subhalo masses (or mass spectra) given high enough fraction of the total mass is in the subhaloes. The next step would be either to improve the code speed in order to push the lower limit further. Another option could be to quantify the effect of the inevitable perturbations of real clusters from the idealised NFW or NSIE halo used here and see if the perturbations are enough to explain the poor χ^2.

Even if we haven't been able to draw strict boundaries for the subhalo population in haloes of galaxy clusters we have shown that the high absolute χ^2 often seen in strong lensing models can be easily explained by deviation from a perfectly smooth halo profile. It should be noted that although the χ^2 can be easily explained with subhaloes to actually include the subhaloes in the modelling is very challenging. A good way to begin would be to study the effect of the subhaloes on the derived total mass distribution and on the obtained parameters of, for example, NSIE and NFW

profiles.

In this thesis we have applied strong lensing to many different aspects of the properties of galaxy clusters A1689: we have measured the mass profile and mass distribution of the cluster as a whole, the extensions of the haloes of the cluster galaxies, and we have shown that the poor χ^2 in strong lensing mass reconstructions can be easily explained with subhaloes.

Bibliography

Abdelsalam H. M., Saha P., Williams L. L. R., 1998, MNRAS, 294, 734 25, 44

Allen S. W., 1998, MNRAS, 296, 392 26

Andersson K. E., Madejski G. M., 2004, ApJ, 607, 190 25, 26, 42, 43, 56, 73, 75, 76, 82, 83, 84, 88, 142

Balogh M. L., Couch W. J., Smail I., Bower R. G., Glazebrook K., 2002, MNRAS, 335, 10 48, 50, 84, 123

Bardeau S., Kneib J.-P., Czoske O., Soucail G., Smail I., Ebeling H., Smith G. P., 2005, A&A, 434, 433 43, 85, 88

Bartelmann M., 1996, A&A, 313, 697 31, 90

Battaglia G. et al., 2005, MNRAS, 364, 433 120

Bender R. et al., 2001, in Deep Fields, p. 96 48

Bender R., Burstein D., Faber S. M., 1992, ApJ, 399, 462 52, 122

Bender R., Saglia R. P., Gerhard O. E., 1994, MNRAS, 269, 785 119

Bennett C. L. et al., 1996, ApJ, 464, L1 4

Bernstein G., Fischer P., Tyson J. A., Rhee G., 1997, ApJ, 483, L79 19

Bernstein G. M., Jarvis M., 2002, AJ, 123, 583 22

Bertin E., Arnouts S., 1996, A&AS, 117, 393 47

Biviano A., Salucci P., 2005, Astro-ph, 0511309 81

Blandford R. D., Kochanek C. S., 1987, ApJ, 321, 658 30, 45, 55, 89

Bouwens R. J. et al., 2004, ApJ, 616, L79 12

Brainerd T. G., 2004, in Allen R. E., Nanopoulos D. V., Pope C. N., ed, AIP Conf. Proc. 743: The New Cosmology: Conference on Strings and Cosmology, p. 129 120

Brainerd T. G., Blandford R. D., Smail I., 1996, ApJ, 466, 623 29, 32, 50, 91, 120, 122, 127, 131, 142

Broadhurst T. et al., 2005a, ApJ, 621, 53 xi, 26, 41, 42, 43, 44, 45, 58, 59, 61, 65, 69, 71, 72, 73, 75, 76, 78, 85, 86, 87, 88, 96, 97, 98, 99, 100, 121, 135, 140, 142, 143

Broadhurst T., Huang X., Frye B., Ellis R., 2000, ApJ, 534, L15 21, 22

Broadhurst T., Takada M., Umetsu K., Kong X., Arimoto N., Chiba M., Futamase T., 2005b, ApJ, 619, L143 26, 41, 42, 43, 65, 77, 78, 79, 80, 82, 85, 86, 87, 142

Broadhurst T. J., Taylor A. N., Peacock J. A., 1995, ApJ, 438, 49 22

Bruzual G., Charlot S., 2003, MNRAS, 344, 1000 53

Burles S., Nollett K. M., Turner M. S., 1999, ArXiv Astrophysics e-prints 8, 9

Cannon D. B., Ponman T. J., Hobbs I. S., 1999, MNRAS, 302, 9 25

Clowe D., 2003, in Bowyer S., Hwang C.-Y., ed, Astronomical Society of the Pacific Conference Series, p. 271 26, 43, 85, 88, 142

Clowe D., Bradač M., Gonzalez A. H., Markevitch M., Randall S. W., Jones C., Zaritsky D., 2006, ApJ, 648, L109 22, 23

Clowe D., Schneider P., 2001, A&A, 379, 384 25, 26, 43, 85, 88

Coleman G. D., Wu C.-C., Weedman D. W., 1980, ApJS, 43, 393 53

Crill B. P. et al., 2003, ApJS, 148, 527 4

Czoske O., 2004, in IAU Colloq. 195: Outskirts of Galaxy Clusters: Intense Life in the Suburbs, p. 183 84

dell'Antonio I. P., Tyson J. A., 1996, ApJ, 473, L17 120

Dicke R. H., Peebles P. J. E., Roll P. G., Wilkinson D. T., 1965, ApJ, 142, 414 4

Diego J. M., Protopapas P., Sandvik H. B., Tegmark M., 2005a, MNRAS, 360, 477 45

Diego J. M., Sandvik H. B., Protopapas P., Tegmark M., Benítez N., Broadhurst T., 2005b, MNRAS, 362, 1247 26, 45, 121

Diemand J., Moore B., Stadel J., 2004, MNRAS, 353, 624 31

Djorgovski S., Davis M., 1987, ApJ, 313, 59 52, 122

Dressler A., Lynden-Bell D., Burstein D., Davies R. L., Faber S. M., Terlevich R., Wegner G., 1987, ApJ, 313, 42 52, 122

Duc P.-A. et al., 2002, A&A, 382, 60 48, 50, 84, 123

Dye S., Taylor A. N., Thommes E. M., Meisenheimer K., Wolf C., Peacock J. A., 2001, MNRAS, 321, 685 26, 42, 83

Faber S. M., Jackson R. E., 1976, ApJ, 204, 668 53, 122

Fischer P. et al., 2000, AJ, 120, 1198 120, 131

Ford H., 2002, in HST Proposal, p. 5668 47

Fort B., Mellier Y., Dantel-Fort M., 1997, A&A, 321, 353 59, 96, 98

Freedman W. L. et al., 2001, ApJ, 553, 47 5, 7

Fritz A., Ziegler B. L., Bower R. G., Smail I., Davies R. L., 2005, MNRAS, 358, 233 53, 54, 55

Frye B., Broadhurst T., Benítez N., 2002, ApJ, 568, 558 48, 59, 96, 97, 98

Fukushige T., Makino J., 1997, ApJ, 477, L9 14

Fukushige T., Makino J., 2001, ApJ, 557, 533 31

Gössl C. A., Riffeser A., 2002, A&A, 381, 1095 46

Gavazzi R., Fort B., Mellier Y., Pelló R., Dantel-Fort M., 2003, A&A, 403, 11 25

Gavazzi R., Mellier Y., Fort B., Cuillandre J.-C., Dantel-Fort M., 2004, A&A, 422, 407 52, 120, 129, 130, 131

Geiger B., Schneider P., 1998, MNRAS, 295, 497 120

Geiger B., Schneider P., 1999, MNRAS, 302, 118 120

Ghigna S., Moore B., Governato F., Lake G., Quinn T., Stadel J., 1998, MNRAS, 300, 146 133

Ghigna S., Moore B., Governato F., Lake G., Quinn T., Stadel J., 2000, ApJ, 544, 616 130, 133

Girardi M., Fadda D., Escalera E., Giuricin G., Mardirossian F., Mezzetti M., 1997, ApJ, 490, 56 25, 26, 43, 48, 50, 56, 83, 84, 87, 88

Goldberg D. M., Leonard A., 2006, ArXiv Astrophysics e-prints 24

Goldberg D. M., Natarajan P., 2002, ApJ, 564, 65 24

Golse G., 2002, Ph.D. thesis, Laboratoire d'Astrophysique de l'Observatoire Midi-Pyrénées 48, 59, 96, 97, 98

Golse G., Kneib J.-P., 2002, A&A, 390, 821 31, 90, 91

Gott J. R. I., Gunn J. E., 1974, ApJ, 190, L105 30, 89

Halkola A., Seitz S., M. P., 2006, Astro-ph, 0605470, accepted for publication in the MNRAS, 1 121, 122, 123, 130

Hanany S. et al., 2000, ApJ, 545, L5 4

Hartwick F. D. A., Sargent W. L. W., 1978, ApJ, 221, 512 120

Heidt J. et al., 2003, A&A, 398, 49 47

Hinshaw G., Krauss L. M., 1987, ApJ, 320, 468 30, 89

Hoekstra H., 2001, A&A, 370, 743 85

Hoekstra H., 2003, MNRAS, 339, 1155 85, 120, 131

Hoekstra H., Yee H. K. C., Gladders M. D., 2004, ApJ, 606, 67 41, 50, 51, 120, 122, 131, 142

Holtzman J. A., Burrows C. J., Casertano S., Hester J. J., Trauger J. T., Watson A. M., Worthey G., 1995, PASP, 107, 1065 46

Hubble E., 1929, Proceedings of the National Academy of Science, 15, 168 5

Hubble E. P., 1936, Yale University Press 12

Hudson M. J., Gwyn S. D. J., Dahle H., Kaiser N., 1998, ApJ, 503, 531 120

Jørgensen I., Franx M., Kjaergaard P., 1996, MNRAS, 280, 167 53

Kaiser N., Squires G., 1993, ApJ, 404, 441 22

Kaiser N., Squires G., Broadhurst T., 1995, ApJ, 449, 460 22

Kassiola A., Kovner I., 1993, ApJ, 417, 450 89

Kassiola A., Kovner I., Fort B., 1992, ApJ, 400, 41 21

Kayser R., Schramm T., 1988, A&A, 191, 39 58

King L. J., Clowe D. I., Lidman C., Schneider P., Erben T., Kneib J.-P., Meylan G., 2002, A&A, 385, L5 26, 42, 43, 56, 73, 76

King L. J., Clowe D. I., Schneider P., 2002, A&A, 383, 118 25, 26, 85, 88

King L. J., Schneider P., Springel V., 2001, A&A, 378, 748 136

Kneib J.-P., Ellis R. S., Smail I., Couch W. J., Sharples R. M., 1996, ApJ, 471, 643 31

Kneib J.-P. et al., 2003, ApJ, 598, 804 25, 44

Kneib J. P., Mellier Y., Fort B., Mathez G., 1993, A&A, 273, 367 44

Kneib J. P., Mellier Y., Pello R., Miralda-Escude J., Le Borgne J.-F., Boehringer H., Picat J.-P., 1995, A&A, 303, 27 25

Kochanek C. S., Blandford R. D., Lawrence C. R., Narayan R., 1989, MNRAS, 238, 43 30, 89

Kormann R., Schneider P., Bartelmann M., 1994, A&A, 284, 285 30, 55, 89

Kormendy J., Bender R., 1996, ApJ, 464, L119 12

Labbé I., Bouwens R., Illingworth G. D., Franx M., 2006, ApJ, 649, L67 12

Limousin M., Kneib J.-P., Bardeau S., Natarajan P., 2006, A&A 120, 129, 130, 131, 132, 133, 142

Limousin M., Kneib J.-P., Natarajan P., 2005, MNRAS, 356, 309 120

Lokas E. L., Prada F., Wojtak R., Moles M., Gott ober S., 2005, Astro-ph, 0507508 84

Lu Y., Mo H. J., Katz N., Weinberg M. D., 2006, MNRAS, 368, 1931 31

Lynds R., Petrosian V., 1986, BAAS, 18, 1014 25

Markevitch M., Gonzalez A. H., David L., Vikhlinin A., Murray S., Forman W., Jones C., Tucker W., 2002, ApJ, 567, L27 23

McKay T. A. et al., 2001, Astro-ph 120

Melchior P., Meneghetti M., Bartelmann M., 2006, ArXiv Astrophysics e-prints 24

Mellier Y., Meylan G., ed, 2005, Impact of Gravitational Lensing on Cosmology (S225) 21

Meneghetti M., Bartelmann M., Moscardini L., 2003, MNRAS, 340, 105 31, 32, 33, 90

Merritt D., 1983, ApJ, 264, 24 41, 50, 122, 127, 130, 142

Meylan G., Jetzer P., North P., Schneider P., Kochanek C. S., Wambsganss J., ed, 2006, Gravitational Lensing: Strong, Weak and Micro 29

Miralda-Escude J., 1995, ApJ, 438, 514 56

Miralda-Escude J., Babul A., 1995, ApJ, 449, 18 26

Moore B., Ghigna S., Governato F., Lake G., Quinn T., Stadel J., Tozzi P., 1999, ApJ, 524, L19 136

Moore B., Governato F., Quinn T., Stadel J., Lake G., 1998, ApJ, 499, L5 14, 21

Moore B., Katz N., Lake G., Dressler A., Oemler A., Jr., 1996, Nat, 379, 613 133

Moore B., Lake G., Katz N., 1998, ApJ, 495, 139 130, 133

Natarajan P., Kneib J.-P., 1997, MNRAS, 287, 833 120

Natarajan P., Kneib J.-P., Smail I., 2002, ApJ, 580, L11 51, 120, 129, 130, 132, 133, 142

Natarajan P., Kneib J.-P., Smail I., Ellis R. S., 1998, ApJ, 499, 600 51, 120, 122, 129, 130, 133

Natarajan P., Springel V., 2004, ApJ, 617, L13 136, 140

Navarro J. F., Frenk C. S., White S. D. M., 1996, ApJ, 462, 563 13, 14, 21, 29, 31, 45, 90

Navarro J. F. et al., 2004, MNRAS, 349, 1039 31

Oguri M., Takada M., Umetsu K., Broadhurst T., 2005, Astro-ph, 0505452 44, 87

Okura Y., Umetsu K., Futamase T., 2006, ArXiv Astrophysics e-prints 24

Ota N., Mitsuda K., Fukazawa Y., 1998, ApJ, 495, 170 25

Peng C. Y., Ho L. C., Impey C. D., Rix H., 2002, AJ, 124, 266 53

Penzias A. A., Wilson R. W., 1965, ApJ, 142, 419 3, 4

Prada F. et al., 2003, ApJ, 598, 260 120

Press W. H., Teukolsky S. A., Vetterling W. T., Flannery B. P., 1992, Numerical recipes in C. The art of scientific computing. Cambridge: University Press, —c1992, 2nd ed. 34

Refsdal S., 1964, MNRAS, 128, 307 20

Rhodes J., Refregier A., Groth E. J., 2000, ApJ, 536, 79 22

Richard J., Pelló R., Schaerer D., Le Borgne J.-F., Kneib J.-P., 2006, A&A, 456, 861 12

Riess A. G. et al., 1998, AJ, 116, 1009 5

Roberts M. S., Rots A. H., 1973, A&A, 26, 483 30, 89

Salvador-Solé E., Manrique A., Solanes J. M., 2005, MNRAS, 358, 901 31

Schlegel D. J., Finkbeiner D. P., Davis M., 1998, ApJ, 500, 525 53

Schneider P., Ehlers J., Falco E. E., 1992, Gravitational Lenses. Springer-Verlag, Berlin 29

Schramm T., Kayser R., 1987, A&A, 174, 361 58

Seitz S., Saglia R. P., Bender R., Hopp U., Belloni P., Ziegler B., 1998, MNRAS, 298, 945 30, 58, 89

Sersic J. L., 1968, Atlas de galaxias australes. Cordoba, Argentina: Observatorio Astronomico, 1968 53

Shapiro P. R., Iliev I. T., 2000, ApJ, 542, L1 22

Simard L. et al., 1999, ApJ, 519, 563 53

Smith D. R., Bernstein G. M., Fischer P., Jarvis M., 2001, ApJ, 551, 643 120, 131

Smith G. P., Kneib J.-P., Smail I., Mazzotta P., Ebeling H., Czoske O., 2005, MNRAS, 359, 417 43

Sofue Y., Rubin V., 2001, ARA&A, 39, 137 119

Soucail G., Fort B., Mellier Y., Picat J. P., 1987, A&A, 172, L14 25

Spergel D. N. et al., 2006, ArXiv Astrophysics e-prints 10

Spergel D. N. et al., 2003, ApJS, 148, 175 4, 5, 6, 7, 21

Tasitsiomi A., Kravtsov A. V., Gottlöber S., Klypin A. A., 2004, ApJ, 607, 125 31

Taylor A. N., Dye S., Broadhurst T. J., Benitez N., van Kampen E., 1998, ApJ, 501, 539 26

Teague P. F., Carter D., Gray P. M., 1990, ApJS, 72, 715 26, 42, 43, 50, 83, 84, 123

Teplitz H. I., Malkan M. A., McLean I. S., 2004, ApJ, 608, 36 58

Thuan T. X., Gunn J. E., 1976, PASP, 88, 543 53

Tormen G., Diaferio A., Syer D., 1998, MNRAS, 299, 728 119

Turner E. L., Ostriker J. P., Gott J. R., 1984, ApJ, 284, 1 30, 89

Tyson J., 1995, in HST Proposal, p. 2477 46

Tyson J. A., Fischer P., 1995, ApJ, 446, L55 26, 83

Tyson J. A., Kochanski G. P., dell'Antonio I. P., 1998, ApJ, 498, L107 21, 22

Tyson J. A., Valdes F., Jarvis J. F., Mills A. P., 1984, ApJ, 281, L59 120

Walsh D., Carswell R. F., Weymann R. J., 1979, Nat, 279, 381 18, 19

Wilson G., Kaiser N., Luppino G. A., Cowie L. L., 2001, ApJ, 555, 572 120

Wright C. O., Brainerd T. G., 2000, ApJ, 534, 34 31, 90

Xue S., Wu X., 2002, ApJ, 575, 152 25, 26, 42, 56, 82, 83

Zaritsky D., Olszewski E. W., Schommer R. A., Peterson R. C., Aaronson M., 1989, ApJ, 345, 759 120

Zekser K. C. et al., 2006, ApJ, 640, 639 26, 45, 88, 121

Ziegler B. L., Bower R. G., Smail I., Davies R. L., Lee D., 2001, MNRAS, 325, 1571 53, 54, 55

Appendix A

Dark matter

Some of the evidence for dark matter has been discussed in the Introduction in chapter 1 but the limits on the properties and some of the candidates for dark matter itself were not discussed. Although certainly a part of the dark matter is normal baryonic matter that doesn't emit enough radiation to be detected, it is by now well accepted that most of the dark matter has to be in some kind of new elementary particle that does not interact with electromagnetic radiation. This is because although baryonic dark matter can help in solving the problem of unseen matter in galaxies and clusters, it cannot solve the problems of structure formation and of the element abundances in the Big Bang nucleosynthesis which together require non-baryonic dark matter. In this Appendix we give some current ideas for what the matter that makes up most of the universe could be. In the following only non-baryonic dark matter will be discussed. We will also not discuss alternative theories to the Standard Model here.

A.1 Hot dark matter

Hot dark matter consist of particles with relativistic speeds. Examples include light neutrinos and gravitinos. The total mass contained in these neutrinos cannot be very high, or otherwise they would prohibit the formation of small scale structure to a level that would contradict the wealth of structure seen in the universe today.

A.2 Cold dark matter

Opposite to its hot counterpart, cold dark matter is composed of slowly moving particles. The slow speeds of particles mean that small scale structures can form more easily.

There is good agreement between the structures seen in numerical simulations with

cold dark matter and the observed observed universe. Also the mass profiles of cluster and galaxies from the simulations agree well with observations. These provide strong support for the cold dark matter paradigm. Although the paradigm successfully reproduces observed phenomena, it cannot tell us what most of the matter content of the universe is made of. This is a question for particle physicists. Some of the particles included in the answers are:

Neutralino

In supersymmetric theories, bosons (fermions) have fermionic (bosonic) supersymmetric partners, e.g. a photon's supersymmetric partner is a photino. These can mix to form neutralinos. A possible mass range for neutralinos is from 30 GeV to 3 TeV, and as such they are an excellent cold dark matter candidate. Neutralinos are expected to annihilate, and the energy released in the annihilation is equal to the mass of the neutralino. There are several projects looking at the centre of the Galaxy for well defined gamma-ray lines that could result from these annihilation processes.

Axion

Axions are hypothetical particles that are used to explain the strong-CP (charge/parity) problem in QCD (quantum chromodynamics). Certain types of weak decays seemed to violate the strong-CP symmetry. Axions are thought to be created at this symmetry braking and thus solve the symmetry violation. The current imbalance in matter/anti-matter is a result of the strong-CP violation and an indication that the Big Bang should have produced large amounts of axions. Provided that the axions have a suitable mass, they are a promising candidate for a cold dark matter particle.

Q-balls

Q-balls are another cold dark matter candidate arising from supersymmetric theories. They are localised field configurations, where the stability is provided by the conservation of charge. Q-balls might be created in the early universe and be preserved until today.

A.3   Warm dark matter

A compromise solution between the two extremes can be a mix between the two, and is therefore warm. This is most certainly the case since we know that hot dark matter exists at least in neutrinos and we have strong evidence to believe that cold dark matter exists also. But it is possible that warm dark matter is truly warm.

Neutrinos could help in this region again. Their energy would optimally have to be around 1 kev. This would solve the over merging problem; numerical simulations

predicted many more substructures in galaxies than what is observed. If the mass of the neutrino is around 1 kev it suppresses the formation of satellites sufficiently. Larger masses have little effect on the number of satellites and less massive neutrinos on the other hand would be too hot and result in too few satellites in simulations.

Acknowledgements

I would like to thank my thesis supervisor Ralf Bender and thesis advisor Stella Seitz for giving me the opportunity to work on the exceptional strong lensing cluster A1689. Stella was there when needed, guiding me with her suggestions and questions on the perilous path to a PhD. I would especially like to thank her for not giving me a ready made map for the road but allowing me to find my own way, even if it sometimes took an odd turn here and there.

This thesis would not be what it is without Maurilio Pannella. With his expertise, the galaxies in 'my' cluster fell on a plane. I value greatly the input he has given to this thesis, his patience with a very inexperienced collaborator and for his views on what science really is all about.

Jan Snigula and Claus Gössl both deserve a huge thank you for their patience in answering my endless questions about the workings of linux, ltl, and computers in general. In the beginning of my thesis the data reduction experience and help of Armin Gabasch, Arno Riffeser and Jürgen Fliri was invaluable in getting me started. In addition I am grateful to Jan and Georg Feulner for not locking their office door in the beginning of my thesis. My "I have a Yorick question!" could easily have had just that effect!

I was very lucky with the office assigned to me and from the beginning Armin Gabasch and Jürgen Fliri were the best imaginable office mates and tutors. The atmosphere was only improved when Veronika Junk joined the office. Discussions on any aspect of astronomy were always interesting. I would like to thank Armin for always finding time to answer my questions whenever I've needed help with bash/LaTeX/sm/perl/awk/..., Jürgen for the many times I've been to Garching with him and Veronika for never doing what she always threatened to do.

I thank my friends for their friendship, help and support which I value greatly. I thank also my backing team at home who have always supported me on the way, both in the choices I have made and at difficult times. Cécile has been wonderful in being there when needed but equally importantly giving me the space I need for myself at times. I also thank her family for providing me with a Bed and Breakfast (and much more) on my numerous visits to Munich from Bonn.

CURRICULUM VITAE

Name:	Aleksi Halkola
Citizenship:	Finnish
Date of birth:	12 January 1979
Place of birth:	Iisalmi, Finland
Marital Status:	Single

Home Address:	Aloys-Schulte-Str. 50 53129 Bonn Germany

Current Work Address:	Argelander-Institut für Astronomie Auf dem Hügel. 71 53121 Bonn Germany

Telephone:	Work:	+49 (0)228 736787
	Home:	+49 (0)228 2433428
	Mobile:	+49 (0)179 9627408

Languages	Good:	Finnish, English
	Some:	German, French, Swedish

Education	2002 –	Ph.D. Student in Astronomy LMU, Munich, Germany
	1998 – 2002	M.Sci. Mathematics and Astronomy University College London, London, England
	1996 – 1998	International Baccalaureate United World College of the Atlantic, Wales
	1995 – 1996	First year of high school Luostarivuoren Lukio, Turku, Finland
	1986 – 1995	Primary Education Luostarivuoren Yläaste, Turku, Finland Wäinö Aaltosen Koulu, Turku, Finland